



FRIEDRICH-SCHILLER-UNIVERSITÄT  
JENA  
PHYSIKALISCH-ASTRONOMISCHE FAKULTÄT  
ASTROPHYSIKALISCHES INSTITUT UND  
UNIVERSITÄTS-STERNWARTE



# Architecture of selected full planetary systems

—DISSERTATION—

ZUR ERLANGUNG DES AKADEMISCHEN GRADES  
DOCTOR RERUM NATURALIUM (DR. RER. NAT.)

vorgelegt dem Rat der Physikalisch-Astronomischen Fakultät  
der Friedrich-Schiller-Universität Jena

von Dipl.-Phys. MARTIN REIDEMEISTER  
geboren am 25. März 1982 in Magdeburg

Gutachter:

1. ....

2. ....

3. ....

Tag der Disputation: .....

# Danksagung

Ich möchte mich zu aller erst bei meinem Doktorvater Prof. Dr. Alexander Krivov für seine umfassende Unterstützung und herzliche Betreuung in den vergangenen Jahren bedanken. Seine fachliche und didaktische Kompetenz, aber auch sein Vertrauen und seine Geduld, vor allem am Schluss, haben maßgeblich zur Vollendung dieser Arbeit beigetragen.

Kaum weniger wichtig waren meine Bürokollegen Torsten Löhne und Christian Vintense, die mir jederzeit mit Rat und Tat zur Seite standen, mich mit viel Witz bei Laune hielten und eine wichtige Grundlage für das familiäre Gefüge in unserem Haus bildeten.

Auch Jürgen Weiprecht möchte ich hier erwähnen und danken, für seine gewissenhafte und unermüdliche Pflege von Nimloth und allen anderen Rechenknechten hier am Institut, ohne die meine Arbeit erst gar nicht möglich gewesen wäre.

Weiterhin danke ich allen meinen Kollegen hier am AIU, die mir mit ihrer Gesellschaft und Gesprächen, von fachlich intellektuell, bis hin zum Donnerstagsabendniveau, eine wunderschöne Zeit bescherten und das AIU über viele Jahre hinweg für mich zu einem zweiten Zuhause machten.

Ich möchte auch Grit Ronneburg für ihr geduldiges und immer offenes Ohr danken. Ebenso sei Jeremy Pierce Mayer für seine Zeit gedankt, die er sich für muttersprachliche Korrekturen genommen hat.

Und nicht zuletzt danke ich meinen Eltern, die in jeglicher Hinsicht die Grundsteine für meinen Weg gelegt haben.

Ohne all diese großen und kleinen, direkten und indirekten Beiträge zu meinem Leben wäre ich heute nicht hier und derjenige, der ich bin.

Vielen Dank!





# Kurzfassung

Unser Wissen über den Aufbau von Planetensystemen ist noch immer im Wandel. Unser Sonnensystem mit seinen acht Planeten, dem inneren Asteroidengürtel, sowie dem Kuipergürtel am äußeren Rand gilt als Prototyp eines Planetensystems. Durch die Entdeckungen von zum Beispiel heißen Jupitern oder sehr massereichen und ausgedehnten Trümmerscheiben wurde dies in Frage gestellt. Natürlich wurden durch die Einschränkungen in der Beobachtungstechnik bisher nur die Extremfälle entdeckt. In den meisten Systemen kennen wir nur Planeten oder nur Trümmerscheiben. In einigen Fällen sind jedoch sowohl Planeten als auch Trümmerscheiben bekannt. Für diese Systeme führen wir den Begriff „vollständige Planetensysteme“ ein.

In dieser Arbeit wurde die Architektur von vollständigen Planetensystemen anhand der zwei Beispielsysteme HR 8799 und  $\epsilon$  Eridani untersucht. HR 8799 ist ein Mehrfachplanetensystem, in dem eine innere und eine äußere Staubscheibe bekannt sind, deren jeweils äußerer bzw. innerer Rand von vier massereichen Gasriesen geformt wird. Das System wurde zum einen auf die Stabilität und die Orientierung mit Hilfe von N-Körper-Simulationen untersucht. Zum anderen wurde versucht die Lage, Ausdehnung und Masse der Scheiben anhand der spektralen Energieverteilung zu bestimmen. Zusätzlich wurde auch das Alter des Sterns, seine Inklination sowie die Masse der Planeten berücksichtigt.

Bei  $\epsilon$  Eridani widmeten wir uns der Frage, welchen Ursprung der warme Staub nahe des Sterns hat. Ein Planetesimalgürtel in unmittelbarer Nähe, als Quelle des Staubs, ist unplausibel, da dieser von dem inneren Planeten in kürzester Zeit zerstreut worden wäre. In der Studie konnte gezeigt werden, dass genug warmer Staub von der massiven äußeren Trümmerscheibe durch Transportprozesse (P-R-Effekt, stellarer Wind) nach innen strömen kann, um die Beobachtungen zu erklären.

Ein dritter Teil bestand in der Suche nach Trümmerscheibenkandidaten in Transitplanetensystemen. Dies ist vor allem deshalb von besonderem Interesse, da zum einen bisher noch keine Trümmerscheiben in Transitsystemen bekannt sind, und zum anderen in Transitsystemen die direkte Bestimmung von Planeteneigenschaften wie Masse, Radius und Dichte möglich ist. Außerdem ermöglicht ein Transit Einblicke in die Planetenatmosphäre und somit auch in deren inneren Aufbau. Die Entdeckung von Trümmerscheiben in Transitplanetensystemen würde helfen, die Entstehung von bekannten Planeten zu klären. Im *vorläufigen* Katalog des *WISE All-Sky Surveys* fanden wir zwei Kandidaten vollständiger Planetensysteme. Diese konnten jedoch in der *finalen* Version des WISE-Katalogs nicht bestätigt werden.

Mit diesen Beispielen für vollständige Planetensysteme zeigen wir einerseits, welche unterschiedlichen Architekturen bisher bekannt sind und andererseits welche Rückschlüsse sich aus der gemeinsamen Analyse von Trümmerscheibe und Planeten, aber auch des Zentralsterns ziehen lassen. Dabei steht nicht nur der gegenwärtige Zustand des Systems im Vordergrund sondern auch das Verständnis für die Entstehung und Entwicklung des Systems.



# Abstract

Our knowledge about the structure of planetary systems is still changing. The Solar System with its eight planets, the inner asteroid belt, as well as the Edgeworth-Kuiper belt at the outer rim was considered as the prototype of a planetary system. With the discovery of hot Jupiters or massive dust disks around other stars, this concept was called into question. Because of limitations in observational techniques at first only the most extreme examples have been discovered, and in most cases only systems either with planets or a debris disk are known. But in some systems both components – planets and debris disks – have been identified. For these systems we introduce the term “full planetary system”.

In this work the architectures of full planetary systems have been studied. Therefore, we chose two examples: HR 8799 and  $\varepsilon$  Eridani. The first one is a multiplanet system, where an inner and an outer dust disk are known. Their outer and inner edges, respectively, are formed by four massive gas giants in between. We investigated the stability and orientation of the system with N-body simulations. Further, we tried to constrain the location, extension and mass of the disk by analyzing the spectral energy distribution. During the comprehensive analysis we also considered the age and inclination of the star, as well as the masses of the planets.

For  $\varepsilon$  Eridani we addressed the question of what might be the origin of the warm dust near the star. A belt of planetesimals as an in-situ source of dust would be implausible, since such a belt would be dispersed by the inner planet within a short period of time. We have shown that a sufficient amount of dust can be transported inward by Poynting-Robertson and stellar wind drag from the cold massive outer disk to the inner warm region, explaining the observations.

The third part searches for debris disk candidates in systems with transiting planets. This is of special interest, since no debris disks in transit systems are known to date, but above all because transit systems allow the direct determination of planetary properties, such as the mass, radius and density. Further, a transit event sheds light onto the planetary atmosphere and thus gives an insight into the inner structure. The discovery of debris disks in systems with transiting planets would help to clarify the formation of planets. In the *preliminary* data release of the *WISE All-Sky Survey* we found two candidates for debris disks in transit systems, but these candidates have not been confirmed in the *final* release of the WISE catalog.

With these examples of full planetary systems we show, on the one hand, which diverse architectures are known so far, and on the other hand, which conclusions one can draw from a comprehensive analysis of all components in a full planetary system, comprising the star, the planets, and the dust. Thereby not only the current state is of interest, but also the understanding of the formation and evolution of planetary systems.



# Contents

Danksagung	i
Kurzfassung	iii
Abstract	v
<b>1 Introduction</b>	<b>1</b>
<b>2 Fundamentals</b>	<b>9</b>
2.1 Planet formation & debris disks . . . . .	9
2.1.1 Protoplanetary disks . . . . .	9
2.1.2 Formation of planets . . . . .	12
2.1.3 Debris disks . . . . .	14
2.2 Dynamics . . . . .	16
2.2.1 Two-body problem . . . . .	16
2.2.2 N-body problem . . . . .	18
2.2.3 Photo-gravitational forces . . . . .	20
2.2.4 DISCO & MERCURY6 . . . . .	23
2.3 Collisions . . . . .	24
2.3.1 Collisional physics . . . . .	25
2.3.2 Collisions in debris disks . . . . .	27
2.3.3 ACE . . . . .	28
2.4 Thermal Emission . . . . .	29
2.4.1 Thermal emission of a dust disk . . . . .	29
2.4.2 SEDUCE & SUBITO . . . . .	31
2.5 Masses from evolutionary models . . . . .	32
<b>3 HR 8799</b>	<b>34</b>
3.1 The central star . . . . .	35
3.1.1 Age . . . . .	35
3.1.2 Rotational period and inclination . . . . .	37
3.2 Planets . . . . .	38
3.2.1 Masses from models . . . . .	38
3.2.2 Masses from stability requirement . . . . .	40
3.3 Dust and the planetesimal belts . . . . .	50
3.3.1 Observations . . . . .	50
3.3.2 Interpretation . . . . .	51
3.4 Dynamical interactions between planets and planetesimals . . . . .	55
3.5 Conclusions and discussion . . . . .	58
3.5.1 Conclusions . . . . .	58
3.5.2 Prospects for future observations . . . . .	60
3.5.3 Origin and status of the system . . . . .	61

<b>4</b>	<b><math>\varepsilon</math> Eridani</b>	<b>63</b>
4.1	Model setup . . . . .	64
4.1.1	Method . . . . .	64
4.1.2	Stellar properties . . . . .	65
4.1.3	Dust grain properties . . . . .	65
4.1.4	Radiation pressure and stellar wind . . . . .	65
4.1.5	Sublimation . . . . .	66
4.2	Dust in the outer and intermediate region . . . . .	67
4.2.1	Model . . . . .	67
4.2.2	Results . . . . .	68
4.3	Dust in the inner region . . . . .	70
4.3.1	Model . . . . .	70
4.3.2	Results . . . . .	71
4.4	Spectral energy distribution . . . . .	72
4.4.1	SED from the outer and intermediate regions . . . . .	72
4.4.2	SED from the inner region . . . . .	74
4.4.3	SED from the entire disk . . . . .	76
4.4.4	Connecting outer and inner regions . . . . .	78
4.5	Surface brightness profiles . . . . .	78
4.6	Conclusions . . . . .	80
<b>5</b>	<b>Debris dust in systems with transiting planets</b>	<b>82</b>
5.1	Search for dust . . . . .	83
5.1.1	IRAS, ISO, Spitzer, and AKARI . . . . .	83
5.1.2	WISE . . . . .	84
5.2	Analysis of excess candidates . . . . .	85
5.3	Presumed dust belts . . . . .	88
5.4	Conclusions and discussion . . . . .	89
<b>6</b>	<b>Conclusions</b>	<b>93</b>
6.1	HR 8799 . . . . .	93
6.2	$\varepsilon$ Eridani . . . . .	95
6.3	Dust in systems with transiting planets . . . . .	96
	<b>References</b>	<b>99</b>
	<b>Ehrenwörtliche Erklärung</b>	<b>119</b>
	<b>Lebenslauf</b>	<b>121</b>

# Chapter 1

## Introduction

Astronomy is one of the oldest natural sciences. The beginnings date back to prehistoric times and the formation of cultures (i.e., roughly 5 000 years ago). From then until today, we found that the Earth is neither a disk nor the center of our Solar System. We discovered that we are living on one of four small rocky planets next to four huge gas giants farther out in a 4.5 billion years old planetary system around an ordinary dwarf star called the Sun. The Sun orbits around a super-massive black hole amongst another 100 billion stars in the Milky Way, which is again just one of billions of galaxies in our visible universe.

With powerful telescopes and high-tech satellites we can take a deep look into space and therefore back in time to the beginning of the universe, but the theory of formation and evolution of our planetary system is still challenging. For a long time our Solar System was unique and the only example to test the theory of planet formation. Even the existence of planetary systems other than the Solar System was just a scientific speculation. We knew that the architecture of the Solar System is complex but somehow well-ordered. The inner few AU are populated with four small rocky, terrestrial planets, while farther out (5–30 AU) we find four gas giants. In between and on the fringe of the system we find debris left over from planet formation. The (main) asteroid belt comprise planetesimals which failed to grow to a planet because of the perturbations by nearby Jupiter (e.g., Safronov, 1969; Wetherill, 1980), while the planetesimals of the Edgeworth-Kuiper belt (EKB) did not form planets, since the density of the solar nebular was too low (e.g., Safronov, 1969; Lissauer, 1987; Kenyon & Bromley, 2008). Most of the objects move on almost circular orbits and nearly in the same plane.

The discovery of the first planet (Mayor & Queloz, 1995) and that of a debris disk (Aumann et al., 1984) around other main sequence stars changed the picture dramatically. The planet was massive and very close to the host star (so called *hot Jupiter*), and the disk was several orders of magnitude more massive than the asteroid belt and the EKB. Their discovery induced the question: “How do these planetary systems form, and what is their typical structure?”

Today several hundred planetary candidates are known (851, [exoplanet.eu](http://exoplanet.eu), 2012-11-21, Schneider et al., 2011) with various orbits and masses. Most of them are found to be Neptune or Jupiter-like gas giants within a few AU of the star, but in all likelihood this is a bias due to limitations in observational techniques. It is estimated that at least 50% of the solar-type stars host one or more planets (Mayor et al., 2011). There are also several hundred debris disks known, and estimations from Herschel observations suggest that at least 25% of the stars host a debris disk (Eiroa et al., in prep.). With ongoing technological progress and new telescopes (VLT/SPHERE, VLTI/PIONIER, ALMA, JCMT/SCUBA2, GPI/GeminiS, E-ELT, JWST), one expects to find more (super-) earth-like planets and faint debris disks such as EKB around other stars.

As it will be explicated in Sect. 2.1 the formation of planets and debris disks are connected, and thus, it is a reasonable thought that the occurrence of planets and debris disks is correlated. However, observational studies (Greaves et al., 2004; Beichman et al., 2005b; Greaves et al., 2006; Moro-Martín et al., 2007; Bryden et al., 2009; Kóspál et al., 2009) did not find such a correlation. One reason for this negative result may be that we still are only able to find rather massive planets or disks. Assuming the Solar System presents a typical planetary system, if at all only the gas giants would have been found. Comparable debris disks in an analogue of the Solar System are still below current detection limits (Vitense et al., 2012). While surveys for transit systems are already quite successful in finding lower mass planets, their caveat is that these transit systems are usually found at several hundred parsecs. At such distances it is rather difficult to find debris disks. At the time of these previous studies the situation was even more severe, since the detection limit was even higher. Though, recent studies claim that there might be a correlation between low mass planets and debris disks. An analysis of 60 nearby G-stars shows that the five systems with high-mass planets do not show evidence of an infrared (IR) excess<sup>1</sup>, while four out of six system with low-mass planets do show an IR excess (Wyatt et al., 2012). Further, Raymond et al. (2011) found in their simulations that systems with massive debris disks are an indication for an efficient formation process of terrestrial planets. Systems with a massive outer debris disk and stable giant planets may contain high amount of warm inner dust due to scattering of comets from the outer region to the inner one, while systems with unstable giant planets are likely to deplete most of the planetesimal belts and disturb the formation of terrestrial planets.

Irrespective of whether there is a correlation or not, to find systems comprising one or more planets, as well as debris disks is of great value. Such systems we call here *full* or

<sup>1</sup>The SED shows more flux than expected from stellar photosphere (see also Sect. 2.4).



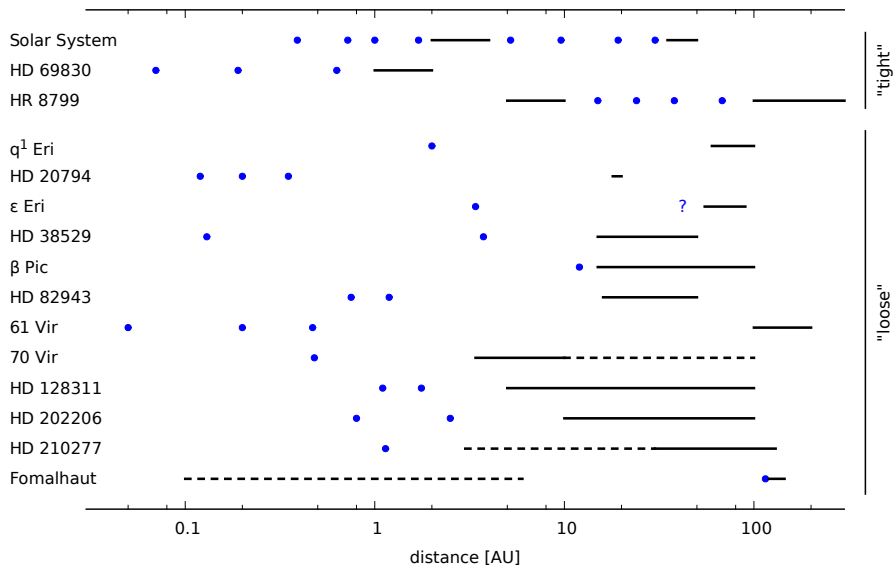


**Figure 1.1:** Sketch of architectures of full planetary systems with known disk locations (*solid lines*), while planets are represented by *dots*. Unknown disk extensions are depicted with *dashed lines*.

*complete* planetary systems. They give us the opportunity to study the interactions of planets and debris disks which have the same history and evolution.

Based on the work of Maldonado et al. (2012) we found 36 systems in the literature (2012-09-27), having at least one planet and showing an IR excess (Tab. 1.1). While in all of these systems the location of the planets is known, only in 15 can the location of the dust be estimated (Fig. 1.1). We find it convenient to classify the architecture of these systems into two groups (Krivov, pers. comm.).

We classified one group of full planetary systems as “*tight systems*”, which are densely packed with planets, and with one or several debris disks. The Solar System and HR 8799 (Marois et al., 2008, 2010; Reidemeister et al., 2009) are the best examples to depict this category. The status of HD 69830 (Lovis et al., 2006; Payne et al., 2009) as a third tight system is arguable, since all components are within a few AU with a lot of space for additional components farther out. Due to mutual interactions between the components, it can be possible in such tight systems, by combining the analysis of stellar, planetary, and dust data, using models and data from laboratory, to ascertain – or at least constrain – the system’s age, orientation, masses and orbits of planets, the location of dust belts, etc. (e.g., Reidemeister et al., 2009).

We call the other group “*loose systems*”, which have a large gap between the planet(s) and the disk, or at least a lot of space for additional objects. These loose systems raise

**Table 1.1:** List of known *full planetary systems*. When the dust could be located, the systems were classified either as *tight* (T) or as *loose* (L) cases. Transit-planet candidates with warm dust, which are discussed in Chap. 5, are not included.

Identifier		Sp Type	# of planets	class	references
	Solar System	G2 V	8	T	
HD 69830		G8+ V	3	T	(1)
HD 218396	HR 8799	A5 V	4	T	(13)
HD 10647	q <sup>1</sup> Eridani	F9 V	1	L	(11)
HD 20794		G8 V	3	L	(16)
HD 22049	ε Eridani	K2 V <sub>k</sub>	1	L	(7)
HD 38529		G4 V	2	L	(12)
HD 39060	β Pictoris	A6 V	1	L	(6)
HD 82943		F9 VFe+0.5	2	L	(12)
HD 115617	61 Virginis	G7 V	3	L	(14)
HD 117176	70 Virginis	G4 V	1	L	(15)
HD 128311		K3 V	2	L	(12)
HD 202206		G6 V	2	L	(12)
HD 210277		G0 D	1	L	(5)
HD 216956	Fomalhaut	A4 V	1	L	(8)
	GJ 581	M2.5 V	4		(10)
HD 142		F7 V	2		(3)
HD 1461		G0 V	2		(9)
HD 19994	94 Ceti	F8 V	1		(10)
HD 38858		G4 V	1		(2)
HD 40979		F8 D	1		(10)
HD 45184		G1.5 V	1		(9)
HD 46375		K1 IV	1		(10)
HD 50499		G1 V	1		(10)
HD 50554		F8 V	1		(10)
HD 52265		G0 V	1		(10)
HD 73526		G6 V	2		(10)
HD 104067		K3 V <sub>k</sub>	1		(9)
HD 108874		G9 V	2		(4)
HD 130322		K0 V	1		(4)
HD 137759	ι Draconis	K2 III	1		(10)
HD 178911B		G5 D	1		(10)
HD 187085		G0 V	1		(4)
HD 192263		K2.5 V	1		(4)
HD 215152		K0 D	2		(10)
HD 216435	τ <sup>1</sup> Gruis	G0 V	1		(10)

**References for planets:** [exoplanet.eu](http://exoplanet.eu)

**References for IR-excess:** (1) Beichman et al. (2005a), (2) Beichman et al. (2006), (3) Bryden et al. (2009), (4) Dodson-Robinson et al. (2011), (5) Eiroa et al. (2011), (6) Golimowski et al. (2006), (7) Greaves et al. (2005), (8) Kalas et al. (2005), (9) Koerner et al. (2010), (10) Kóspál et al. (2009), (11) Liseau et al. (2010), (12) Moro-Martín et al. (2010), (13) Su et al. (2009), (14) Tanner et al. (2009), (15) Trilling et al. (2008) (16) Wyatt et al. (2012)

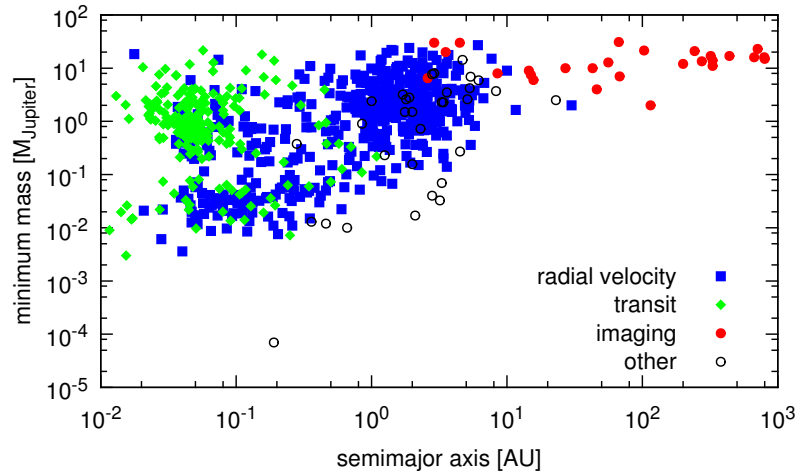


**Figure 1.2:** Planetary mass over semimajor axis for different detection methods. Other methods (black circle) comprise microlensing, astrometric measurements, and pulsar timing. Data was taken from `exoplanet.eu` (2012-11-29).

the question, of whether the void has been caused by collisional erosion (Wyatt et al., 2012) or has been cleared by planets (Faber & Quillen, 2007). And for the latter case are they still hidden in the gap and not discovered yet, or did they migrate through the disk? As good examples for loose systems may serve  $q^1$  Eridani or Fomalhaut.

While we know several hundreds of planetary systems and a comparable number of debris disks, there are only a few dozen full planetary systems identified and most of them are identified as “loose” in the first place. One reason for this result may be that the observational techniques for planets and those for debris disks probe different distances to the star. The most successful planet searching techniques (RV & transit) are most efficient within 10 AU (see Fig. 1.2), though dust is typically found at orbital distances of tens of AU (e.g., Bryden et al., 2009). Further, massive objects are more likely to find than earth-sized planets or faint disks like Asteroid or Kuiper belts. Until today it is not definite if the gap is an observational bias or a real feature of a typical planetary system which has been cleared during planet formation or the system’s evolution (e.g., migration of a planet through the disk, planet-planet scattering, or grinding of the disk from inside out due to stirring).

In general, due to mutual interactions between planets, planetesimals and dust there is great potential to get more information about the single components instead of studying a uniform system. For example, a known orbit and mass of a planet could constrain the location of dust in an unresolved debris disk. Vice versa, a configuration with a resolved disk and an vaguely known planet could make it possible to constrain

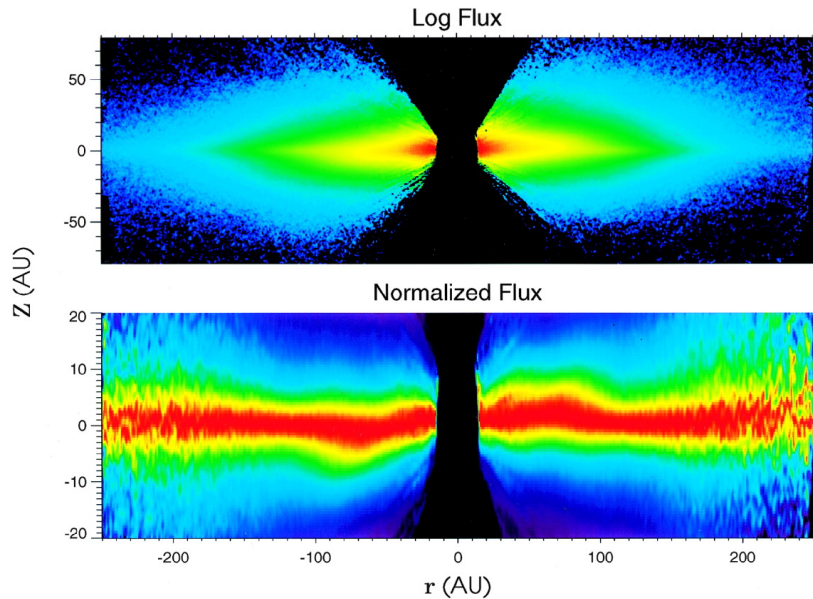


**Figure 1.3:** STIS/CCD coronagraphic images of the  $\beta$  Pic disk (WedgeB2 observations). *Top:* The disk at a logarithmic stretch. *Bottom:* The disk normalized to the maximum flux, with the vertical scale expanded by a factor of four. The expanded vertical scale exaggerates the warp in the inner region of the disk (from Heap et al., 2000, their Fig. 8).

orbital parameters, such as the distance to the star, eccentricity, orientation of the orbital plane or mass of the planet by analyzing the shape and stability of the adjacent dust ring. This scenario was already utilized for the well known systems  $\beta$  Pictoris (Freistetter et al., 2007) and Fomalhaut (Quillen, 2006; Chiang et al., 2009).

The very prominent disk around  $\beta$  Pictoris shows a warp within  $\approx 100$  AU (Burrows et al., 1995; Mouillet et al., 1997; Heap et al., 2000; Golimowski et al., 2006, see Fig. 1.3), which was attributed to a giant planet misaligned with the main disk (Augereau et al., 2001; Freistetter et al., 2007). Meanwhile, Lagrange et al. (2009, 2010) discovered a planet in the disk which is roughly consistent with the planet predicted before. This planet has been confirmed by several other observations (Currie et al., 2011b; Lagrange et al., 2012a,b; Chauvin et al., 2012).

Around Fomalhaut, a narrow elliptic dust ring at  $\approx 130$  AU with a clear offset is visible in scattered light (Kalas et al., 2005, see Fig. 1.4). The sharp inner edge was presumed to be sculpted by a planet. Then Kalas et al. (2008) found an object near the inner edge which could be the presumed planet. Dynamical analyses of the object and the disk imply that the mass of the planet needs to be less than three Jupiter masses (Chiang et al., 2009; Boley et al., 2012). Although a non-detection with Spitzer/IRAC confirms that Fomalhaut b needs to be  $\lesssim 3M_{\text{Jup}}$ , this also puts the observation by

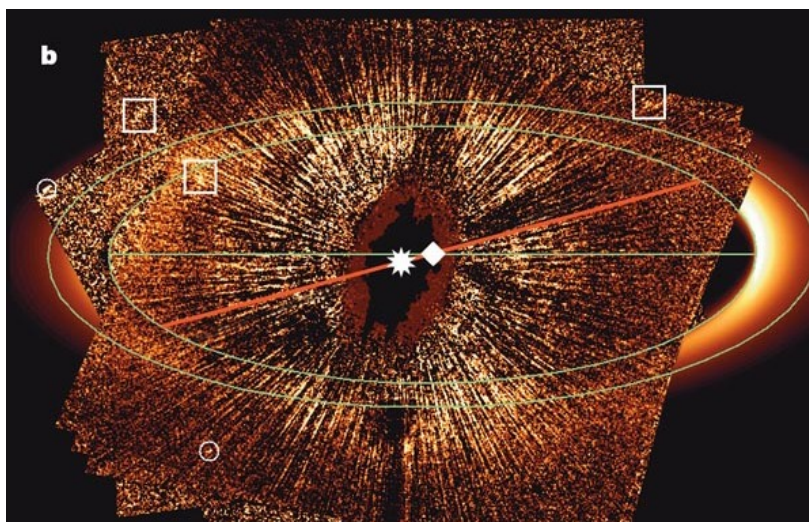


**Figure 1.4:** False-color residual image after subtracting a model of a dust belt. Green lines trace the projected boundaries of the detected belt (133–158 AU). The white diamond and asterisk mark the centers of the belt and the star, respectively. The horizontal green line traces the belt semimajor axis, whereas the red line traces the vector between the belt and star centers. White boxes and circles mark extended objects and background stars, respectively (from Kalas et al., 2005, Fig. 1).

Kalas et al. (2008) and its interpretation as a planet into question (see Janson et al., 2012). To determine the true nature of the spot, the Hubble Space Telescope will have to monitor it for several years (Cowen, 2012).

A third example for the benefit of full planetary systems is HD 69830. Here one finds an opportunity to test planet formation and evolution. Beside three radial-velocity planets close to the star ( $< 1$  AU) (Lovis et al., 2006), the system shows a  $24 \mu\text{m}$  excess (Beichman et al., 2005a), indicating a massive disk of warm dust, located at  $\approx 1$  AU. Payne et al. (2009) used dynamical models of planetary formation and migration in combination with those for the sculpting of a dust-producing planetesimal disk. With this method they study the outcome and constraints of planet formation on the structure and evolution of the debris disk and vice versa.

In the spirit of these studies we focused on two other full planetary systems, HR 8799 and  $\varepsilon$  Eridani. For both systems we wanted to achieve a better understanding of their properties and structure by detailed analyses of the planets, the disks, and the interactions between these components. Further, we tried to increase the number of known full planetary systems by searching for warm dust around systems with transiting planets. Altogether, these activities constitute important steps to constrain planet formation theories.

While HR 8799 was known to have a massive dust disk (Sadakane & Nishida, 1986), Marois et al. (2008) presented the direct image of three giant planets in the system (HR 8799 b, c, d). Since the images of the planets just show the projected distances, and orbital coverage was rather short, we tried to constrain the real orientation and therefore the real distance of the planets. This was achieved with a synthetic analysis of the star, the planets, and the debris disks (Reidemeister et al., 2009). For example we constrained the stellar rotation and deduced inclination of the star and possibly the orbits. We analyzed the stability of the planetary orbits, by varying their masses and the orientation of the orbits. We also tested our stable solution with the position of the dust rings we got from modeling of the thermal emission. This work is presented in Chap. 3.

Chapter 4 contains our analysis of  $\varepsilon$  Eridani (Reidemeister et al., 2011). This system shows a puzzling feature. The spectral energy distribution (SED) reveals the presence of a significant amount of warm dust within a few AU (Backman et al., 2009), and in the same distance a radial velocity (RV) planet has been detected (Hatzes et al., 2000). The planet would have dispersed a ring of planetesimals within 10 AU (Brogi et al., 2009), which could have been the source for the dust. This raised the questions of what and where the origin of the warm dust is. We suggest a scenario where dust is produced in the outer ring and transported inward by drag effects caused by strong stellar wind. As a first step, we modeled the outer disk including collisions and transport mechanisms. We found that a great deal of small particles are transported inward. In a second step, we analyzed the behavior of small dust grains in the vicinity of the RV planet and we modeled the resulting SED in comparison to the observations. Our intent was to distinguish between two different orbital solutions of the planet which are given in the literature (Benedict et al., 2006; Butler et al., 2006).

In Chap. 5 our search for additional full planetary systems is described. Here, we focused on systems with transiting planets. On the one hand, no debris disks had been found there, and on the other hand, the special orientation of transit systems offers valuable insights in the planetary properties. Therefore, we searched the literature if transit systems had been observed with IRAS, Akari, or Spitzer. We only found a few systems and none of them showed an excess. But with the release of the preliminary WISE catalog in April 2011, we were able to find several candidates. Finally, our analysis of the SED quarried two candidates with excesses of  $\gtrsim 3\sigma$ .

The conclusions in Chap. 6 form the end of this work.

# Chapter 2

## Fundamentals

In this chapter the background information needed for the understanding of this thesis will be presented. We begin in Sect. 2.1 with a concise summary of the current state of planet formation theory and a definition of debris disk, allowing the reader to put this work into context. In Sect. 2.2 the dynamics of planetary systems are treated. First the analytic solution of the two-body problem and the orbital elements, which are used to describe an orbit in space, will be presented. Next the N-body problem is discussed and an approach to deal with it. The next part of this section is dedicated to non-gravitational forces, such as radiation pressure, Poynting-Robertson drag, and stellar wind drag. The section closes with an overview about the programs DISCO and MERCURY6 which are used to calculate the dynamics throughout this work. Section 2.3 treats the problem of collisions in debris disks and our implementation of a statistical approach into the program *ACE*. Section 2.4 deals with the theoretical background of thermal emission of dust particles in a debris disk, allowing us to calculate the spectral energy distribution (SED) and surface brightness profiles. Therefore, we used the codes SEDUCE and SUBITO, respectively. Section 2.5 briefly describes evolutionary models, which are used to derive planetary masses from luminosities or temperatures.

### 2.1 Planet formation & debris disks

#### 2.1.1 Protoplanetary disks

Planet formation can be seen as a byproduct of star formation. When an interstellar gas cloud collapses it forms a protostellar core and a flat disk, due to conservation of angular momentum and the vertical component of the protostellar gravitation. This gas disk is called *protoplanetary disk* (PPD).

The typical protoplanetary disk is geometrically flat ( $h \ll r$ , but flared) and has a radius up to several hundred AU (Williams & Cieza, 2011, and references therein). Due to the flaring the protostar can illuminate the whole surface of the disk. The

gas accretes onto the star due to turbulent viscosity which may be induced by magnetorotational instabilities (MRI, Balbus & Hawley, 1991), baroclinic instabilities (BI, Klahr & Bodenheimer, 2003; Klahr, 2004), vortices (Lithwick, 2009), or gravitational torques (Vorobyov & Basu, 2008). Which of these effects is the dominant one causing viscosity in the disk is still under debate (Chiang & Youdin, 2010).

The gas disk does not only contain gas in form of molecular hydrogen and helium, but also some solid grains of sub-micrometer sizes. From the composition of interstellar gas clouds one knows a dust to gas ratio of  $\sim 1/100$  (Hildebrand, 1983). These solids are a crucial element in the process of planet formation. Not only are they the basic modules from which the planets or their cores are built, they also determine – for example – the opacity and therefore the temperature of the disk. Although one can assume that the gas has the same elemental abundances as the star, the composition of solids in the disk depends on the distance to the star. While materials like Forsterite already condense from gas phase to solids at temperatures over 1000 K, other materials such as water, ammonia or methane need temperatures below 100–200 K (Lodders, 2003). For example, around a solar type star the dust grains within  $\sim 3$  AU are composed of rocky material (Lodders, 2003). Farther outward, the temperature drops below  $\sim 150$  K (referred to as “snowline”) and volatile substances condense into solid ice grains.

In the beginning of the evolution the small grains are well mixed within the gas, i.e., gas and dust behave like a single fluid. Due to the vertical component of the gravitation the solids sink to the midplane, while the gas in the disk is supported against gravity by an outward pressure gradient. Since the settling velocity increases with particle size, the larger grains overrun the smaller ones. On their way to the midplane they collide and stick with the smaller – and therefore slower – particles and become even larger (Safronov, 1969). The time scale of settling and growth is found to be extremely rapid ( $\sim 10^3$  yr) (Dullemond & Dominik, 2005). This raises the problem, that growth of particles with sub- and micrometer sizes is still observed in systems as old as some few megayears (van Boekel et al., 2004). This problem can be solved by taking turbulences into account. When the dust settles in the midplane, the dust to gas ratio increases and the statement, that the dust is well mixed, is not valid anymore. Now, the dust layer needs to be treated as a second fluid and due to Kelvin-Helmholtz instabilities turbulences occur at the boundary layer. These turbulences stir up particles with sizes up to 1 mm. While larger particles settle in the midplane, smaller are still distributed within the gas. An additional effect is, that there are a significant amount of small fragments due to collisions (Brauer et al., 2008).



Due to the pressure gradient the gas orbits the star at a slightly sub-Keplerian velocity. While very small particles are strongly coupled to the gas, the coupling is reduced with increasing sizes. The solids are used to orbit with Keplerian velocity, and thus, they experience a “head wind”. This is a great challenge for planet formation. At a few AU the radial drift, due to the gas drag, reaches its maximum for meter-sized objects, and they will fall on the star within  $\sim 10^3$  orbits (Weidenschilling, 1977). This causes an additional problem. Since the typical relative velocities for bodies in the centimeter-to-meter-size range are several tens of meters per second (Cuzzi & Weidenschilling, 2006; Dominik et al., 2007), the sticking probability is rather low at these velocities and the boulders get lost faster than they can grow to significantly larger sizes (Blum & Wurm, 2008; Güttler et al., 2010; Zsom et al., 2010).

To overcome this *meter barrier* Johansen et al. (2007) proposed a mechanism, where swarms of decimeter-sized objects get caught in high pressure regions in the turbulent gas. Streaming instabilities can amplify these regions and objects of 100 km can be built within very short time scales. As additional evidence Morbidelli et al. (2009) concluded from the observed size distribution of the asteroid belt in the Solar System that the formation of asteroids need to have made a quick jump from small particles to big objects. Similar results were obtained for the EKB (Vitense et al., 2012). However, Weidenschilling (2011) showed that the size distribution of objects in the asteroid belt could also be explained by planetesimals with initial sizes of hundred meters. Another possibility to overcome the meter barrier was examined by Okuzumi et al. (2012), analyzing the porosity evolution of dust aggregates. They show that dust can evolve to highly porous particles and that the growth of these particles by direct collisions is faster than the inward drift.

As we can see, due to its complex physics – involving the conditions in the gas disk, such as the interaction of the gas and dust layer, the material properties of the dust (porosity, material strength, etc.) – this topic is still under heavy discussion<sup>2</sup>. Anyway, the presence of planets and asteroids in the Solar System and the empirical observations of dust and planets in extrasolar systems, show us that the planetesimal formation process is rather robust.

---

<sup>2</sup>A general problem for such sizes is that it is rather difficult to verify theoretical models with laboratory experiments. Already computer simulations for small particles show higher sticking probabilities than laboratory experiments (e.g., Wada et al., 2011).

## 2.1.2 Formation of planets

At the moment there exist two competing formation theories. On the one hand, there is the theory of *core accretion*, where a solid core of several earth masses forms first and then a gaseous envelope accretes onto the core. On the other hand, in the theory of *disk instability* a massive disk can become unstable due to self-gravity, forming fragments, which collapse into massive planets.

### Core accretion

After the meter-size barrier is taken, the dominant process for the further evolution is the mutual gravitational interaction and collisions between the planetesimals. On the one hand, cumulative mutual gravitational interactions will excite the random velocity in the disk by viscous stirring or dynamical friction. On the other hand, gas drag and inelastic collisions will result in energy dissipation and therefore damping of the eccentricities and inclinations.

The early stage of planetesimal growth is referred to as *runaway growth* (Greenberg et al., 1978), the largest objects grow more rapidly than their smaller neighbors. Due to dynamical friction the eccentricities and inclinations of large planetesimals are smaller than those of small planetesimals (Stewart & Wetherill, 1988). Additionally, gravitational focusing is more effective for large planetesimals (Wetherill & Stewart, 1989). When a protoplanet dominates the velocity distribution of the smaller background planetesimals ( $M/m \sim 100$ ) their random velocities will increase. Thus, the gravitational focusing becomes less effective and furthermore, neighboring planetesimals are scattered away, producing a gap in the spatial distribution of the planetesimals. As a result, the growth switches to a slower, self-limiting *oligarchic growth* (Ida & Makino, 1993).

The outcome of the growth can split into two categories depending on the distance to the star. The border can be drawn at the *snowline*, which defines the distance after which the temperature in the disk is low enough that gaseous hydrogen compounds (water, ammonia, methane) can condensate to ice particles. Inside the snowline there are 3–4 times less solids than outside this line (Hayashi, 1981), therefore only terrestrial planets can form via collisional agglomeration of planetary embryos over 10–100 Myr (Chambers, 2001; Kenyon & Bromley, 2006; Raymond et al., 2006, 2009; O’Brien et al., 2006). Outside the snowline the protoplanets can reach several earth masses, and when the planet embryo reaches a critical core mass of  $\sim 10M_{\oplus}$ , the gaseous envelope can

no longer sustain a hydrostatic equilibrium and it collapses onto the core, forming a gas giant (e.g., Mizuno et al., 1980; Bodenheimer & Pollack, 1986; Pollack et al., 1996; Ikoma et al., 2001). While the time scale for core accretion is rather short ( $\sim 10^5$  yr), the hydrostatic growth of the envelope usually takes several million years. When the mass of the envelope exceeds the mass of the core, a runaway growth of the envelope starts. This process is only limited by the supply from the disk and eventually it ends either by tidal effects of the planet on the disk or by global dispersal. In the outer most region of the system the growth time scale exceeds the lifetime of the disk and only debris of planet formation remains.

### Disk instability

A massive disk can become unstable when the following relation is fulfilled:

$$Q = \frac{\Omega c_s}{\pi G \Sigma} \lesssim 2, \quad (2.1)$$

where  $Q$  is the *Toomre parameter* (Toomre, 1964),  $\Omega$  is the orbit frequency,  $c_s$  is speed of sound,  $G$  is the gravitational constant, and  $\Sigma$  is the surface density. But that is not sufficient to create planet forming fragments, because the instability generates density waves which transport angular momentum outward via gravitational torques. This also implies that there is material transport, which would heat the disk and mitigate the instability. To fragment the disk it has to cool efficiently within time scales comparable to the local disk orbital period (Gammie, 2001). The most likely region for fragmentation is around 50 to 100 AU, since there the opacity is low enough. The resulting mass of planets would be several Jupiter masses (super Jupiters or brown dwarfs, see also Rafikov, 2005). If the disk can dissipate its energy more efficient than with radiation (e.g., convection), this could lead to smaller distances. The advantage of the disk instability model is, that the time scales of formation is rather short, compared to the core accretion model (Boss, 1997).

### Migration

The fact that giant planets exist much closer to the star than the snowline (“Hot Jupiters”), can be explained by migration after or during planet formation. Planets with low masses interact with the disk and induce spiral density waves in the surrounding gas. While the inner arm pushes the planet outward, the outer arm pushes

the planet inward. In most cases the strength by the outer arm is larger and the planet migrates inward (migration *type I*). The time scale is very short ( $\approx 10^4 \dots 10^5$  yr).

If the planet is sufficiently large ( $\gtrsim 10M_{\oplus}$ ), it opens a gap in the disk, stopping migration of type I. Nonetheless, material continues to flow into the gap, moving the planet and the gap further inward (migration *type II*). This happens on time scales of disk accretion and is assumed to explain the Hot Jupiters. Such a gap is also a barrier for smaller protoplanets, which get trapped in mean-motion resonances with the gap opening planet, stopping their migration (Thommes, 2005).

Another mechanism can be gravitational scattering, either by planet-planet interactions (Raymond et al., 2008, and references therein) or by scattering small planetesimals (Ida et al., 2000; Kirsh et al., 2009). Since the process is chaotic, the result can move planets inward or outward.

### 2.1.3 Debris disks

While nearly all young stellar objects with an age below  $\sim 1$  Myr show evidence for a PPD, with increasing age (some million years) the fraction of stars with a disk decreases (Hillenbrand et al., 1998; Haisch et al., 2001; Mamajek et al., 2004). Around stars with an age of around ten million years nearly no PPDs can be observed anylonger. Accordingly, the time scale of giant planet formation is several million years. Further, the dissipation of the disk seems to be a rapid process ( $\sim 10^5$  yr) (Skrutskie et al., 1990; Wolk & Walter, 1996; Andrews & Williams, 2005). This excludes accretion as the dominant lost mechanism. A plausible mechanism could be *photoevaporation*, where ultra-violet (UV) or X-ray radiation heats the surface of the disk, until the kinetic energy of the gas molecules exceeds the gravitational potential of the disk and are then blown away (Hollenbach et al., 1994). Once more material is blown away than accreted, an annular gap forms and the inner disk is cut off from resupply. Finally, the inner disk becomes optical thin to the stellar UV flux, which then directly illuminates the inner edge of the outer disk. This leads to an increasing inner gap and dissipation of the whole disk within a few  $10^5$  yr (Clarke et al., 2001; Alexander et al., 2006).

What remains eventually is a planetary system and probably a disk of planetesimals which did not form planets, either there was not enough time before the gas disk dissipates or the planetesimals got disturbed by an adjacent planet. These disks are called *debris disks*. While the planetesimals cannot be observed, due to their small

surface area, a disk of dust particles is still observable at infrared and sub-millimeter wavelengths.

The dust in a system, older than some tens of million years, cannot be primordial, since various effects (such as collisions and Poynting-Robertson drag) would have removed it from the system within this time scale. Due to the fact that at least 15% of the stars with ages over 10 Myr show an IR-excess (Trilling et al., 2008; Hillenbrand et al., 2008), the sources of the dust are expected to be collisions of long-lived planetesimals. Since the gas is gone, there is no damping and stirring by planets or large boulders increases relative velocities up to several hundred meters per second. At these velocities the collisions are usually destructive, producing a cascade of fragments of various sizes. Thus, the debris are ground from planetesimals and boulders over pebbles to micron-sized grains, compensating the loss and filling the disk with the dust which may be still observable after millions and billions of years. For a more detailed description of collisions and their outcome see Sect. 2.3.

### **Warm dust & terrestrial planets**

While most of the observed debris disks are found at several tens of AU, up to some hundred AU at the outer boundary of the planetary system, some systems show evidence for warm dust and an inner belt, such as the zodiacal dust cloud and the asteroid belt in the Solar System. Raymond et al. (2011) claim that such an inner belt should be a good indicator for terrestrial planet formation. On the one hand, this is evidence that there was enough material to form planetesimals generating dust, which can still be observed. And thus, probably there will also exist terrestrial planets. On the other hand, a system with an inner belt should be evidence of a “calm” formation of possible giant planets. Which means that the orbits of giant planets during the formation process in the outer region did not undergo an event of planet-planet scattering, and so they did not disturb the formation process in the inner region. This is also important for the outer region since massive disks are anti-correlated with strongly-scattered giant planets.

## 2.2 Dynamics

### 2.2.1 Two-body problem

The simplest case in a planetary system is the two body problem. With Newton's law of gravity

$$\vec{F}_G = -G \frac{m_1 m_2}{r^2} \frac{\vec{r}}{r} \quad (2.2)$$

where  $G$  is the gravitational constant, and  $\vec{r}$  is the distance vector from mass  $m_1$  to  $m_2$  one can derive that two objects move in Keplerian orbits. This means that the distance between these two bodies is

$$r = \frac{p}{1 + e \cos(\phi)} \quad (2.3)$$

with eccentricity  $e$ , semilatus rectum  $p$  and true anomaly  $\phi$ . The angle  $\phi$  is measured from the pericenter, the position of the minimum distance between  $m_1$  and  $m_2$  on the orbit, and the current position. Equation 2.3 is the general equation of a conic in polar coordinates. The three possible conics are:

ellipse	$0 \leq e < 1$	$p = a(1 - e^2)$
parabola	$e = 1$	$p = 2q$
hyperbola	$e > 1$	$p = a(e^2 - 1)$

where  $a$  is the semimajor axis, and  $q$  is the pericenter distance.

If  $e < 1$ , beside the true anomaly  $\phi$  astronomers make use of two equivalent angles, the eccentric anomaly  $E$  and the mean anomaly  $\mathcal{M}$ . While  $\phi$  gives the current position of the body,  $\mathcal{M}$  gives the position of a body moving with an average angular velocity  $n$  (mean motion) on a circular orbit with radius  $a$ :

$$\mathcal{M} = n(t - \tau) = \frac{2\pi}{P}(t - \tau), \quad (2.4)$$

with  $P$  – the orbital period and  $\tau$  – the time of pericenter passage. This anomaly has no geometric analog.

The eccentric anomaly  $E$ , is defined as the angle between the major axis of the ellipse and the radius from the center to the intersection point on the circumscribed circle

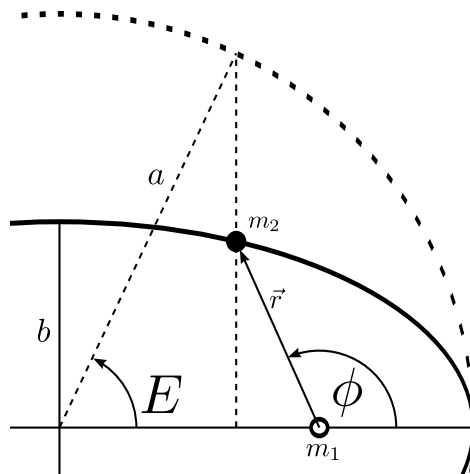


**Figure 2.1:** Geometric representation of the eccentric anomaly  $E$  in an ellipse.  $a$  and  $b$  are the semimajor and semiminor axis of the ellipse, while  $\phi$  is the true anomaly.

(see also Fig. 2.1). The true anomaly is connected to the eccentric anomaly over

$$\tan\left(\frac{E}{2}\right) = \sqrt{\frac{1-e}{1+e}} \tan\left(\frac{\phi}{2}\right), \quad (2.5)$$

and knowing the eccentric anomaly one can calculate the mean anomaly with Kepler's equation

$$\mathcal{M} = E - e \sin E. \quad (2.6)$$

With Eq. (2.3)–(2.6) one can find the orbital position at a given time.

### Orbit in space

To describe an orbit in space, three additional angles are needed: the inclination  $I$  of the orbit with respect to the plane; the longitude of ascending node ( $\Omega$ ), which is the angle between an arbitrary reference direction and the intersection line of the orbital plane and a reference plane; and the argument of pericenter ( $\omega$ ), which is the angle between the ascending node and the pericenter. All six orbital elements are sketched in Fig. 2.2. Further, one can define the longitude of pericenter  $\varpi = \Omega + \omega$  and the mean longitude  $\lambda = \varpi + \mathcal{M}$ .

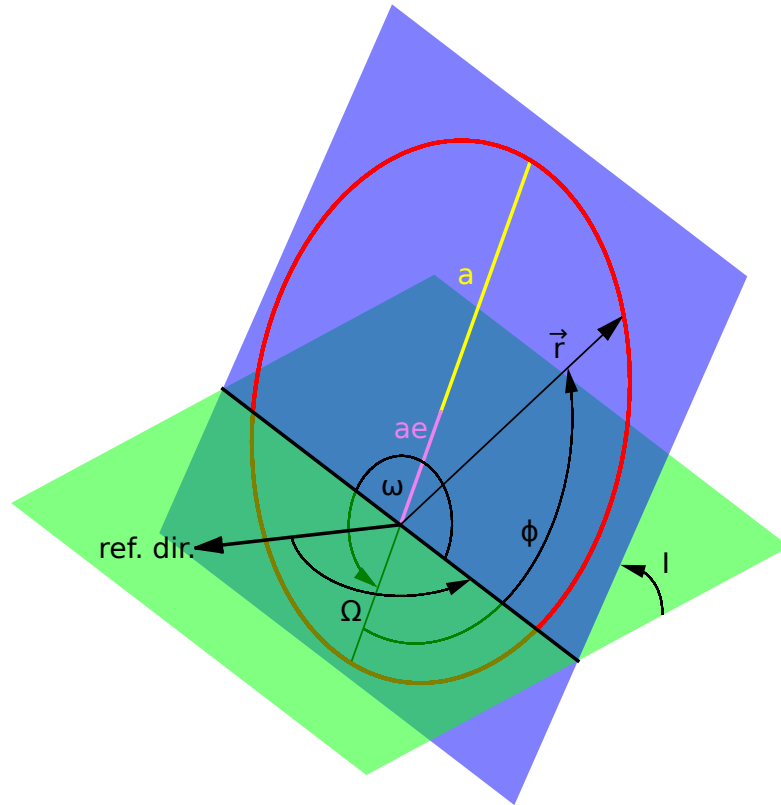


**Figure 2.2:** Orbital elements in space. The green plane is the reference plane, while the orbital plane is blue. The reference direction is arbitrarily chosen.

### 2.2.2 N-body problem

The generalization of the two-body problem to the N-body problem, makes a solution rather difficult. Although there is an analytical solution for the general three- and N-body problem, the solution is of little practical use: “[...] because the speed of convergence of the resulting solution is terribly slow” (Wang, 1991).

Therefore, one needs different ways to deal with this problem. One way is to analyze the disturbing function  $\mathcal{R}_i$  of an object with mass  $m_i$  around a central object  $M_c$ . Like in the two-body problem the object  $m_i$  moves in a potential of the central body

$$\mathcal{U}_i = \frac{G(M_c + m_i)}{r_i}. \quad (2.7)$$

By introducing additional objects  $m_j$  the mutual gravitational forces between  $m_i$  and  $m_j$  result in additional accelerations superposing the two-body acceleration between  $m_i$  and  $M_c$ . These additional accelerations of the mass  $m_i$  relative to the central mass



can be obtained from the gradient of the perturbing potential

$$\mathcal{R}_i = \sum_{j \neq i} G m_j \left[ \frac{1}{|\vec{r}_j - \vec{r}_i|} - \frac{\vec{r}_i \cdot \vec{r}_j}{r_j^3} \right], \quad (2.8)$$

the disturbing function. The resulting acceleration on a mass  $m_i$  with respect to the central mass  $M_c$  can be written as the gradient of the two potentials

$$\ddot{\vec{r}}_i = \vec{\nabla}_i(\mathcal{U}_i + \mathcal{R}_i). \quad (2.9)$$

Then one can analyze the properties of a Fourier expansion of the disturbing function. Therefore, the appropriate terms important for a particular problem are isolated, and one assumes that the time-averaged contribution of the other terms to the equation of motion are negligible.

As an example, an approach to analyze the *restricted three-body problem* is presented here. A central body ( $M_c$ ) is orbited by perturbing object  $m$  and a perturbed (primed) object  $m'$ . After a coordinate transformation from Cartesian coordinates to orbital elements one can show that the expansions – for example with Legendre Polynomials – will result in the general form

$$\mathcal{R} = Gm \sum S(a, a', e, e', i, i') \cos(\underbrace{j_1 \lambda + j_2 \lambda' + j_3 \varpi + j_4 \varpi' + j_5 \Omega + j_6 \Omega'}_{\varphi}), \quad (2.10)$$

where the D'Alembert relation applies ( $\sum_{i=1}^6 j_i = 0$ ).

While in an unperturbed case the orbital elements  $a, e, i, \Omega$  and  $\varpi$  do not change with time, but the mean longitude does, we consider these elements as slow moving or fast moving variables, respectively. Therefore,  $j_1 = j_2 = 0$  is classified as *long-term* or *secular perturbations*, and  $j_1 n + j_2 n' \neq 0$  are *short-period perturbations*. For  $j_1 n + j_2 n' \approx 0$ , the mean motions and the terms are classified as *resonant perturbations*.

Assuming the perturbing object moves on an inner circular orbit, while the perturbed object moves outside on an eccentric orbit. The longitude of pericenter varies with time at rate  $\dot{\varpi}$ . In a frame that rotates along with the drift in longitude of the outer object, the condition for exact resonance is

$$\frac{n_{\text{in}} - \dot{\varpi}_{\text{out}}}{n_{\text{out}} - \dot{\varpi}_{\text{out}}} = \frac{p + q}{p}, \quad (2.11)$$

with  $p$  and  $q$  are small intergers. The resonant condition is then

$$\dot{\varphi} = (p + q)n_{\text{out}} - pn_{\text{in}} - q\dot{\omega}_{\text{out}} = 0, \quad (2.12)$$

where  $\varphi$  is called the *resonant argument*.

When the dynamics is studied in detail (e.g., Murray & Dermott, 2000) and the system is close to the exact resonance, the perturbations act such as to keep the resonant argument bound. In resonance the resonant argument *librates*, which means that the argument varies over time, but within a limited range. Out of resonance the argument *circulates*, taking on all values between 0 and  $2\pi$  (Armitage, 2010).

Another way is the direct numerical integration of the equation of motion. Therefore, one can use sophisticated codes based for example on the methods of Runge-Kutta, Bulirsch-Stoer, or a symplectic algorithm (Wisdom & Holman, 1991; Yoshida, 1993). A short description of the codes (DISCO, MERCURY6) we used for our simulations can be found in Sect. 2.2.4.

### 2.2.3 Photo-gravitational forces

Although in planetary systems gravity dominates the dynamics of celestial objects, other forces need to be included. Especially for small particles (below several micrometers in size) stellar radiation becomes important. One can divide the influence of the stellar radiation in two effects, the direct part, so-called radiation pressure, and a velocity dependent Poynting-Robertson effect (PR drag).

**Radiation pressure:** A particle with a cross section  $A$  in a distance  $r$  to a star with luminosity  $L_{\star}$  absorbs a radiant flux

$$L_{\text{abs}} = \frac{A Q_{\text{rp}} L_{\star}}{4\pi r^2}, \quad (2.13)$$

where  $Q_{\text{rp}}$  is the absorption efficiency of the material. Assuming that the object is a compact sphere (with  $A = \pi s^2$  and  $m = \frac{4}{3}\pi s^3 \rho_{\text{d}}$ ),  $Q_{\text{rp}}$  can be calculated with Mie theory (Bohren & Huffman, 1983). The absorbed radiation transmit momentum from the photon to the particle. This is called radiation pressure

$$\vec{F}_{\text{rp}} = \frac{L_{\text{abs}} \vec{r}}{c r} = \frac{\pi s^2 Q_{\text{rp}}(s) L_{\star} \vec{r}}{4\pi r^2 c r}, \quad (2.14)$$

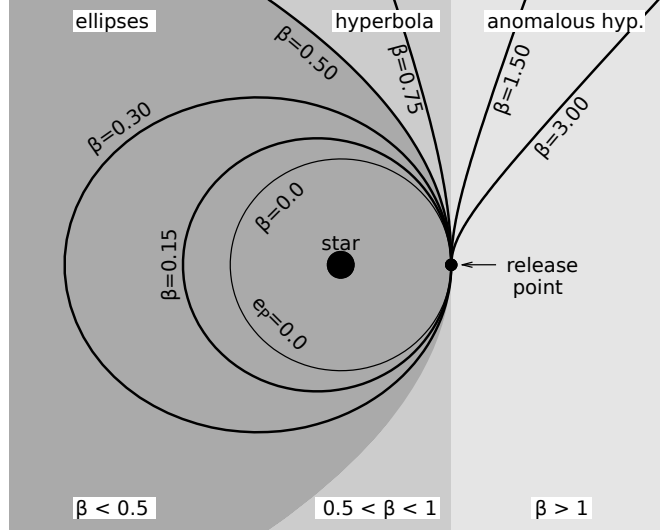


**Figure 2.3:**  $\beta$ -dependence of the orbital shape of a particle released from a parent body on circular orbit (based on Fig. 1 in Krivov et al., 2006)

where  $c$  is the speed of light. Since both forces, gravitation and radiation pressure, are proportional to  $r^{-2}$  the fraction is constant over the distance

$$\beta = \frac{|\vec{F}_{\text{rp}}|}{|\vec{F}_{\text{G}}|} = \frac{3}{16} \frac{L_{\star}}{GM_{\star}c} \frac{Q_{\text{rp}}(s)}{\pi s \rho_{\text{d}}}. \quad (2.15)$$

For particles with sizes much larger than the dominant stellar wavelength,  $Q_{\text{rp}}$  is approximately one. Thus,  $\beta$  can be approximated to be  $\propto s^{-1}$ .

The radiation pressure effectively reduces the mass of the star ( $M_{\text{eff}} \rightarrow (1 - \beta)M_{\star}$ ). That is, particles with  $\beta \geq 1$  are unbound and get ejected of the system. But also particles with  $\beta < 1$  can be blown away, which depends on their initial velocity. Let us assume that a large body ( $\beta \rightarrow 0$ ) on a Keplerian orbit releases a small fragment which is affected by radiation pressure. As a simplification the relative velocity between the large object and the fragment is assumed to be small and therefore negligible. From conservation of energy and angular momentum follows the new (primed) orbital elements for the small particle after release

$$a' = a \frac{(1 - \beta)(1 - e^2)}{1 - 2\beta(1 + e \cos(\phi)) - e^2}, \quad (2.16a)$$

$$e' = \frac{\sqrt{e^2 + 2e\beta \cos(\phi) + \beta^2}}{1 - \beta}, \quad (2.16b)$$

$$\text{and} \quad \cos(\phi') = \frac{\beta + e \cos(\phi)}{(1 - \beta)e'}. \quad (2.16c)$$

When a parent body moves on a circular orbit, the released particle obtains a new semimajor axis  $a' = a \frac{1-\beta}{1-2\beta}$  and eccentricity  $e' = \frac{\beta}{1-\beta}$ . All particles with a  $\beta > 0.5$  are released in unbound orbits and blown away by radiation pressure. For eccentric orbits of the parent body the blowout size depends obviously on the release point. Nonetheless, the blowout limit is defined as  $s_{\text{blow}} = s(\beta = 0.5)$ .

**Poynting-Robertson drag:** This effect was first mentioned by Poynting (1903) and later was formulated in terms of special relativity by Robertson (1937). Due to the aberration of light, some part of the photon's momentum acts as a "headwind" for the moving particle, accordingly the particle loses angular momentum and spirals inward to the central star. The velocity dependent drag force can be written as

$$\vec{F}_{\text{PR}} = -F_{\text{G}} \beta \left[ \frac{v_{\text{r}}}{c} \frac{\vec{r}}{r} - \frac{\vec{v}}{c} \right], \quad (2.17)$$

with  $v_{\text{r}} = \vec{v} \cdot \vec{r}/r$ . Together with the direct radiation pressure term the total force is

$$\vec{F}_{\text{rad}} = F_{\text{G}} \beta \left[ \left(1 - \frac{v_{\text{r}}}{c}\right) \frac{\vec{r}}{r} - \frac{\vec{v}}{c} \right]. \quad (2.18)$$

**Stellar wind:** Besides radiation the stellar wind needs to be taken into account. Indeed, the stellar wind is not exactly a photogravitational force, but it has the same mode of action. Momentum is transferred in radial direction and angular momentum is decreased. The resulting force due to stellar wind is analog to Eq. (2.18):

$$\vec{F}_{\text{sw}} = F_{\text{G}} \beta_{\text{sw}} \left[ \left(1 - \frac{v_{\text{r}}}{v_{\text{sw}}}\right) \frac{\vec{r}}{r} - \frac{\vec{v}}{v_{\text{sw}}} \right], \quad (2.19)$$

where  $v_{\text{sw}}$  is the speed of the stellar wind and  $\beta_{\text{sw}}$  is the ratio between the stellar wind pressure and gravitation:

$$\beta_{\text{sw}} \equiv \frac{|\vec{F}_{\text{sw}}|}{|F_{\text{G}}|} = \frac{3}{16} \frac{\dot{M}_{\star} v_{\text{sw}}^2}{GM_{\star}} \frac{Q_{\text{sw}}(s)}{\pi s \rho_{\text{d}}}. \quad (2.20)$$

$\dot{M}_{\star}$  is the mass loss rate of the star, and  $Q_{\text{sw}}(s)$  is the size dependent absorption efficiency for stellar wind particles.

The total force due to radiation and stellar wind is

$$\vec{F}_{\text{rad+sw}} = F_{\text{G}} \left[ (\beta + \beta_{\text{sw}}) \frac{\vec{r}}{r} - \frac{\beta}{c} \left(1 + \frac{\beta_{\text{sw}}}{\beta} \frac{c}{v_{\text{sw}}}\right) \left( \frac{v_{\text{r}}}{r} \vec{r} + \vec{v} \right) \right]. \quad (2.21)$$

The change of a Keplerian orbit due to the drag forces can be expressed by (Wyatt & Whipple, 1950)

$$\left(\frac{da}{dt}\right)_{\text{rad+sw}} = -\frac{\beta}{c} \left(1 + \frac{\beta_{\text{sw}}}{\beta} \frac{c}{v_{\text{sw}}}\right) \frac{GM_{\star}}{a} \frac{2 + 3e^2}{(1 - e^2)^{3/2}}, \quad (2.22)$$

$$\left(\frac{de}{dt}\right)_{\text{rad+sw}} = -\frac{5\beta}{2c} \left(1 + \frac{\beta_{\text{sw}}}{\beta} \frac{c}{v_{\text{sw}}}\right) \frac{GM_{\star}}{a^2} \frac{e}{(1 - e^2)^{1/2}}. \quad (2.23)$$

For a particle on a circular orbit the time to spiral inward from a distance  $a$  down to the star is

$$t_{\text{rad+sw}} = \frac{a^2}{4GM_{\star}} \frac{c}{\beta} \left(1 + \frac{\beta_{\text{sw}}}{\beta} \frac{c}{v_{\text{sw}}}\right)^{-1}. \quad (2.24)$$

## 2.2.4 DISCO & MERCURY6

As mentioned before in Sect. 2.2.2, the N-body problem is usually solved with numerical integration of the equation of motion. Therefore, we use our code *DISCO* (Direct Integration of Single Circumstellar Orbits), written in C/C++, which is based upon the implementation of the Bulirsch-Stoer algorithm by Press et al. (1992). Beside the gravitational restricted three-body problem the code incorporates also photogravitational forces such as radiation pressure, Poynting-Robertson-effect and stellar wind drag (see Sect. 2.2.3). As initial input one has to characterize the star through its mass  $M_{\star}$ , luminosity  $L_{\star}$ , mass-loss rate  $\dot{M}_{\star}$  and stellar wind velocity  $v_{\text{sw}}$ ; the planet through  $m_{\text{P}}, a_{\text{P}}, e_{\text{P}}$  (while  $I_{\text{P}}, \omega_{\text{P}}, \phi_{\text{P}} = 0$ ); and the test-particle with  $a, e, I, \omega, \Omega, \phi$ . The mass or size is substituted by the  $\beta$ -ratio, describing the particle's interaction with the stellar radiation and wind.

Another program is the *MERCURY6* package, provided by Chambers (1999) and written in FORTRAN 77. This “hybrid” symplectic integrator includes the advantages of the symplectic method for long periodic calculations, naming the integration speed and the conservation of energy. Since the symplectic method cannot handle close encounters accurately, it switches at close encounters to a classical numerical integration algorithm (Burlisch-Stoer). Another advantage of the *MERCURY6* package is that it handles the full N-body problem. As a caveat, the standard package does not include non-gravitational forces.

## 2.3 Collisions

As already mentioned before, collisions play an important role in the evolution of debris disks. Due to the huge amount of particles, it is not feasible to tackle the problem with N-body simulations. A more practical way is to calculate the probability and the outcome of collisions with a statistical approach from kinetic theory. Therefore, it is recommended to use the *Boltzmann* equation to calculate changes in the number-density distribution  $n$  in an appropriate phase space  $\vec{p}$ . This can be formulated with the “master equation”:

$$\frac{dn}{dt} = \underbrace{\left(\frac{\partial n}{\partial t}\right)_{\text{gain}}}_{\text{source}} - \underbrace{\left(\frac{\partial n}{\partial t}\right)_{\text{loss}}}_{\text{sink}} + \underbrace{\vec{\nabla} \cdot (n\dot{\vec{p}})}_{\text{transport}}, \quad (2.25)$$

The phase space vector  $\vec{p}$  can cover the size or mass of the object, and the orbital elements (e.g.  $\vec{p}(m, a, e, I, \Omega, \omega, \phi)$ ).

Apart from very dense systems, collisions can be assumed to be two-particle interaction. Thus, a particle of type  $\vec{p}$  can be produced by a variety of combinations of two particles  $\vec{p}_1$  and  $\vec{p}_2$ :

$$\left(\frac{\partial n}{\partial t}\right)_{\text{gain}} = \int_{\vec{p}_1} \int_{\vec{p}_2} G(\vec{p}, \vec{p}_1, \vec{p}_2) d\vec{p}_2 d\vec{p}_1. \quad (2.26)$$

The loss of particles of  $\vec{p}$  can be caused by collisions with other particles of type  $\vec{p}_1$ :

$$\left(\frac{\partial n}{\partial t}\right)_{\text{loss}} = \int_{\vec{p}_1} L(\vec{p}, \vec{p}_1) d\vec{p}_1. \quad (2.27)$$

The absolute gain- and loss-function  $G$  and  $L$ , respectively, are proportional to the individual number densities of both collisional participants:

$$G(\vec{p}, \vec{p}_1, \vec{p}_2) = G'(\vec{p}, \vec{p}_1, \vec{p}_2)n(\vec{p}_1)n(\vec{p}_2), \quad (2.28)$$

$$L(\vec{p}, \vec{p}_1, \vec{p}_2) = L'(\vec{p}, \vec{p}_1)n(\vec{p})n(\vec{p}_1). \quad (2.29)$$

While the loss function  $L'$  is only determined by the collision rate between  $\vec{p}$  and  $\vec{p}_1$ , for the gain function  $G'$  one needs to know with which probability a particular particle  $p$  is produced due to the collision between  $\vec{p}_1$  and  $\vec{p}_2$ . Thus, the gain of a particle  $\vec{p}$  can be written as product of a collision of  $\vec{p}_1$  and  $\vec{p}_2$ , and the fragment-generating

function  $f(\vec{p}, \vec{p}_1, \vec{p}_2)$

$$G'(\vec{p}, \vec{p}_1, \vec{p}_2) = L'(\vec{p}_1, \vec{p}_2) f(\vec{p}, \vec{p}_1, \vec{p}_2). \quad (2.30)$$

The generating function  $f$  can be decomposed into a function  $h(\vec{p}, \vec{p}_1, \vec{p}_2)$ , describing if the particle  $\vec{p}$  can be produced by  $\vec{p}_1$  and  $\vec{p}_2$  at all, and into a function of the size distribution of resulting fragments:

$$f = h(\vec{p}, \vec{p}_1, \vec{p}_2) g(m, \vec{p}_1, \vec{p}_2). \quad (2.31)$$

The loss function  $L'$  arise from the relative velocity  $v_{\text{rel}}$  the cross section  $\sigma$  of the two particles and the volume  $V$ , where the collisions take place:

$$L' = \frac{\sigma v_{\text{rel}}}{V}. \quad (2.32)$$

### 2.3.1 Collisional physics

An important parameter for collisions is the specific impact energy

$$Q_{\text{imp}} = \frac{E_{\text{imp}}}{(m_1 + m_2)}. \quad (2.33)$$

For a complete inelastic collision the impact energy is equal to the kinetic energy in the barycentric coordinate system:

$$Q_{\text{imp}} = \frac{1}{2} \frac{m_1 m_2}{(m_1 + m_2)^2} v_{\text{imp}}^2 \quad (2.34)$$

where  $v_{\text{imp}}$  is the impact velocity.

If the specific impact energy is larger than the critical impact energy  $Q_{\text{D}}^*$  (Durda et al., 1998), the target object is destroyed. If  $Q_{\text{imp}} < Q_{\text{D}}^*$ , the bulk stays bound or even intact, but some fragments are released, which is called *cratering*. At lower specific impact energies ( $v_{\text{imp}} \lesssim 10 \text{ m s}^{-1}$ ) *bouncing* or even *agglomeration* of two objects occurs. In debris disks both effects are negligible, since stirring due to planets in the system (Mustill & Wyatt, 2009), stellar fly-bys, or self-stirring (Kennedy & Wyatt, 2010) cause eccentricities to grow. This leads to higher impact velocities ( $\langle v_{\text{imp}} \rangle \simeq e v_{\text{Kepler}}$ ) and mostly disruptive collisions. Therefore, I will skip bouncing and agglomeration in the following treatment.

Theoretical and experimental studies show that  $Q_D^*$  depends primarily on the mass or size of the involved objects (Benz & Asphaug, 1999). While small objects are kept together mainly by cohesion (i.e., material strength), large objects are subject to self-gravitation. Therefore, the critical energy can be described by the sum of two power laws:

$$Q_D^* = A_s \left( \frac{s}{1 \text{ m}} \right)^{b_s} + A_g \left( \frac{s}{1 \text{ km}} \right)^{b_g} \quad (2.35)$$

where the indices “s” and “g” stand for strength and gravitation, respectively. The size  $s$  is a function of the total mass:  $s(m) = s(m_1 + m_2)$ .

The size distribution of the fragments as a result of a collision is usually described by a power law (Krivov et al., 2005):

$$g(m, \vec{p}_1, \vec{p}_2) = (2 - \eta) \left( \frac{m}{m_x} \right)^{-\eta} \frac{m_{\text{frag}}}{m_x^2}, \quad (2.36)$$

with  $m_{\text{frag}}$  – total mass of fragments after a collision, and  $m_x$  – mass of the largest fragment. A “classical” value is  $\eta \approx 11/6$  (Fujiwara et al., 1977). For a destructive collision the mass of fragments has to be the total mass ( $m_{\text{frag}} = m_1 + m_2$ ), and the largest mass of the fragment is

$$m_x = \frac{m_1 + m_2}{2} \left[ \frac{(m_1 + m_2)Q_D^*}{E_{\text{imp}}} \right]^c, \quad (2.37)$$

where  $c$  is a value close to unity (Paolicchi et al., 1996; Krivov et al., 2005). For cratering, the ejected mass is dependent on the impact energy

$$m_{\text{frag}} = \frac{m_1 + m_2}{2} \left[ \frac{(m_1 + m_2)Q_D^*}{E_{\text{imp}}} \right]^{-1} \quad (2.38)$$

and the mass of the largest fragment can be equated with the cumulative mass of all fragments:

$$m_x = \int_{m_x}^{\infty} m g(m, \vec{p}_1, \vec{p}_2) dm = m_{\text{frag}} \frac{(2 - \eta)}{(1 - \eta)}. \quad (2.39)$$



### 2.3.2 Collisions in debris disks

Debris disks are assumed to be in a quasi-equilibrium<sup>3</sup> between generating and destroying particles of a certain kind. If the size distribution is flatter, than it would be in a collisional equilibrium, there are more large objects and their collisional time scale is shorter. Thus, more smaller fragments are produced and large objects are destroyed. This leads to a steeper size distribution. Assuming the size distribution is steeper than in the collisional equilibrium, then there are more small particles destroying excessively their collisional partners, creating a breach at this size. Since the collisional time scale for larger particles is longer, they cannot produce enough fragments to compensate the loss, leading to a flatter size distribution.

Under the assumptions that the material properties are constant for all sizes, the size distribution has an infinite extent (or at least  $s_{\min} \ll s_{\max}$ ), that there are no transport effects, and neglecting cratering collisions, Dohnanyi (1969) found the steady-state size distribution to follow a power-law  $n(s) \propto s^{-q}$  with  $q = 3.5$ . Interestingly, in the same calculations Dohnanyi found that the size distribution of fragments after a collision has no influence on the size distribution in an infinite collisional cascade. It is only important that some fragments are produced. But for sizes where the collisional cascade ends, as around the blowout limit, where smaller particles are blown away before they can collide with large particles does the distribution of fragments comes into play. O'Brien & Greenberg (2003) extended the steady-state approximation by considering a size dependent material strength ( $Q_D^* \propto s^b$ ) and found the size distribution index to be

$$q = \frac{7 + b/3}{2 + b/3}. \quad (2.40)$$

A disk with negligible transport effects is called *collision dominated*, and the averaged lifetime of a particle, before a collision removes it, can be estimated with

$$t_{\text{col}} = \frac{1}{n(s) v_{\text{rel}} \sigma(s)}. \quad (2.41)$$

This means that the lifetime decreases when the disk becomes denser; or the particles are on more eccentric orbits and, thus, have higher relative velocities. For larger particles, and therefore larger cross-sections, the lifetime usually increases, since there are less bigger particles ( $n(s) \propto s^{-q}$  with  $q > 2$ ).

<sup>3</sup>The amounts of particles with different sizes on different orbits, while changing with time stay constant relative to each other (Löhne et al., 2008).

As already shown in Sect. 2.2.3 we can also estimate the lifetime of a particle that falls onto the star due to drag effects (Eq. 2.24). The transport lifetime is mainly proportional to the size  $s$ . Under the assumption that  $q > 3$ , there will exist a size, below which the transport lifetime becomes shorter than the collisional lifetime. For some late type stars there is no blowout size, since the radiation pressure is not strong enough and  $\beta \lesssim 0.5$ . In disks where dust particles are mainly removed by transport effects than from collisions, the size distribution flattens to a power-law index of  $q = \alpha_r - 1$ , where  $\alpha_r$  is the power-law index of the size distribution function of fragments produced in an individual collision (Wyatt et al., 2011). Such disks are called *transport dominated*.

### 2.3.3 ACE

To follow the evolution of a debris disk over time and space, the master equation (2.25) needs to be solved numerically. Therefore, our group uses the code *ACE* (Analysis of Collisional Evolution, see Krivov et al., 2005, 2006; Löhne et al., 2008), written in C++. Since the calculation with the complete phase space would be extremely time consuming, the phase space had to be simplified. The used phase space  $\vec{p}$  includes just the mass of the particle – assuming a spherical shape –, the pericenter and the eccentricity of the orbit. Nevertheless, a calculation over a time span of a gigayear normally still needs at least several days to finish.

The usage of the pericenter is equivalent to the semimajor axis and just gives some numerical advantages. To eliminate the dependence on the inclination  $I$ , the program averages over all inclinations in the range of a given opening angle. Thus, *ACE* works effectively with surface densities instead of spatial densities. Finally, the orbital angles  $\Omega, \omega$  and  $M$  are averaged, so that the disk is rotationally symmetric. A caveat is, that thus it is not possible to include perturbations from a singular source, such as resonances from a planet, into the calculations. Usually for our problems this disadvantage is not that important, since the collision rate is not significantly higher (a factor of 2) within clumps originated from resonances (Queck et al., 2007).

The initial disk parameters of *ACE* are the

- total mass of the disk,
- power-law index of the initial mass distribution  $q' = \frac{2+q}{3}$ ,
- range of semimajor axes to locate the disk,
- range of eccentricities to define the state of stirring in the disk,

- the opening angle of the disk<sup>4</sup>, and the
- slope of the radial distribution of the particles within  $[a_{\min}, a_{\max}]$ .

Beside the settings for the grid and other computational parameters, that I will not present, there are parameters for the particle properties. These contain the

- density of the dust grains ( $\rho_d$ ),
- coefficients of the material strength  $Q_D^*$  ( $A_s, b_s, A_g, b_g$ ),
- slope  $c$  for large fragment,
- slope  $\eta$  for the fragment distribution, and the
- table with the values for the  $\beta$ -ratio at given sizes, which are calculated with Mie theory (Bohren & Huffman, 1983).

## 2.4 Thermal Emission

In a full planetary system the majority of the emissions naturally stems from the star. This emission can be approximated with a black body function  $B_\lambda(T_{\text{eff}})$ , or for example modeled with photospheric *NextGen* models (Hauschildt et al., 1999). However, Aumann et al. (1984) measured around the Vega star an additional component emitting in infrared. Since spectral energy distribution (SED) shows more flux in the infrared than expected it is called *infrared excess*. This additional component was then attributed to a disk of dust.

Meanwhile hundreds of stars with infrared excess are known and scores of the dust disks have been spatially resolved. In this section the theoretical background and the programs we use are presented.

### 2.4.1 Thermal emission of a dust disk

To calculate the thermal emission of a debris disk we use several assumptions. First, the debris disk is optically thin and rotationally symmetric. Second, the particles are of spherical shape, so that Mie theory (Bohren & Huffman, 1983) can be applied.

---

<sup>4</sup>When the opening angle is chosen, one has to have in mind, that in a disk with mutual collisions and scattering, the distribution of inclinations is coupled to the distribution of eccentricities, like in a thermodynamic equilibrium. Ida (1990) found a 2:1 ratio of eccentricity to inclination:  $\langle 2I \rangle \simeq \langle e \rangle$ .

Third, they are in a thermal equilibrium:

$$\pi s^2 \frac{R_\star^2}{r^2} \int_0^\infty Q_\lambda^{\text{abs}}(s) F_\lambda(T_\star) d\lambda = 4\pi s^2 \int_0^\infty Q_\lambda^{\text{abs}}(s) B_\lambda(T_g(r)) d\lambda, \quad (2.42)$$

with  $R_\star$  – stellar radius,  $F_\lambda(T_\star)$  – flux at wavelength  $\lambda$  from a star with the effective surface temperature  $T_\star$ ,  $B_\lambda(T_g)$  – Planck function of a grain with temperature  $T_g$ , and  $Q_\lambda^{\text{abs}}(s)$  – wavelength dependent absorption cross section of a particle with size  $s$ . This allows us to calculate the relation between distance of the particle to the star  $r$  and its temperature  $T_g$ :

$$r(T_g) = \frac{R_\star}{2} \sqrt{\frac{\int_0^\infty Q_\lambda^{\text{abs}}(s) F_\lambda(T_\star) d\lambda}{\int_0^\infty Q_\lambda^{\text{abs}}(s) B_\lambda(T_g) d\lambda}}. \quad (2.43)$$

The total flux  $F_{\lambda,\text{disk}}^{\text{tot}}$  from a distance  $D$  is then:

$$F_{\lambda,\text{disk}}^{\text{tot}} = \frac{2\pi}{D^2} \int_{s_{\min}}^{s_{\max}} \int_{T_g(r_{\max})}^{T_g(r_{\min})} \Theta(r(T_g), s) Q_\lambda^{\text{abs}}(s) B_\lambda(T_g) r(T_g) \frac{dr(T_g)}{dT_g} dT_g ds, \quad (2.44)$$

where  $\Theta(r, s)$  is the surface number density (particles per unit area) of the disk at a given distance and particle size.

If the disk is spatially resolved, one can measure the surface brightness at a given distance. To compare this with a model, the surface brightness can be calculated as

$$S_\lambda(r) \approx \frac{1}{D^2} \int_{s_{\min}}^{s_{\max}} \Theta(r, s) Q_\lambda^{\text{abs}}(s) B_\lambda(T_g(r, s)) ds. \quad (2.45)$$

In general disks are not seen directly pole-on, but inclined by an angle  $\alpha$ . While pole-on means  $\alpha = 0^\circ$ , disks seen edge-on have  $\alpha = 90^\circ$ . The surface brightness in the pole-on disk frame (with capital letters)  $S_\lambda(R)$  changes to  $\tilde{S}_\lambda(r)$  in the projected sky frame (with lower-case letters). The transformation from the projected sky frame to the disk frame reads

$$\vec{R}(\vec{r}) = \begin{pmatrix} X \\ Y \end{pmatrix} = \begin{pmatrix} 1 & 0 \\ 0 & \sec \alpha \end{pmatrix} \begin{pmatrix} x \\ y \end{pmatrix}, \quad (2.46)$$

where without loss of generality, the  $x$ -direction is assumed along the major axis of

the observed disk.

Furthermore, the measured image is deformed due to diffraction, and one has to convolve the theoretical model image with an instrument-specific *Point Spread Function* (PSF):

$$S'_\lambda(\vec{r}) = \tilde{S}_\lambda(\vec{r}) \otimes \text{PSF}_\lambda(\vec{r}). \quad (2.47)$$

The convolution can be written as

$$S'_\lambda(\vec{r}) = \frac{1}{\cos \alpha} \int_0^\infty \int_0^{2\pi} S_\lambda(R(\vec{r} - \vec{r}')) \text{PSF}_\lambda(r', \phi') r' d\phi' dr'. \quad (2.48)$$

For computational purposes it is convenient to replace the explicit integration in Eq. (2.48) with Fast Fourier Transformation (FFT):

$$S'_\lambda(\vec{r}) = \mathcal{F}^{-1} \{ \mathcal{F} \{ S_\lambda(R(\vec{r})) \} \mathcal{F} \{ \text{PSF}(\vec{r}) \} \}. \quad (2.49)$$

## 2.4.2 SEDUCE & SUBITO

To calculate the spectral energy distribution of a rotationally symmetric dust disk, we used our code *SEDUCE* (SED Utility for Circumstellar Environments), written by Sebastian Müller in C++. The program needs input for the star, the dust distribution, the material properties of the dust and parameters for the integration. The star is modeled with adequate *NextGen* photosphere models (Hauschildt et al., 1999) and the stellar temperature (or alternatively stellar radius and luminosity). The dust distribution can be given as a power law ( $\Theta \propto s^q r^\xi$ ), within a distance range  $[r_{\min}, r_{\max}]$  and a size interval  $[s_{\min}, s_{\max}]$ , or as input from external calculations, such as processed DISCO data or directly from ACE. The dust properties include the bulk density (assuming spherical shapes), the optical properties, or rather absorption cross section  $Q_\lambda^{\text{abs}}(s)$ , which derived with Mie theory (Bohren & Huffman, 1983) from given refractive indices (e.g., Laor & Draine, 1993).

*SUBITO* (SURface Brightness Investigation TOol) is the program to calculate the surface brightness of a rotationally symmetric disk. The code was also written by Sebastian Müller in C++. The basic input is the same as for SEDUCE, with the addition of the distance parameter from the observer to the system, and an explicit list of requested wavelengths (e.g., 24, 70, 160  $\mu\text{m}$ ) for which the surface brightness

should be calculated. As SEDUCE, it can handle a disk modeled with power laws, or use input from external programs (DISCO and ACE). The output can be compared with deconvolved observational images, or can be convolved with a given instrumental PSF using FFT (Eq. (2.49)).

## 2.5 Masses from evolutionary models

For a directly imaged giant planet, one can measure the luminosity and – with the help of evolutionary models – estimate the mass of the object. Therefore, one has to know the cooling curve and the age of the system. The general idea for such an estimate is that the collapsing atmosphere transforms gravitational energy into radiation, and cools down with increasing age. With a measured luminosity, a given age and an evolutionary model one can obtain the appropriate mass.

To calculate the cooling curve of a planet, one has to understand the structure and radiative transfer in the atmosphere. The ingredients for such a theory include (Burrows et al., 1997):

1. Equations of state (EOS) for metallic hydrogen/helium mixtures and molecular atmospheres, (e.g., EOS by Saumon et al., 1995).
2. Chemical equilibrium codes and thermodynamic data to determine the molecular fractions.
3. Scattering and absorption opacities for the dominant chemical species, which are methane ( $\text{CH}_4$ ), water ( $\text{H}_2\text{O}$ ), nitrogen ( $\text{N}_2$ ) or ammonia ( $\text{NH}_3$ ), beside hydrogen ( $\text{H}_2$ ) and helium (He).
4. An atmosphere code to calculate temperature/pressure profiles and to identify the radiative and convective zones. Although most well-established models use 1D calculations with plane-parallel atmospheric layers to reduce the time-consuming calculations (e.g., Burrows et al., 1997; Chabrier & Baraffe, 1997; Baraffe et al., 1998, 2002, 2003), new models also incorporate 3D-calculations (e.g., Burrows et al., 2010).
5. An algorithm for converting a grid of atmospheres into boundary conditions for evolutionary calculations.
6. A Henyey code (Henyey et al., 1964; Kippenhahn & Weigert, 1990) for solving the equations of stellar evolution.
7. A radiative transfer code to produce resulting spectra.

While planets “forget” their history and their initial conditions after  $\sim 10^8$  yr, the evolutionary models show large uncertainties for young ages (first few million years), since the initial conditions are not clear. Standard models assume a large gas sphere with high internal entropy and high effective temperature. These models are called “hot-start” formation scenarios, representing formation due to disk-instabilities (Marley et al., 2007). In contrast, formation scenarios due to core-accretion are called “cold-start” models. Here, the internal entropy and effective temperature are lower. Spiegel & Burrows (2012) explain, that both, core accretion as well as disk instability, can produce similar initial conditions, so that one cannot distinguish between the formation scenarios without detailed knowledge about the physics in the accretion process.

Further challenges for atmospheric models and the calculation of evolutionary tracks are, for example, non-equilibrium chemistry, formation of (nonuniform) clouds, or realistic growth and dissolving of dust grains, which have great influence on the opacity of the atmosphere (e.g., Helling et al., 2008; Marley et al., 2010; Barman et al., 2011).

# Chapter 3

## HR 8799

*This chapter is based on the paper “A possible architecture of the planetary system HR 8799” (Reidemeister et al., 2009). I made major contributions to the dynamical stability analysis of the planets and planetesimal belts, as well as the calculation of the thermal emission of the dust. Other parts of this study were done in collaboration with Alexander Krivov, Tobias O. B. Schmidt, Simone Fiedler, Sebastian Müller, Torsten Löhne, and Ralph Neuhäuser.*

The first full planetary system presented in detail is HR 8799 (HD 218396, HIP 114189, V342 Peg, SAO 91022). The system is located  $\approx 40$  pc away from Earth, the central star is of type A5 V (van Belle & von Braun, 2009) and there have been imaged four planetary candidates<sup>5</sup> by Marois et al. (2008, 2010), confirmed by re-reducing archival data (Lafrenière et al., 2009; Fukagawa et al., 2009; Metchev et al., 2009; Soummer et al., 2011; Currie et al., 2012) and additional observations (Hinz et al., 2010; Currie et al., 2011a). Wide companions with separations within 600 AU and masses higher than  $3M_{\text{Jup}}$  can be excluded (Close & Males, 2010). As defined for a full planetary system, HR 8799 has long been known to harbor cold circumstellar dust responsible for excess emission in the far-infrared discovered by IRAS (Sadakane & Nishida, 1986; Zuckerman & Song, 2004; Rhee et al., 2007). The rather strong infrared excess has also been confirmed with ISO/ISOPHOT (Moór et al., 2006), Akari/FIS (Yamamura et al., 2010), Spitzer/MIPS (Su et al., 2009), CSO/SHARCII (Patience et al., 2011), JCMT (Williams & Andrews, 2006) and IRAM (Sylvester et al., 1996). The outer disk has been spatially resolved with Spitzer/MIPS at 24 and 70  $\mu\text{m}$ , CSO/SHARCII at 350  $\mu\text{m}$  and SMA at 880  $\mu\text{m}$  (Hughes et al., 2011). Additionally, Spitzer/IRS measurements provided evidence of warm dust emission in the mid-infrared (Jura et al., 2004; Chen et al., 2006; Su et al., 2009). Both cold and warm dust emission is indicative of one or more dust-producing planetesimal belts, similar to the Edgeworth-Kuiper belt and possibly, the asteroid belt in the Solar System. Altogether, a picture of a complex,

---

<sup>5</sup>For the sake of brevity, we will often call them “planets” throughout this chapter. However we want to caution that the often used definition of an “extrasolar planet” as a star-orbiting body of mass lower than the deuterium burning limit remains controversial. Furthermore, it is not possible at present to completely exclude the possibility that the mass of at least one companion in the HR 8799 system lies above that limit, although this appears rather unlikely.



multi-component planetary system with several planets, planetesimal belts, and dust is emerging. A prime example for a full planetary system.

Although the efforts for new observations since the discovery of the four planets have been increased, the key parameters of the system and its components remain vaguely known. A large uncertainty in the system's age amplifies the difficulty of inferring accurate masses of the companions from evolutionary models, and the mass estimates vary from one model to another even for the same age. While there are clear indications that the system is seen nearly pole-on, the exact orientation of its symmetry plane is not known either, which makes it impossible to convert projected astrometric distances of planets into their true positions.

However, already in 2009 we found it reasonable to reanalyze the available data in a comprehensive study (Reidemeister et al., 2009). While the discovery paper by Marois et al. (2008) concentrated mostly on the planets themselves and the first “follow-up” publications (Goździewski & Migaszewski, 2009; Fabrycky & Murray-Clay, 2010) provided an in-depth analysis of dynamical stability issues, we attempted with our paper to present a more synthetic view of the planetary system around HR 8799 with all its components: central star, planets, and dust-producing planetesimal belts.

This chapter presents our results published in Reidemeister et al. (2009), with additions of recent observations and conclusions. In Sect. 3.1 we briefly discuss our results on the stellar properties, notably the stellar age and inclination of the rotation axis. Section 3.2 treats the planetary system, analyzing the stability of the orbits by varying the orientation of the orbital plane and the planetary masses. Further, constraints of the masses are discussed, which were derived from evolutionary models. In Sect. 3.3 we discuss the presence of dust belts in the system and our fit to the data of the observed SED. In Sect. 3.4 it is checked whether planetesimal belts, as found to fit the infrared photometry, would be stable against planetary perturbations. Finally, Sect. 3.5 contains our conclusions and a discussion to this particular system.

## 3.1 The central star

### 3.1.1 Age

Marois et al. (2008) give an age of 30 to 160 Myr for HR 8799 and hence its companions, considering several age indicators. While most of the indicators support a rather younger age, few of them still allow for an older age or even suggest it. One indicator

is the Galactic space motion (UVW) of the primary, which is similar to that of close young associations (Marois et al., 2008). Using these data, Moór et al. (2006) propose HR 8799 to be a member of the Local Association at an age of 20 to 150 Myr with a probability of 62%. Another method is the position of HR 8799 in the Hertzsprung-Russell diagram. Taking into account the low luminosity of the star (after correction for its low metallicity) as well as its UVW space motion, Rhee et al. (2007) arrived at an age of 30 Myr. Baines et al. (2012) combined stellar radius and effective temperature values with Yonsei-Yale isochrones (Yi et al., 2001) to estimate the star’s mass and age in two scenarios:  $1.516_{-0.024}^{+0.038} M_{\odot}$  and  $33_{-13.2}^{+7}$  Myr if the star is contracting onto the zero age main sequence or  $1.513_{-0.024}^{+0.023} M_{\odot}$  and  $90_{-50}^{+381}$  Myr if it is expanding from it.

Marois et al. (2008) noted in addition that HR 8799 is a  $\lambda$  Boötis star, and these are generally thought to be young, up to a few 100 Myr. However, the Hipparcos mission has shown that the well established  $\lambda$  Boötis stars of the Galactic field comprise the whole range from the zero age main sequence to the terminal age main sequence, which is  $\sim 1$  Gyr for an A-type star (Turcotte, 2002; Paunzen et al., 2001, and references therein). The most accurate indicator of an older age is the location of HR 8799 in a  $T_{\text{eff}}$  versus  $\log g$  diagram derived from published uvby $\beta$  photometry. Using this method, Song et al. (2001) found an age of 50 to 1128 Myr with a most likely estimate of 732 Myr, and Chen et al. (2006), an age of 590 Myr.

An independent argument in favor of a younger age may come from the dust portion of the system. The measured infrared excess ratio of  $\sim 100$  at 60–90  $\mu\text{m}$  (see Fig. 3.11 below) would be typical of a debris disk star of age  $\lesssim 50$  Myr (see Su et al., 2006, their Fig. 5). However, this argument is purely statistical and must be interpreted with caution. For instance, one cannot exclude the possibility that the formation of this planetary system with four massive planets in very wide orbits could originate in an exceptionally dense and large protoplanetary disk. The latter might leave, as a by-product, a more massive debris disk at the periphery, whose fractional luminosity might well be above the statistically expected level.

Altogether, there seem to be more arguments to advocate a younger age of the system of the order of several tens of Myr. On any account, as pointed out in the discovery paper by Marois et al. (2008) and discussed in Sect. 3.2 below, extremely old ages would inevitably imply high object masses in the brown dwarf range – for all the evolutionary models used to infer the masses. Fabrycky & Murray-Clay (2010) demonstrated that dynamical stability of this system is problematic. It can be stable for masses up to 20 Jupiter masses, but only for very special orbital configurations.

### 3.1.2 Rotational period and inclination

As summarized by Sadakane (2006), the Vega-like,  $\gamma$  Doradus type pulsator HR 8799 exhibits  $\lambda$  Boötis-like abundances. He concludes that for the case of HR 8799, which is known to be a single star and associated with a dusty disk, the scenario invoking the process of selective accretion of circumstellar or interstellar material depleted in refractory elements, seems to be the most favorable explanation of the unusually low abundances.

Since HR 8799 is a  $\gamma$  Doradus type pulsator, it is difficult to determine rotational period. However, several authors measure a value of  $\sim 0.51$  d (e.g., Rodriguez & Zerbi, 1995). From a multisite campaign, Zerbi et al. (1999) found three independent periods (0.5053 d, 0.5791 d, 0.6061 d) and a coupling term between them (4.0339 d). All of these periods could be independent pulsational modes. However, if one of these pulsation periods corresponds to the rotational period of the star, we are able to calculate the inclination  $i$  of its rotational axis.

From the possible rotational periods (0.5053 d, 0.5791 d, 0.6061 d) and the radius of HR 8799 of between  $1.32R_{\odot}$  (Allende Prieto & Lambert, 1999) and  $1.6R_{\odot}$  (Pasinetti Fracassini et al., 2001), we determined the possible range of the true rotational velocity  $v$  of the star of 110–160  $\text{km s}^{-1}$ . These values agree quite well with the median value of  $v \sin i$  for A4–A6 main-sequence stars of  $159 \pm 7.2 \text{ km s}^{-1}$  (Royer et al., 2007). On the other hand, the projected rotational velocity  $v \sin i$  of HR 8799 was measured by several authors to be between 35.5  $\text{km s}^{-1}$  and 55  $\text{km s}^{-1}$  (e.g., Kaye & Strassmeier, 1998; Uesugi & Fukuda, 1982). From  $v$  and  $v \sin i$ , we finally derived a possible range of the inclination of the star of  $13^{\circ}$ – $30^{\circ}$ . We note that in the above estimates we excluded the 4.0339-day period because this would infer  $\sin i > 1$ . With a more sophisticated method, analyzing the pulsation modes, Wright et al. (2011a) derived an inclination of the stellar rotation axis to  $\gtrsim 40^{\circ}$ .

It can be expected that the rotational equator of the star and the planetary orbits are aligned with each other. Spin-orbit alignment is a common assumption, consistent for instance with the data of most transiting planets (e.g., Fabrycky & Winn, 2009). It has also been confirmed for Fomalhaut and its disk (Le Bouquin et al., 2009). Nonetheless, a misalignment on the order of several degrees is likely. It is exemplified by our own system, in which the Jupiter orbit is tilted by  $\sim 7^{\circ}$  to the solar equator and the orbital planes of giant planets differ from each other by a few degrees. With this caveat, we assumed perfect alignment throughout this work. This assumption

was needed particularly to reduce the complexity of our dynamical stability studies presented below.

## 3.2 Planets

When we analyzed the system in 2009, only the outer three of four planets have been known. Therefore, our former results are presented in this section include only three planets. Nonetheless, in some plots the fourth planet has been added to complete the picture. At the end of this section the consequences for the system are discussed, which ensue from the discovery of the fourth planet, and the current state of research is presented.

### 3.2.1 Masses from models

A common way of estimating the masses of various astrophysical objects, from stars to planets, is to use their formation and evolution models. These models predict important physical parameters of objects of various masses, notably their luminosity and temperature, as a function of age. If the age is known, a comparison with luminosity or temperature retrieved from observations allows one to estimate the mass. At the time of our study the temperature of the companions was unknown, but their luminosity was derived from brightness and distance with sufficient accuracy to apply the models. Ages, masses, and other parameters of other directly imaged planet candidates were reviewed by Schmidt et al. (2009).

However, all models involve simplifying assumptions and adopt certain initial conditions, e.g., the initial internal energy and temperature structure. Further, the so-called hot-start models all start at a non-zero age (e.g., 0.1 or 1 Myr) with a finite luminosity and thus do not consider the actual formation stage. For these reasons, models may not deliver reliable results for at least the first several megayears (see Wuchterl, 2001; Chabrier et al., 2005, for discussion), if not several hundred megayears (Stevenson, 1982).

Using the model by Baraffe et al. (2003) and assuming the age range of 30–160 Myr, Marois et al. (2008) estimated the masses of companions to be  $7_{-2}^{+4}M_{\text{Jup}}$  for HR 8799 b and  $10_{-3}^{+3}M_{\text{Jup}}$  for HR 8799 c & d. For the later discovered planet HR 8799 e Marois et al. (2010) estimated a mass of  $7_{-2}^{+3}M_{\text{Jup}}$  for an age of 30 Myr and  $10_{-3}^{+3}M_{\text{Jup}}$  for 60 Myr. We recalculated the possible masses of the three outer companions with the

**Table 3.1:** Masses of HR 8799 b / c / d from luminosity (and absolute K-band magnitude) using various evolutionary models.

HR 8799 b		Luminosity $\log L/L_{\odot} = -5.1 \pm 0.1$ (Marois et al., 2008)									
Model		Mass [ $M_{\text{Jup}}$ ] at age									
		20 Myr	30 Myr	60 Myr	100 Myr	160 Myr	590 Myr	730 Myr	1000 Myr	1128 Myr	
Burrows et al. (1997)		3.5–4.5	4.5–6	7–8.5	9–11	11.5–12.5	22–26	25–30	28–33	30–36	
Marley et al. (2007) <sup>a</sup>		3–5	4–7	6–10							
Chabrier et al. (2000)							21–26			30–35	
Baraffe et al. (2003)			4–5	6–7	9–10		21–26			30–35	
Baraffe et al. (2008) <sup>b</sup>				$\sim 7$	$\sim 9$						
Baraffe et al. (2003) <sup>c</sup>			$\sim 5.5$	$\sim 8.5$	$\sim 10.5$		$\sim 30$			$\sim 38$	
HR 8799 c / d		Luminosity $\log L/L_{\odot} = -4.7 \pm 0.1$ (Marois et al., 2008)									
Model		Mass [ $M_{\text{Jup}}$ ] at age									
		20 Myr	30 Myr	60 Myr	100 Myr	160 Myr	590 Myr	730 Myr	1000 Myr	1128 Myr	
Burrows et al. (1997)		6–7.5	7.5–9.5	11–12	12.5–13	13–13.5	30–38	35–43	40–48	41–50	
Marley et al. (2007) <sup>a</sup>		6–8	8–10								
Chabrier et al. (2000)			6–7	8–10	10–11		28–34			39–46	
Baraffe et al. (2003)			6–7	8–10	10–11		27–31			37–43	
Baraffe et al. (2008) <sup>b</sup>				$\sim 9$							
Baraffe et al. (2003) <sup>d</sup>			$\sim 7.5$	$\sim 10.5$	$\sim 11.5$		$\sim 38$			$\sim 48$	

Remarks: All mass values were shortened to appropriate decimals and partly rounded to halves or integers of a Jupiter mass. (a) Hot-start models. (b) Non irradiated models. (c) Using  $M_{K_s} = 14.05 \pm 0.08$  mag (Marois et al., 2008). (d) Using  $M_{K_s} \sim 13.12$  mag instead of slightly different values  $M_{K_s} = 13.13 \pm 0.08$  mag for HR 8799 c and  $M_{K_s} = 13.11 \pm 0.12$  mag for HR 8799 d, given in Marois et al. (2008).

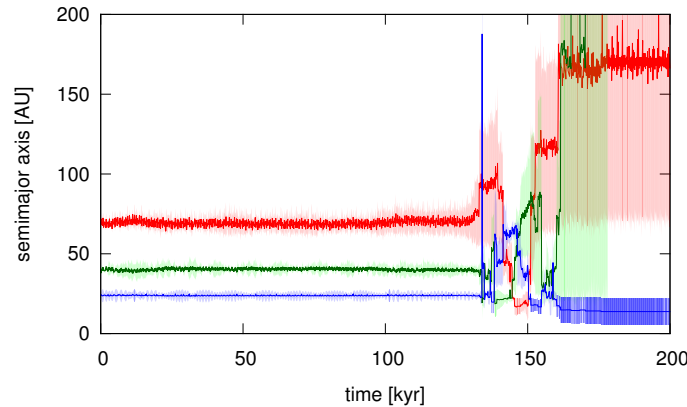


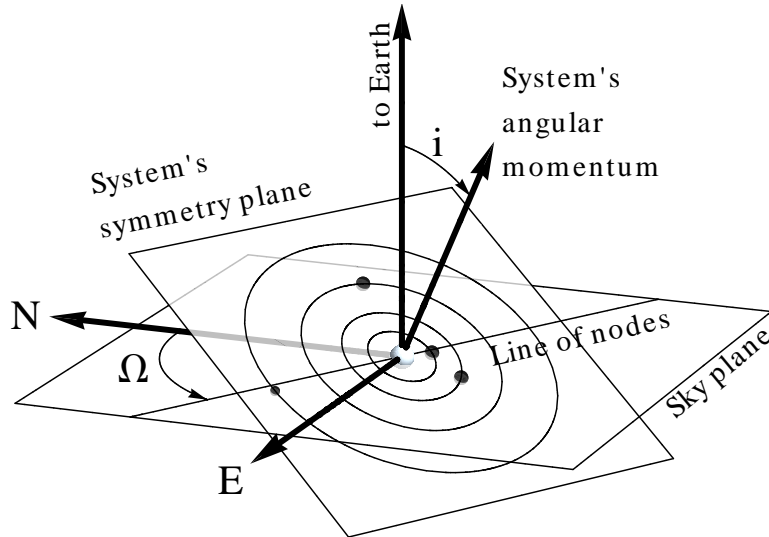
**Figure 3.1:** Instability of the planetary system with nominal masses in the non-inclined case. For each of the planets, the solid inner line corresponds to the semi-major axes, while the colored area depicts the pericentric and apocentric distance.

aid of several state-of-the-art hot-start evolutionary models from system’s age and companions’ luminosity. As discussed in Sect. 3.1.1, we allowed a broader range of possible ages. Table 3.1 shows our results. We note that some models consider only limited age and/or mass ranges; for instance, the model by Marley et al. (2007) does not consider masses higher than  $10M_{\text{Jup}}$ . This explains why some positions in the table are not filled. In general, the mass estimates that we obtain are similar to those of Marois et al. (2008).

### 3.2.2 Masses from stability requirement

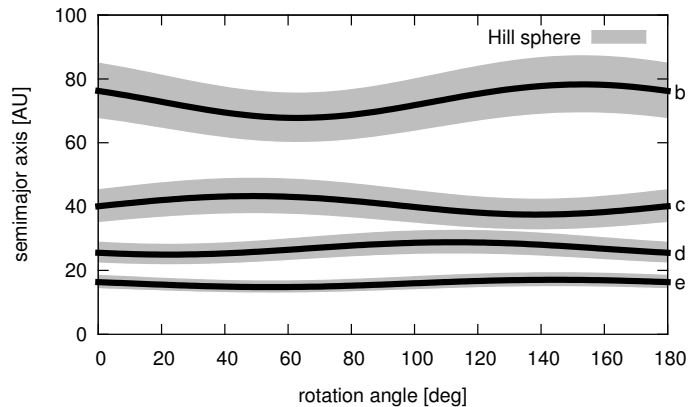
The simplest possible assumption that one can make is that the system is seen perfectly face-on (inclination  $i = 0$ ) and that all planets are initially in circular, coplanar orbits. However, as Fabrycky & Murray-Clay (2010) pointed out, such a system with the masses reported in Marois et al. (2008) would be unstable. This is readily confirmed by our numerical integrations that are described below. Figure 3.1 shows the time evolution in the planetary orbits. After 134 kyr, a close encounter between HR 8799 c and d already occurs and triggers instability of all three planets ending with the ejection of HR 8799 c 50 kyr later. These time scales are fully consistent with those reported by Fabrycky & Murray-Clay (2010).

The studies by Fabrycky & Murray-Clay (2010) and Goździewski & Migaszewski (2009) were based largely on fitting simultaneously the observed positions and differential proper motion of the companions and checking the stability of the resulting systems in the course of their dynamical evolution. Since constraints on eccentricities



**Figure 3.2:** Orientation of the system with respect to the line of sight.

from the differential proper motion are weak, but clear indications exist for inclined orbits from the rotational period analysis (see Sect. 3.1.2), we employed a different method. We confined our simulations to initially circular and coplanar orbits (and allow the eccentricities to evolve to non-zero values at later times), but allow the symmetry plane to have all conceivable non-zero inclinations and an arbitrary orientation. Thus, in the subsequent analysis we introduce two angles (Fig. 3.2). One is the inclination  $i$  itself, measured between the angular momentum vector and a vector pointing toward the observer. Another angle is the longitude of node  $\Omega$  of the system's symmetry plane on the plane of the sky, which is measured from north in the eastern direction. We vary the inclination  $i$  from  $0^\circ$  to  $45^\circ$ , thus extending the range suggested by Sect. 3.1.2 to higher values. This may be useful to accommodate a possible tilt of planetary orbits with respect to the stellar equator. The rotation angle  $\Omega$  is unconstrained by the observations. It is sufficient to vary it from  $0^\circ$  to  $180^\circ$ , since the true mutual positions of all three planets at  $(i, \Omega)$  and  $(i, \Omega + 180^\circ)$  would be exactly the same. For each  $(i, \Omega)$ -pair, we can convert the observed (projected) instantaneous positions (astrometric distances and positional angles) of the three planets into their true positions in space. Therefore, we used the planetary coordinates given in Marois et al. (2008) from August 12, 2008. If, furthermore, initially circular orbits are assumed, the calculated distances of planets will coincide with their initial semimajor axes. We thus consider a two-parametric  $(i, \Omega)$  set of possible systems; for each of them, the initial orbital configuration is fully and uniquely defined.



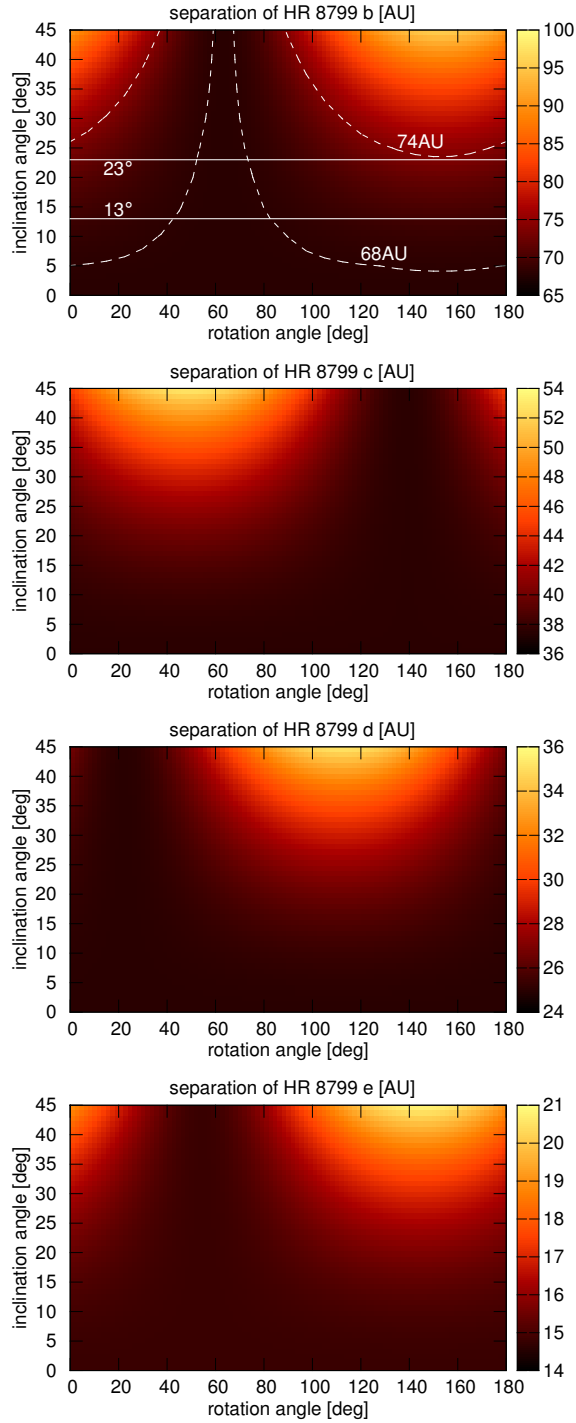
**Figure 3.3:** Semimajor axes of HR 8799b, c, d, and e (solid lines) and the extension of their Hill spheres (gray shade) for nominal masses and  $i = 30^\circ$  as a function of  $\Omega$ .

Figure 3.3 shows the initial astrometric semimajor axes of the three planets with an inclination of  $i = 30^\circ$  as a function of rotation angle  $\Omega$ , as well as the corresponding Hill spheres for nominal planetary masses. Similarly, Fig. 3.4 depicts the initial semimajor axis of the planets depending on  $i$  and  $\Omega$ . Finally, Fig. 3.5 plots the difference of initial semimajor axes of HR 8799 b and c, HR 8799 c and d, as well as HR 8799 d and e, again depending on  $i$  and  $\Omega$ . From all of these figures, it is clearly seen that the orbital spacing, and therefore the stability, might indeed strongly depend on the orientation of the system.

We note, that the analysis of HR 8799 b by Lafrenière et al. (2009), which is based on archival HST/NICMOS data from 1998, yielded a semimajor axis of  $a \sim 68\text{--}74$  AU and an inclination of  $i \sim 13^\circ\text{--}23^\circ$ . This result was confirmed by an improved analysis of the HST-data by Soummer et al. (2011), also providing astrometric positions of HR 8799 c & d.

This expectation is fully confirmed by the main bulk of numerical integrations that we performed with the aid of the MERCURY6 package (Chambers, 1999). We used the hybrid symplectic integrator with an adaptive step size and a  $10^{-14}$  angular momentum conservation accuracy, which changes to a Bulirsch-Stoer algorithm at distances of less than 3 Hill radii. Output was stored every 1000 yr. Each integration terminated when two planets had a distance less than half the Hill radius or after an integration time of  $t_{\max} = 100$  Myr. In all cases, we assumed a stellar mass of  $1.5M_\odot$  and a distance of 39.4 pc to convert the separation angle into the projected astrometric distance. The three planets started at positions at the epoch of 2008 Sept. 18 (see Table 1 in Marois et al., 2008). We used 3 different sets of possible planet masses (see Table 3.2) and checked stability for  $i \in \{0, 1, \dots, 45^\circ\}$  and  $\Omega \in \{0, 5, \dots, 180^\circ\}$ . We note that,





**Figure 3.4:** Initial semimajor axes of all four planets as a function of  $i$  and  $\Omega$ . Solid horizontal lines in the uppermost panel border the range of inclination range of  $i = 13\text{--}23^\circ$  for HR 8799 b, reported by Lafrenière et al. (2009). Dashed lines do the same for the semi-major axis range,  $a = 68\text{--}74$  AU.

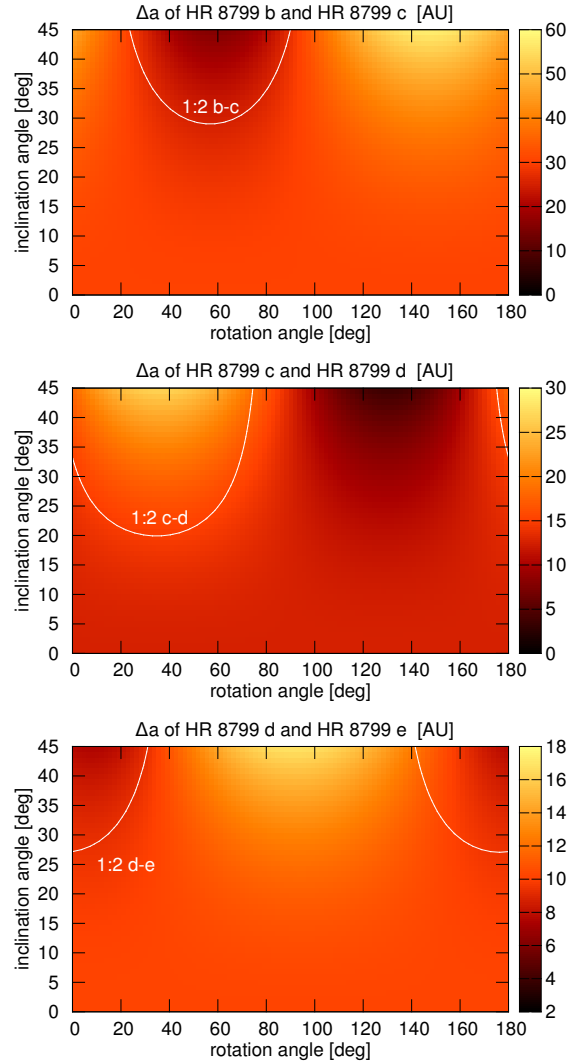


**Figure 3.5:** Difference of initial semimajor axes  $\Delta a$  between HR 8799 b & c (*top*), HR 8799 c & d (*middle*), and HR 8799 d & e (*bottom*) as a function of  $i$  and  $\Omega$ , as well as the location of the 1:2 commensurability of the periods for circular orbits.

**Table 3.2:** Three sets of planet masses used in numerical integrations

HR 8799	b	c	d
low mass	$5M_{\text{Jup}}$	$7M_{\text{Jup}}$	$7M_{\text{Jup}}$
nominal mass	$7M_{\text{Jup}}$	$10M_{\text{Jup}}$	$10M_{\text{Jup}}$
high mass	$11M_{\text{Jup}}$	$13M_{\text{Jup}}$	$13M_{\text{Jup}}$

although we assumed initially circular orbits, this does not mean that the orbits stay circular at later times. Indeed, the opposite is true: the mutual perturbations always force eccentricities to acquire values in the range between zero and approximately 0.1, so that the initial circularity is “forgotten” by the system.

The results of these integrations are presented in Fig. 3.6, which depicts the time interval until the first close encounter – as a proxy for stability – with an upper limit of 100 Myr. It can be seen that all three planets may be stable for 100 Myr for either set of planetary masses, but only for some of all possible orientations. Specifically, an inclination of  $\gtrsim 20^\circ$  is required and the rotation angle  $\Omega$  must lie within the range of between  $\approx 0^\circ$  and  $\approx 50^\circ$ . The higher the mass, the narrower the “stability spot” in the  $(i, \Omega)$ -plane. Furthermore, we conclude that it is the inner pair (c and d) that tends to destroy the stability. Comparing Fig. 3.6 to Fig. 3.5, one can indeed see that the most stable regions are those where  $\Delta a$  of HR 8799 c and d reaches the largest value, whereas that of HR 8799 b and c does not. Finally, a comparison of Fig. 3.6 and Fig. 3.4 shows that the position of the “stability spot” in Fig. 3.6 roughly matches the inclination of  $i = 13\text{--}23^\circ$  and the semimajor axis of  $a = 68\text{--}74$  AU of the outermost planet reported by Lafrenière et al. (2009).

We also check, whether all considered geometries are consistent with the measured differential proper motion of the companions. Figure 3.7 depicts the projected differential proper motions  $\mu$  that the planets in circular orbits would have for each pair of  $i$  and  $\Omega$ . Overplotted are the values of  $\mu$  actually measured together with their  $1\sigma$  and  $2\sigma$  deviations. We derived the differential proper motion of  $22 \pm 2$  mas yr $^{-1}$ ,  $30 \pm 2$  mas yr $^{-1}$ , and  $34 \pm 3$  mas yr $^{-1}$  for HR 8799 b, c, and d, respectively, by combining measurements from Currie et al. (2011a) with the 1998 data from Soummer et al. (2011)<sup>6</sup>. For comparison, the differential proper motion of HR 8799 b given in Marois et al. (2008) is  $25 \pm 2$  mas yr $^{-1}$ . In the non-inclined case, the calculated differential proper motions for HR 8799 b and c are always within  $1\sigma$  of the measured value. All of their orbits with an inclination  $\lesssim 30^\circ$  lie within  $1\sigma$  of the measured value. The best

<sup>6</sup>For HR 8799 e we used two epochs, given in Marois et al. (2010, 2009-08-01 and 2010-09-30), and derived a differential proper motion of  $45 \pm 13$  mas yr $^{-1}$ .

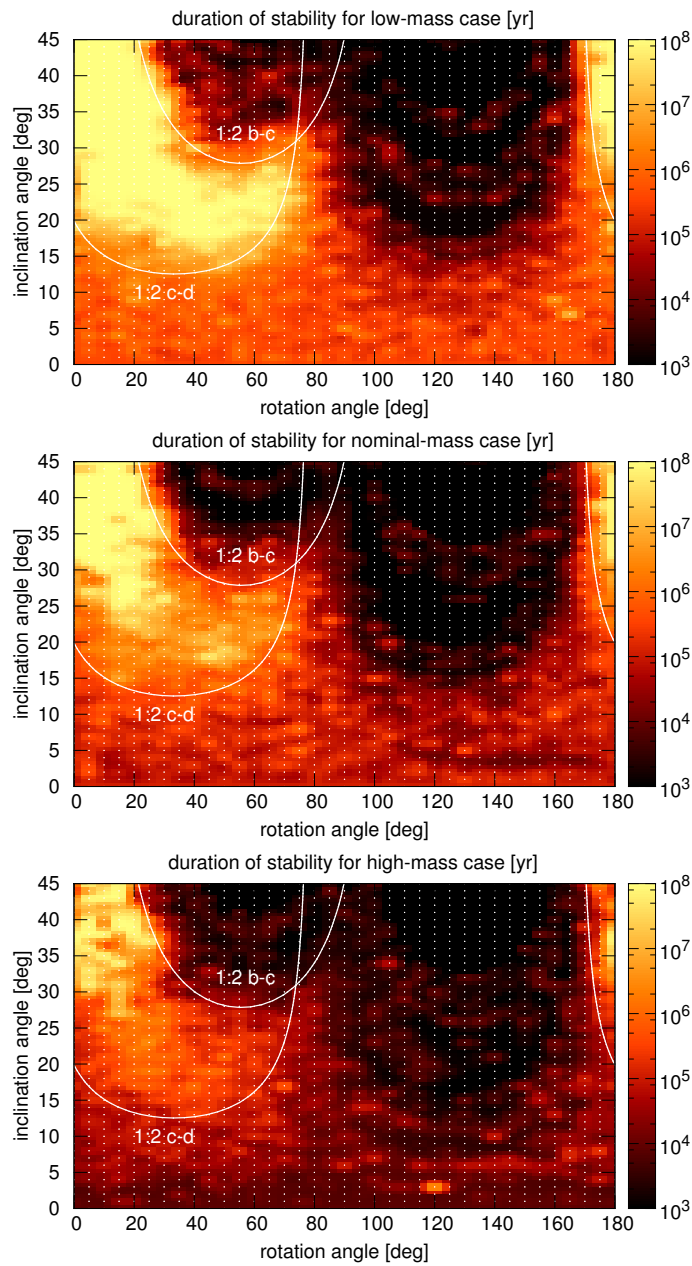


**Figure 3.6:** Duration of stability depending on  $i$  and  $\Omega$  for different sets of planetary masses given in Tab. 3.2: *top*: low, *middle*: nominal, *bottom*: high. A grid of dots corresponds to the actual set of numerical runs (one dot = one run). Curves show where the periods between b-c and c-d would have a commensurability of 1:2 if the orbits were exactly circular.

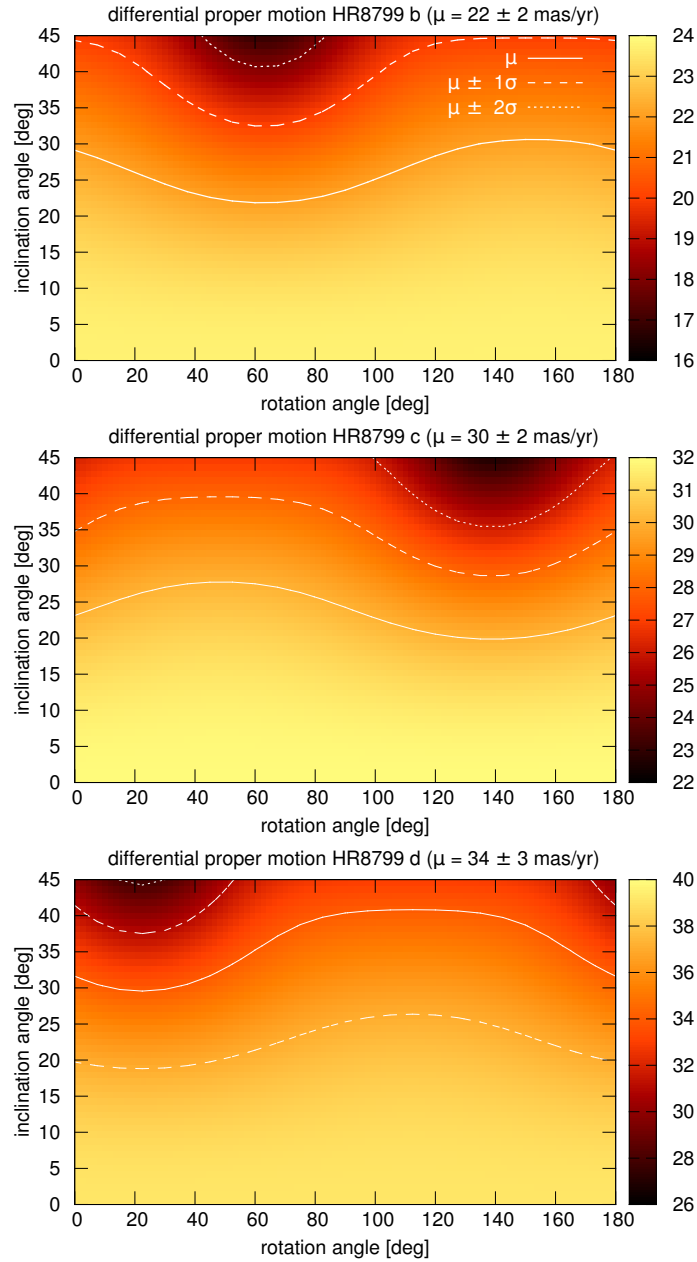


**Figure 3.7:** Sky-projected differential proper motion that HR 8799 b (*top*), c (*middle*) and d (*bottom*) would have for each pair of  $i$  and  $\Omega$  (assuming circular orbits). The isolines are at  $\mu$ ,  $\mu \pm \sigma$ , and  $\mu \pm 2\sigma$ , where  $\mu$  is the differential proper motion derived from the measurements, as described in the text. A panel for HR 8799 e is not included, since the uncertainty ( $\mu = 45 \pm 13 \text{ mas yr}^{-1}$ ) is too large for a reasonable interpretation.

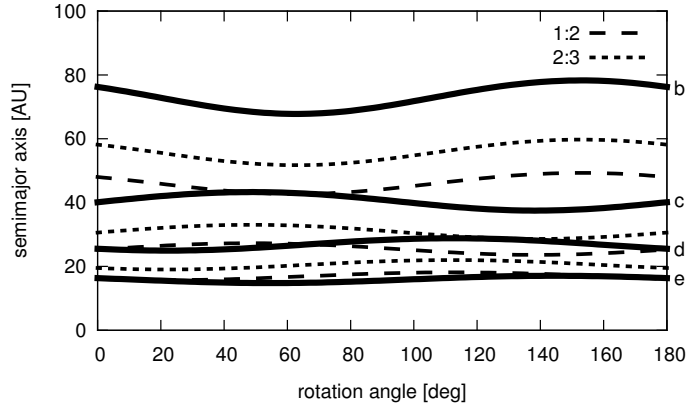


**Figure 3.8:** Semimajor axes of HR 8799 b, c, d and e (solid lines), and positions of 1:2 (dashed) and 2:3 (dotted) nominal mean-motion resonances of the three outer planets for  $i = 30^\circ$  as a function of  $\Omega$ .

constraints are obtained for HR 8799 d, where  $\mu \pm 1\sigma$  is found between inclinations  $25^\circ \lesssim i \lesssim 35^\circ$ . For all planets it holds true, that nearly the entire parameter range of  $(i, \Omega)$  explored here is compatible with observations to within  $2\sigma$ . It is easy to show that taking into account the true low eccentricities up to  $\approx 0.1$  acquired by the planets would not change this conclusion.

To understand the stability region shown in Fig. 3.6, we check the possibility that it may be related to resonances. From Fig. 3.8, it is obvious that HR 8799 c and d (as well as e) are close to the 1:2 resonance. For coplanar and circular orbits, we searched for combinations of  $i, \Omega$  that would correspond to the 1:2 commensurability. The resulting loci of the nominal 1:2 resonance in the  $(i, \Omega)$ -plane (Fig. 3.6) encircle the stability region. This strengthens the hypothesis that the stability may be directly related to the 1:2 resonance.

We then checked whether or not the orbits of HR 8799 c and d within the stability region are indeed locked into the resonance. To this end, we calculated the resonant argument  $\varphi_{cd} = 2\lambda_c - \lambda_d - \omega_d$ , where  $\lambda_c$  and  $\lambda_d$  are the mean longitudes of HR 8799 c and d and  $\omega_d$  is the argument of pericenter of the latter planet. We found that *all* stable orbits are indeed resonant. Interestingly, the initial values of  $\lambda_c$  and  $\lambda_d$  adopted in all numerical runs were such that the planets are not locked in the resonance initially, but – in all stable cases – the system swiftly “slips” into the resonance, becoming stable. The resonant argument  $\varphi_{cd}$  librates around  $0^\circ$  with an amplitude (which we calculated as a standard deviation) of  $22^\circ$ – $100^\circ$ . For comparison, the non-resonant case would have a standard deviation of  $\sim 103.9^\circ$ . However, we ensure that even the

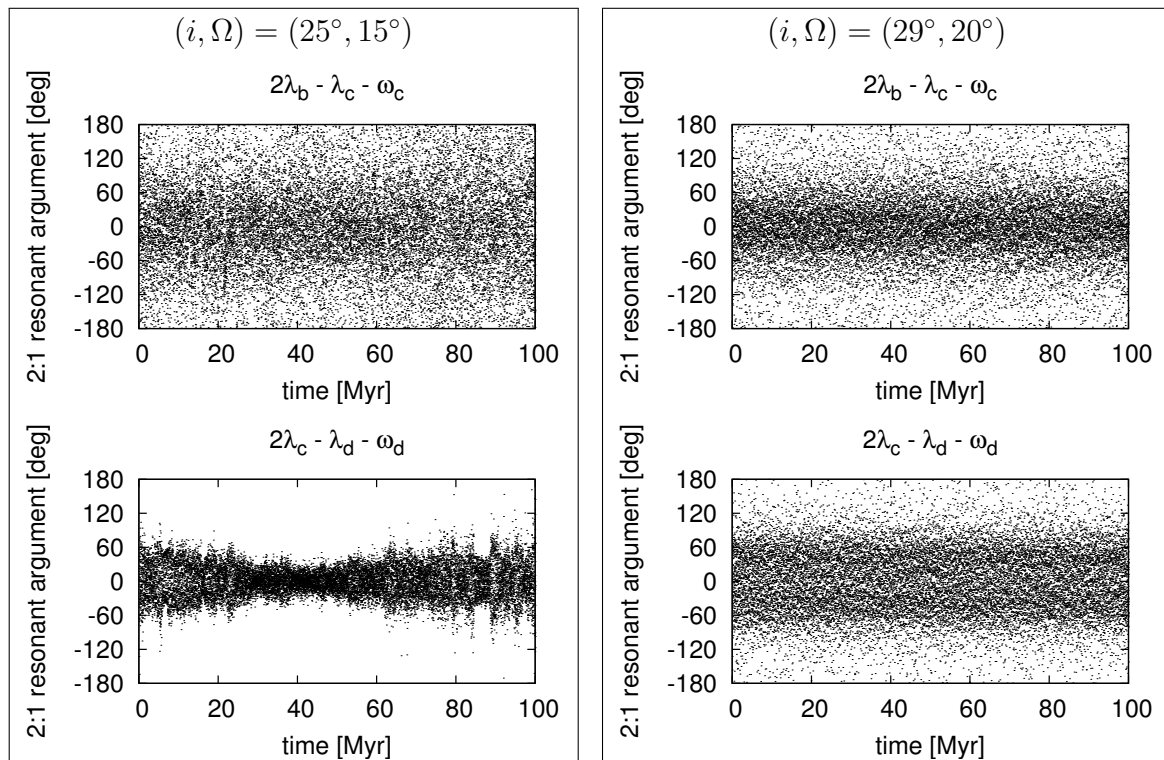


**Figure 3.9:** Typical behavior of resonant arguments for the 1:2 mean-motion resonance between HR 8799 b & c (*top*) and HR 8799 c & d (*bottom*). Nominal planetary masses are assumed. The libration amplitude is  $86^\circ$  (*left top*),  $36^\circ$  (*left bottom*),  $63^\circ$  (*right top*), and  $60^\circ$  (*right bottom*).

cases where the libration amplitude is as high as  $100^\circ$  are resonances, albeit shallow. In these cases, the resonant argument circulates rather than librates. Thus, the phase trajectories on the  $e_c \cos \varphi_{cd} - e_c \sin \varphi_{cd}$  plane are circles with an offset from  $(0,0)$ , which is indicative of a resonant locking.

For all stable configurations we then calculated the resonant argument for the two outer planets, HR 8799 b and c, defined as  $\varphi_{bc} = 2\lambda_b - \lambda_c - \omega_c$ . We found that they are in a 1:2 resonance, too, with the standard deviation in the range  $36^\circ$ – $97^\circ$ . We note that in all stable cases at least one of the resonances, b-c or c-d, is strong, as suggested by a low libration amplitude. Two typical examples of the time evolution of the resonant argument for both planetary pairs are shown in Fig. 3.9. Thus, our results are consistent with those by Fabrycky & Murray-Clay (2010) and Goździewski & Migaszewski (2009), who suggested a double resonance 1:2:4 as the likely “survival recipe” for the entire three-planet system.

Allowing initially eccentric orbits would not help, since the semimajor axes would also need to be varied (and the arguments of pericenter as well). Thus the parameter

space would be exploding, figuratively. Therefore the method to constrain stability needs to be changed, for example by incorporating astrometric data, as Goździewski & Migaszewski (2009) or Fabrycky & Murray-Clay (2010) did. Another possibility to reduce the amount of variables is to confine the parameter space to resonant configurations (i.e., assuming that the system is indeed in resonance). But since the theory of mean-motion resonances are just for one perturbing object and a perturbed one, and not for four mutually disturbing objects, this attempt was not successful. Finally, with the observations done so far (or at least with those available one or two years ago) we can not pose better constraints on the orbits or masses of the planets.

As noted above, the major danger of system destabilization comes from the two inner planets (HR 8799 c and d), which are probably more massive and tightly spaced. Keeping this in mind and taking into account that data on the innermost companion (e.g., its differential proper motion) are as yet the least reliable, we checked the dynamical stability properties the system would have without HR 8799 d. We used the same setup for MERCURY6 and restricted our analysis to three cases: non-inclined configuration,  $i = 15^\circ$ , and  $i = 30^\circ$ . The overall result is that, as expected, the absence of the inner companion would drastically improve stability:

- *The non-inclined configuration* becomes stable over a period of 100 Myr – not only for the nominal masses, but also for much higher masses up to  $m_b = 22M_{\text{Jup}}$  and  $m_c = 30M_{\text{Jup}}$ . The rapid breakdown of the system in less than 10 kyr would only be guaranteed with masses as high as  $m_b = 33M_{\text{Jup}}$  and  $m_c = 45M_{\text{Jup}}$ .
- *For  $i = 15^\circ$*  and all  $\Omega = 0^\circ\text{--}180^\circ$ , the system with nominal masses is always stable over 100 Myr.
- *For  $i = 30^\circ$* , the system with nominal masses is unstable for  $\Omega = 40^\circ\text{--}75^\circ$ , and otherwise stable.

### The fourth planet

The discovery of the fourth planet at a projected distance of 14 AU a year after our analysis exacerbated the dynamical situation. Renewed calculations with the fourth planet, using positions for all four planets given in Currie et al. (2011a, 2009-10-08) and masses with 7 (low) and  $10M_{\text{Jup}}$  (nominal) for HR 8799 e, showed that no configuration lasts longer than a few ten million years. Sudol & Haghighipour (2012) also conclude that the planets have to have lower masses and the system is younger.

As in the simulations with only three planets before, the long lasting configurations are

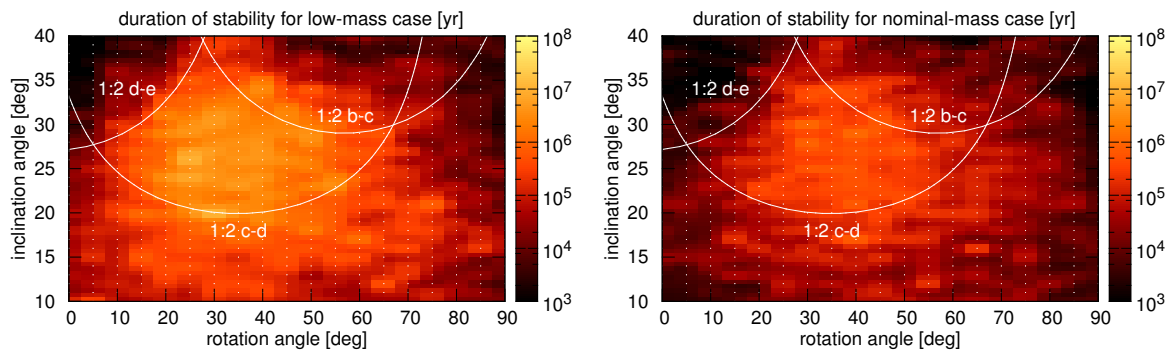


**Figure 3.10:** Duration of stability with all four planets depending on  $i$  and  $\Omega$  for different sets of planetary masses given in Tab. 3.2: *left*: low, and *right*: nominal. A grid of dots corresponds to the actual set of numerical runs (one dot = one run). Curves show where the periods between b-c, c-d and d-e would have a commensurability of 1:2 if the orbits were exactly circular.

found to be encircled by 1:2 mean-motion resonances between b-c, c-d and d-e. Thus, a resonant configuration with a multiple 1:2 MMR can be expected for the system. A resonant configuration can also provide more stability, even for high planetary masses (Fabrycky & Murray-Clay, 2010).

## 3.3 Dust and the planetesimal belts

### 3.3.1 Observations

Table 3.3 lists the catalogs and references used to provide the optical, infrared, sub-mm, and millimeter photometry. We employed the Hipparcos and Tycho databases as well as USNO and GSC catalogs to compile the optical photometry, whereas the near-infrared data were taken from the 2MASS survey. The mid- and far-infrared photometry is provided by the IRAS, ISO, Spitzer and AKARI satellites, while sub-mm and millimeter data were obtained at CSO, JCMT and IRAM. For transforming the  $B$ ,  $V$ ,  $R$ ,  $I$  magnitudes into units of flux [Jy], we used the standard calibration system of Johnson, whereas for the 2MASS  $J$ ,  $H$ ,  $K_s$  bands the calibrations of Cohen et al. (2003) were applied. For the IRAS fluxes, color-correction factors (Beichman et al., 1988) assuming a black body spectral energy distribution for temperatures of 5 000 K, 150 K, 50 K and 50 K were employed<sup>7</sup> for data points at wavelengths of 12, 25, 60 and 100  $\mu\text{m}$ , respectively (as done by Su et al. (2009) in these wavelength ranges).

<sup>7</sup>Correction factors are only available over a coarse temperature grid . . . , 5 000 K, 10 000 K.



The AKARI measurements also have been corrected by factors assuming black body SEDs for temperatures of 7 000 K, 150 K and 50 K for 9, 18 and 90  $\mu\text{m}$ , respectively (Lorente et al., 2007; Verdugo et al., 2007).

The optical and near-infrared photometry was used to derive a best-fit photospheric model. We performed a minimum  $\chi^2$  fitting of the stellar photospheric fluxes by NextGen model atmospheres (Hauschildt et al., 1999), only to data for bandpasses of wavelengths shorter than 3  $\mu\text{m}$ , where no excess emission is expected. In our search for the best-fit model, we employed a system of NextGen models with an effective temperature step size of 200 K, with a  $\log g$  of 4.5, and with solar metallicity<sup>8</sup>. Varying the temperature as well as the stellar radius, which affects the solid angle dilution factor, we derive a best-fit temperature of 7 400 K and a best-fit radius of  $1.34R_{\odot}$ , both in a very good agreement with the results of Gray & Kaye (1999).

To obtain more information about the dust component of the system, we used the Spitzer/IRS data published by Su et al. (2009). This spectrum is 4–60 times deeper than the spectrum measured by Chen et al. (2006). In the dataset, we got from Kate Su, the individual IRS modules and orders are already joined, and smoothed by resolution  $R = 100$  with signal-to-noise rejection of 3. Finally, we subtracted a black-body with a temperature of 7400 K, which is just a rough approximation of the stellar photosphere. The resulting excess emission is quite sensitive around 10  $\mu\text{m}$ , since the uncertainty is in the same order of magnitude as the excess. For wavelengths  $\gtrsim 20 \mu\text{m}$  the excess becomes much larger and the approximation is reliable. The resulting set of photometry points and the IRS spectrum are shown in Fig. 3.11 (with photosphere) and in Fig. 3.12 (excess emission only).

### 3.3.2 Interpretation

To derive an approximate idea of the location of the dust belt(s) and the amount of dust in the HR 8799 system, we modeled the SED assuming a double power-law surface number density of dust  $\Theta \propto s^{-q}r^{-\xi}$ , where  $s$  and  $r$  are the dust grain size and distance from the star, respectively. Keeping in mind that SED interpretation is a degenerate problem and to decrease the number of free parameters, we restrict ourselves to the case of  $q = 3.6$  and  $\xi = 1$ . The dust composition was assumed to be astronomical silicate (Laor & Draine, 1993; Draine, 2003). As the minimum grain size, we chose a multiple of the radiation pressure blowout radius, which equals  $s_{\text{blow}} \approx 1 \mu\text{m}$ . The

<sup>8</sup>Although the metallicity of HR 8799 is  $-0.47$  (Gray & Kaye, 1999), this parameter has no important effect on the fitting result.

**Table 3.3:** Photometry of HR 8799. IRAS and AKARI fluxes are color corrected as described in the “IRAS Explanatory Supplement” (Beichman et al., 1988) and “AKARI IRC/FIS Data User Manuals” (Lorente et al., 2007; Verdugo et al., 2007), respectively.

Photometric band	Flux or magnitude [mag]	$F_{\text{qual}}$ (IRAS)	Ref.
<i>B</i>	$6.090 \pm 0.300$		(1)
<i>B</i>	6.196		(2)
<i>B</i>	$6.210 \pm 0.010$		(3)
<i>B</i>	$6.214 \pm 0.009$		(4)
<i>V</i>	$5.960 \pm 0.010$		(4)
<i>V</i>	5.959		(2)
<i>V</i>	$5.960 \pm 0.010$		(3)
<i>R</i>	$5.810 \pm 0.300$		(1)
<i>I</i>	$5.690 \pm 0.300$		(1)
<i>J</i>	$5.383 \pm 0.027$		(5)
<i>H</i>	$5.280 \pm 0.018$		(5)
<i>K<sub>s</sub></i>	$5.240 \pm 0.018$		(5)
	[Jy]		
IRAS PSC 12 $\mu\text{m}$	$0.267 \pm 0.025$	3	(6)
IRAS PSC 25 $\mu\text{m}$	< 0.362	1	(6)
IRAS PSC 60 $\mu\text{m}$	$0.445 \pm 0.070$	2	(6)
IRAS PSC 100 $\mu\text{m}$	< 2.619	1	(6)
IRAS FSC 12 $\mu\text{m}$	$0.278 \pm 0.026$	3	(7)
IRAS FSC 25 $\mu\text{m}$	< 0.255	1	(7)
IRAS FSC 60 $\mu\text{m}$	$0.450 \pm 0.071$	3	(7)
IRAS FSC 100 $\mu\text{m}$	< 3.524	1	(7)
ISO 60 $\mu\text{m}$	$0.412 \pm 0.021$		(8)
ISO 90 $\mu\text{m}$	$0.585 \pm 0.041$		(8)
Spitzer MIPS 24 $\mu\text{m}$	$0.087 \pm 0.002$		(9)
Spitzer MIPS 70 $\mu\text{m}$	$0.610 \pm 0.031$		(9)
Spitzer MIPS 160 $\mu\text{m}$	$0.555 \pm 0.066$		(9)
Akari IRC 8 $\mu\text{m}$	$0.404 \pm 0.018$		(10)
Akari IRC 18 $\mu\text{m}$	$0.120 \pm 0.080$		(10)
Akari FIS 90 $\mu\text{m}$	$0.488 \pm 0.074$		(11)
	[mJy]		
CSO/SHARCII 350 $\mu\text{m}$	$89 \pm 26$		(12)
JCMT 850 $\mu\text{m}$	$10.3 \pm 1.8$		(13)
JCMT 1100 $\mu\text{m}$	< 33		(14)
IRAM 1200 $\mu\text{m}$	$4.8 \pm 2.7$		(14)

References: (1) The USNO-B1.0 Catalog (Monet et al., 2003); (2) NOMAD Catalog (Zacharias et al., 2004), from Tycho-2 Catalog (Høg et al., 2000); (3) The Guide Star Catalog, Version 2.3.2 (Lasker et al., 2008); (4) The Hipparcos and Tycho Catalogues (Perryman & ESA, 1997); (5) 2MASS All-Sky Catalog of Point Sources (Skrutskie et al., 2006); (6) IRAS catalogue of Point Sources, Version 2.0 (Helou & Walker, 1988); (7) IRAS Faint Source Catalog,  $|b| > 10$ , Version 2.0 (Moshir et al., 1990); (8) Moór et al. (2006); (9) Su et al. (2009); (10) The AKARI/IRC mid-infrared all-sky survey (Ishihara et al., 2010); (11) AKARI/FIS All-Sky Survey Point Source Catalogues (Yamamura et al., 2010); (12) Patience et al. (2011); (13) Williams & Andrews (2006); (14) Sylvester et al. (1996)

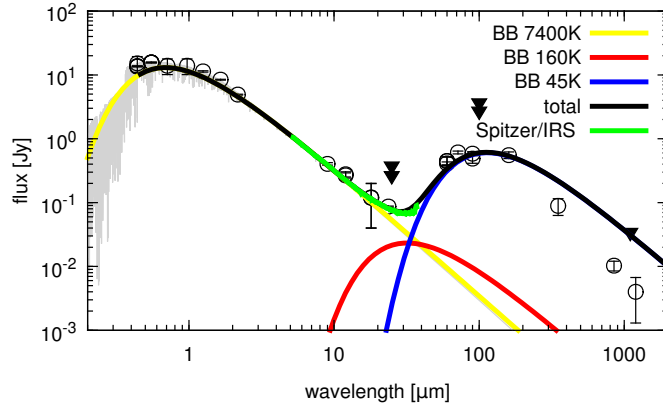


**Figure 3.11:** Spectral energy distribution of HR 8799. Circles are photometric measurements, triangles are upper limits (Table 3.3). The green line between  $\approx 5$  and  $40 \mu\text{m}$  is the Spitzer/IRS spectrum. Underlaid is the best-fit NextGen model (gray line) for the stellar photosphere. The yellow, red and blue lines are black-body approximations for the stellar photosphere, the inner, and outer disk, respectively, which are used to calculate the color-correction factor.

maximum grain radius, which has little effect on the results, was arbitrarily set to be 1 mm.

At first, we modeled the SEDs that would be produced by four hypothetical dust rings with arbitrarily chosen extensions. Since we knew only about three planets at that time, we located the rings inside the orbit of planet HR 8799 d, between d and c, between c and b, and outside the orbit of the outermost planet HR 8799 b (Table 3.4).

**Table 3.4:** Locations and names of the first-guess dust rings.

ring location	ring extension [AU]	name
inside d	3–15	ring d
between d and c	28–32	ring cd
between c and b	45–60	ring bc
outside b	75–125	ring b

Comparison of the first-guess model SEDs with the available photometry and spectrometry observations shows that one single ring is incapable of reproducing the entire set of observations from the mid- to the far-infrared. Taking this into account, we used two rings, an inner one, and an outer one. Since the fourth planet was found with a projected distance of 15 AU, we placed the outer edge of the inner ring further inward at 10 AU, avoiding the chaotic zone of overlapping resonances ( $\Delta a \sim \mu^{2/7} a_P$ , Duncan et al., 1989; Murray & Dermott, 2000). In our ‘best fit’ model (Fig. 3.12) we

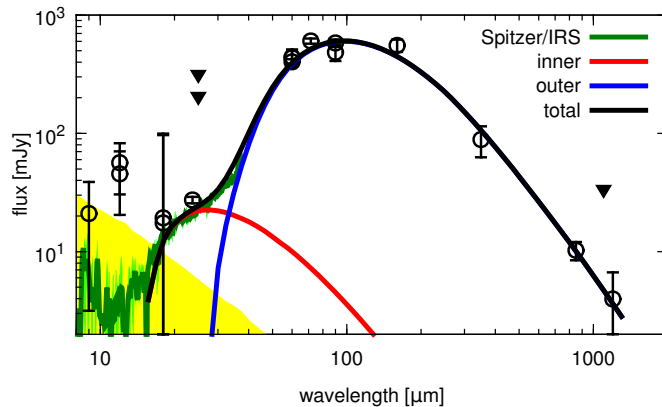


**Figure 3.12:** Excess emission of HR 8799, assuming the stellar photosphere as black body with  $T_{\text{eff}} = 7400$  K. The circles are the observed fluxes, and the triangles are upper limits. The green line is the IRS spectrum. The black line is the sum of the contribution of the inner ring (red) and the outer ring (blue). The yellow area gives the estimated uncertainty for the photosphere.

used for the inner ring an extension from 3–10 AU, a minimum size of  $2 \mu\text{m}$  and a dust mass of  $1.1 \times 10^{-5} M_{\oplus}$ . For the outer ring we fit  $r = 100\text{--}125$  AU,  $s_{\text{min}} = 6 \mu\text{m}$ , and  $m_{\text{d}} \approx 5 \times 10^{-2} M_{\oplus}$ . As a word of caution, we recall that these estimates depend on the uncertainty in the IRS spectrum calibration, as discussed in Sect. 3.3.1, which is a factor of several in dust mass.

A question arises whether these fits are physically reasonable. Thus, we checked the impact of moderate variations in the slopes ( $0.1 \leq \xi \leq 1.9$  and  $2.5 \leq q \leq 4.5$ ). The slope of the spatial distribution  $\xi$  was found to have little effect on the results, moderately changing only the short-wavelength part in the SED from the inner dust ring. The size distribution slope  $q$ , however, affects the resulting emission appreciably. While for the inner ring the changes are still small (a steeper slope would amplify silicate features at 10 and 20  $\mu\text{m}$ , whereas a shallower distribution would remove them, as expected), similar changes in the outer ring would require strong compensation by altering other disk parameters (which were fixed in our approach). The reason is that for the outer component both the rise and the fall of the SED are well constrained by photometric observations. They place tight constraints on the width of the SED, in contrast to the inner ring where only the short-wavelength part of the SED is known. Since dust in the outer ring is much colder than in the inner ring it is no longer the strength of the features but the width of the SED that is affected by a different slope in the size distribution: the steeper the distribution, the narrower the SED. On any account, to determine the rough location and mass of dust the simple fitting approach used here is sufficient.

Another question is how well the edges of the outer and inner ring are constrained. To check this, we varied them and fitted the SED again, leaving the lower cutoff size and dust mass as free parameters. For the outer ring, we found reasonable fits with the inner edge between 75 and 120 AU and the outer edge between 125 and 170 AU (for  $q = 3.6$  and  $\xi = 1$ ). The outer edge in the inner ring can range from 5 to 10 AU. Truncated further inward, the inner ring provides even slightly closer agreement with the IRS spectrum between 20 and 30  $\mu\text{m}$ . However, because of calibration uncertainties, it is difficult to assess the accuracy of the fit, which leaves the outer edge of the inner ring rather unconstrained. The inner edge of the inner ring can be as close to the star as 2 AU to conform to the IRS spectrum, especially by assuming slightly larger particles (e.g.  $s_{\min} = 6 \mu\text{m}$ ).

Spitzer/MIPS images provide marginal resolved images of the disk. At least, Su et al. (2009) constrain the outer edge of the outer disk to  $\approx 300$  AU. Further, they conclude from surface brightness profiles a huge halo  $\sim 1\,000$  AU of small particles. The inner region, including the inner edge of the outer disk, the gap, and the inner disk, is not resolved.

So far we have discussed *dust* rings in the system. However, the presence of a dust belt requires a belt of *planetesimals* that are not evident in the observations, but produce and sustain visible dust. Because of the radiation pressure effect, dust grains typically move in orbits with periastra at the planetesimal belt and apastron outside it. The smaller the grains, the farther out from the star they are spread (cf. Eqs. (2.16)). Thus, the dust-producing planetesimal belt is expected to be narrower than the observed dust ring and to be located within the dust ring close to its inner edge (e.g., Krivov et al., 2006). Therefore, we expect the outer planetesimal belt to be located at  $\sim 75\text{--}120$  AU and the inner planetesimal belt at 2–10 AU from the star. It is important to check whether the expected locations of the outer and inner planetesimal belt are dynamically compatible with the presence of the outermost and innermost planet, respectively. We investigate this in Sect. 3.4, by trying to identify additional constraints on the location of the two rings.

### 3.4 Dynamical interactions between planets and planetesimals

Beside the constraints from the SED-model, we also checked if or how far the outer and inner planetesimal belts (which maintain dust rings b and d) would be truncated by

the planets. Since we could not find a stable solution for the four planet case, only the results with the three outer planets are presented in this section. To analyze how the planetesimal belts would be truncated, we chose one exemplary angle configuration from within the “stability spot” seen in Fig. 3.6. The point chosen is  $(i, \Omega) = (30^\circ, 10^\circ)$ , which implies initial semimajor axes of 74.7, 41.8, and 24.6 AU for HR 8799 b, c, and d, respectively.

We launched 1 000 massless planetesimals in orbits with uniformly distributed orbital elements ( $e_p = 0\text{--}0.2$ ,  $I_p = 0\text{--}10^\circ$ ,  $\{\omega_p, \Omega_p, \mathcal{M}_p\} = 0\text{--}360^\circ$ ). Of these, 200 planetesimals were initially confined to a ring in the range  $a_{\text{inner}} = 10\text{--}20$  AU and the other 800 in the range  $a_{\text{outer}} = 90\text{--}130$  AU. We integrated their orbits over 100 Myr with an accuracy of  $10^{-12}$  for low and nominal planetary masses, as given in Table 3.2. The high-mass case was excluded, because the stability of companions themselves at  $(i, \Omega) = (30^\circ, 10^\circ)$  was only marginal.

Figure 3.13 shows that both the inner part of the outer ring and the outer part of the inner ring are swiftly cleared by the adjacent planet (b and d, respectively). The belt of remaining planetesimals develops “Kirkwood gaps” at the positions of major resonances. Over tens of Myr, the gaps become progressively more pronounced. Simultaneously, the fraction of particles surviving between them gradually decreases. As expected, the survival probability of planetesimals at a given distance is higher for lower companion masses.

For both rings and for the nominal- and low-mass cases, Fig. 3.14 presents the fraction of planetesimals that survived after 100 Myr in orbits with different initial semimajor axes. For nominal planetary masses, the outer ring experiences considerable depletion, with only  $\sim 10$  to 20% planetesimals surviving even outside 120 AU. There are almost no survivors inside the 5:3 and 7:4 resonances with HR 8799 b at  $\approx 105\text{--}110$  AU. In the low-mass case, the survival fraction in the outer ring is appreciably higher (15–70% between  $\approx 110\text{--}130$  AU). The inner ring retains 80–100% of planetesimals inside 11 AU. The outer edge of the ring is between 13 AU (nominal-mass planet) and 15 AU (low-mass one).

These results have to be compared with dust locations found from the SED fitting in Sect. 3.3.2. As noted there, the far-infrared to millimeter part of the SED implies that dust in the outer ring as close as 120 AU from the star; we have just shown that a significant fraction of planetesimals survives outside 120 AU after 100 Myr, at least in the low-mass case. In the nominal-mass case, the fraction of survivors is lower, but any firm conclusions appear premature, since the location of the outer ring is

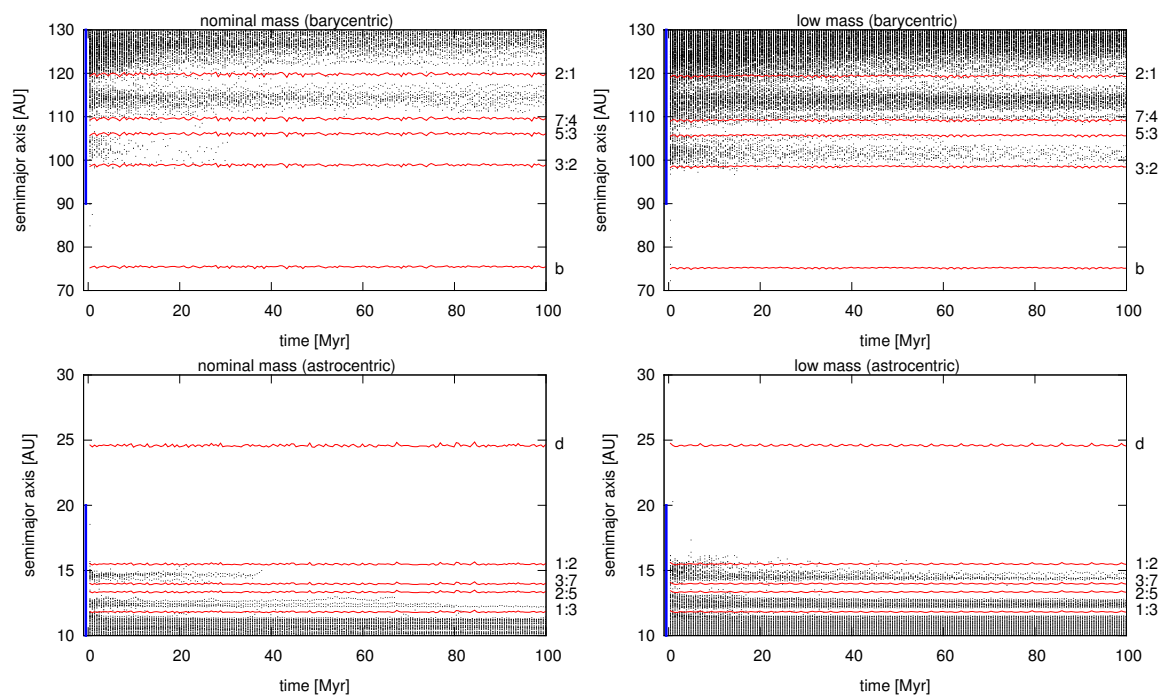


**Figure 3.13:** Evolution of semimajor axes of planetesimals over 100 Myr for the nominal (*left*) and the low (*right*) planet masses. Initial planetesimal rings are shown with blue vertical bars. Solid red lines represent the semimajor axes of planets (b, d) and important resonances. Note that the outer ring (*top*) is plotted in barycentric osculating elements and the inner ring in astrocentric ones. This choice leads to a sharper visibility of the resonance positions.

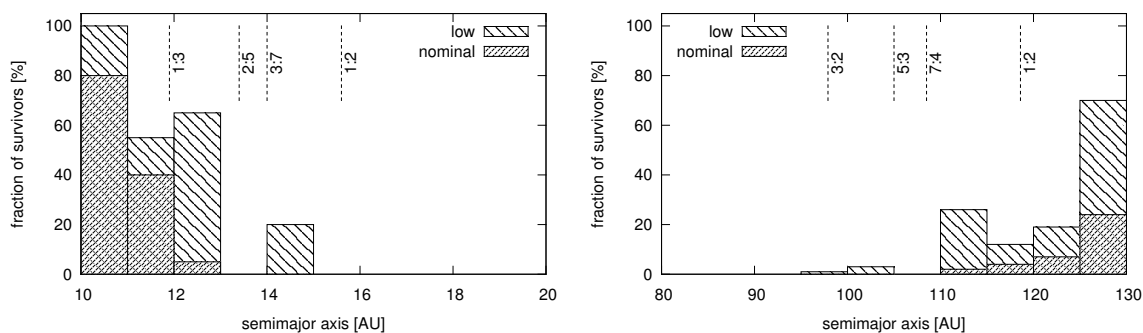


**Figure 3.14:** Fraction of left-over planetesimals after 100 Myr of evolution in the inner (*left*) and outer (*right*) rings, for a low-mass and nominal-mass case.

not well-constrained (see Sect. 3.3.2). Next, the IRS spectrum interpretation requires dust in the inner ring at least 10 AU away from the star. This is comfortably within the stability zone inside the orbit of HR 8799 d for both the nominal-mass and low-mass cases. Moreover, 10 AU quoted above is the distance where *dust* is required; as discussed in Sect. 3.3.2, the parent planetesimals would orbit closer to the star, being yet safer against the perturbations of the innermost planet than their dust. In summary, our analysis of the outer system might slightly favor the low-mass case, but would not really pose any additional strong constraints on the planetary masses.

### The fourth planet

To study the implications of the fourth planet, we did not use the simulations, since we could not find a stable configuration with all four planets (see Sect. 2.2). Instead, we extrapolated the impact of the third planet HR 8799 d on the inner planetesimal belt. HR 8799 d truncates the inner ring down to approximately 12 AU, which is roughly twice the width of its chaotic zone ( $\Delta a \sim \mu^{2/7} a_P$ , Duncan et al., 1989; Murray & Dermott, 2000). Assuming HR 8799 e at  $\approx 15$  AU with a (low) mass of  $7M_{\text{Jup}}$ , the disk would be truncated at  $\approx 8$  AU, which is still consistent with our disk model presented in Sect. 3.3.2.

## 3.5 Conclusions and discussion

### 3.5.1 Conclusions

We have attempted a coherent analysis of various portions of observational data available for the system of the nearby A5 V star HR 8799, which hosts debris dust as well as four planetary candidates discovered by direct imaging (Marois et al., 2008, 2010). A dedicated analysis of all known components of the system (the central star, imaged companions, and dust) leads us to a view of a complex circumstellar system (Fig. 3.15). It contains at least four planets in nearly-circular coplanar orbits bordered by two dust-producing planetesimal belts, one outside the planetary region, and another inside. Each planetesimal belt is surrounded by a dust disk. The outer dust disk may have a considerable extension, of perhaps several hundreds of AU.



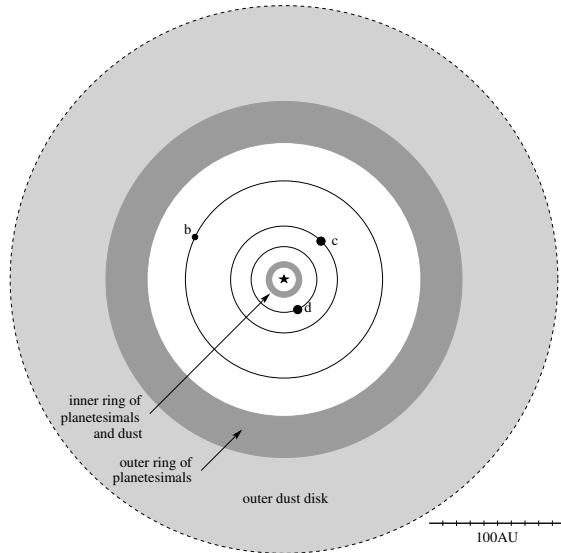


**Figure 3.15:** A schematic view of the system HR 8799.

Our specific conclusions are as follows:

1. With previous estimates of stellar age ranging from  $\approx 20$  to  $\approx 1100$  Myr, the high luminosity of the observed cold dust may favor younger ages of  $\lesssim 50$  Myr. A younger age would automatically lower the masses of all four companions, estimated by evolutionary models, making the masses more consistent with dynamical stability results (see conclusion item 5).
2. The system is seen nearly pole-on. Our analysis of the stellar rotational velocity suggests an inclination of  $13\text{--}30^\circ$ , whereas  $i \gtrsim 20^\circ$  seems to be mandatory for the system to be dynamically stable (see conclusion item 5). Thus, we arrive at a probable inclination range of  $20\text{--}30^\circ$ .
3. Our analysis of the available mid-infrared to millimeter photometry and spectrophotometry data infers the presence of two dust rings, and therefore two parent planetesimal belts, an “asteroid belt” at  $\sim 10$  AU and a “Kuiper belt” at  $\gtrsim 100$  AU. The dust masses are estimated to be  $\approx 1.1 \times 10^{-5} M_\oplus$  and  $5 \times 10^{-2} M_\oplus$  for the inner and outer ring, respectively.
4. Assuming that the system is indeed rather young ( $\lesssim 50$  Myr) and based on the photometry of the companions reported by Marois et al. (2008, 2010), our estimates with several evolutionary models suggest that the masses of the companions are lower than 7 to  $10 M_{\text{Jup}}$ .
5. We show that all three planets may be stable in the mass range suggested in the discovery paper by Marois et al. (2008,  $5\text{--}13 M_{\text{Jup}}$ ), but only for some of all possible orientations. For  $(m_b, m_c, m_d) = (5, 7, 7) M_{\text{Jup}}$ , an inclination  $i \gtrsim 20^\circ$

is required and the line of nodes of the system’s symmetry plane on the sky must lie within  $0^\circ$  to  $50^\circ$  from north eastward. For higher masses  $(m_b, m_c, m_d)$  from  $(7, 10, 10)M_{\text{Jup}}$  to  $(11, 13, 13)M_{\text{Jup}}$ , the constraints on both angles are even more stringent. The stability of the two inner planets is caused by locking in the 1:2 mean-motion resonance, and the stability of the outer couple is supported by the 1:2 commensurability, too. However, in many stable cases only one of the two resonances is strong. Another one is often shallow, with a circulating rather than librating resonant argument. For “wrong” orientations, the stability only seems possible with planetary masses lower than most evolutionary models would predict even for the youngest possible age (cf. Table 3.1). Should this be the case, this would necessitate revisions to the models.

6. The dynamical stability deteriorated with the finding of the fourth planet. Only a few tens of Myr could be reached in our simulations with all four planets in the low-mass case with  $5\text{--}7M_{\text{Jup}}$ . The region of stability in the  $(i, \Omega)$ -phase space was additionally confined by the 1:2 resonance of d-e, encouraging the assumptions of configuration within a multiple resonance.
7. Both dust/planetesimal belts appear to be dynamically stable against planetary perturbations, provided the masses of companions are such that they themselves are dynamically stable against mutual perturbations.

### 3.5.2 Prospects for future observations

While plenty of new observations have become available in the last years, many of the quantitative estimates listed above are still uncertain. However, there is little doubt that new observations will arrive in future times, verifying our estimates and on any account reducing the uncertainties. First, additional observations of the planets themselves are expected. More accurate astrometry, and therefore a more accurate determination of the orbits, should become possible with future instruments and improved methods of astrometric observations, and because of the longer time spans. Next, new photometry observations are needed. The companions have been detected so far in J, H, K, L’,  $3.3\mu\text{m}$  and M’. The SED is relatively flat in this wavelength range for objects with temperatures of roughly 500 K to 1500 K. Imaging photometric detections of the companions in Gunn z ( $1\mu\text{m}$ ) must be possible with 8 to 10 m class telescopes. This would allow one to constrain the objects’ temperature, because the colors z-J and L-M and their differences depend strongly on temperature over the relevant range of between 500 K and 1500 K. Spatially resolved spectroscopy of the

companions may be possible with VLT/Sinfoni or Subaru/IRSC, but would be very challenging. If successful, this would place tighter constraints on temperature and gravity and, hence, the radius and mass of the companions.

Secondly, new data on the dust portion of the system would be particularly promising. For instance, a more accurate mid-infrared photometry would provide more reliable dust mass and location of the inner dust belt (“exozodi”). One could also consider of near- and mid-IR interferometry observations, which have proven to be very successful not only for exozodi studies, but also for stellar radius determination (see, e.g., Di Folco et al., 2004; Absil et al., 2006; Di Folco et al., 2007; Absil et al., 2008). While HR 8799 is too faint to be observed with the presently operating CHARA/FLUOR and Keck Interferometer Nuller instruments (e.g., for CHARA the  $K$ -magnitude of  $\lesssim 4$  mag is needed, whereas HR 8799 has  $K = 5.2$  mag), this should become possible in the near future, for instance with VLTI/PIONIER and the LBTI Nuller. More observational effort is required for the outer disk as well. Resolving the outer debris disk, especially in scattered light, would answer several key questions at a time. On the one hand, it would further constrain the inclination of the entire system and the orientation of its line of nodes on the sky plane, drastically reducing the parameter space assumed in the dynamical simulations. On the other hand, the precise location of the inner rim of the outer disk could place a direct upper limit on the mass of HR 8799 b, in much the same way as achieved for the Fomalhaut planet (Kalas et al., 2008; Chiang et al., 2009).

Once the location and masses of the dust belts are constrained more tightly by observations, it will become possible to access the position, masses, and other properties of directly invisible planetesimal belts that produce and sustain that dust. This could be done with the help of elaborate collisional models (Krivov et al., 2008). The results could provide additional clues to the formation history of the system.

### 3.5.3 Origin and status of the system

The HR 8799 system is a prominent example for a full (and tight) planetary system. Furthermore, it is not the only system with directly imaged companions whose masses most likely fall into the “planetary” (as opposed to brown dwarf) range. Nevertheless, HR 8799 does appear to be unique for the moment. The orbits of its companions extending up to  $\approx 70$  AU are large, and their masses are also probably almost at the limit of their dynamical stability against mutual perturbations. Even though we strongly argue that the masses are well below the deuterium burning limit, it

is not clear whether the companions have formed in a “planetary” way (from the protoplanetary disk) or “stellar” way (as a multiple stellar system). In this sense, it remains questionable whether we are dealing with “true” planets. An argument in favor of the “stellar” formation would be, for instance, a low metallicity ( $\text{Fe}/\text{H} \approx -0.47$ , Gray & Kaye, 1999), atypical of – although not the lowest among – the known planet host stars. The low metallicity is particularly unusual for a system with several high-mass planets. “Planetary” way of formation in situ could be feasible by means of the gravitational instability (GI) (Cameron, 1978; Boss, 1998). For GI to work, the density of the protoplanetary disk should exceed the Toomre density (Toomre, 1964). At the same time, it should be low enough to allow efficient cooling, which is required for a disk to fragment into bound clumps (Gammie, 2001). Both radiative and convective cooling rates may not be efficient enough for direct formation of giant planets by GI within several tens of AU from the parent star (Rafikov, 2005, 2007; Nero & Bjorkman, 2009). Further, Kratter et al. (2010) note that atypical disk conditions are required to form companions with planetary masses via this mechanism. In contrast Boss (2011) claims that gravitational instability appears to be a likely formation process of the system. As far as the standard core accretion scenario is concerned, the only possible way of explaining the formation of planets with several Jupiter masses would be to assume that they have formed closer to the star and then scattered gravitationally to wider orbits (e.g., Veras & Armitage, 2004). Nevertheless, it is difficult to find a mechanism that has circularized their orbits subsequently. Alternatively, massive planets formed by core accretion could have smoothly migrated from their birth places outward. However, this would require displacing a comparable – and therefore an unrealistically large – mass of planetesimals inward over large distances, casting doubt on this mechanism. Thus, by and large it is still controversial how the planets have formed. The era of directly imaged extrasolar planets that has just begun should eventually bring answers to these and many other questions.

# Chapter 4

## $\varepsilon$ Eridani

*This chapter is based on the paper “The cold origin of the warm dust around  $\varepsilon$  Eridani” (Reidemeister et al., 2011). I made major contributions to the study of the dust dynamics in the inner system and the SED modeling. Other parts of this study were done in collaboration with Alexander Krivov, Christopher C. Stark, Jean-Charles Augereau, Torsten Löhne, and Sebastian Müller.*

The second full planetary system we investigated was the nearby ( $\sim 3.2$  pc) K2 V star  $\varepsilon$  Eridani (HD 22049, HIP 16537, HR 1084) with an age of  $\lesssim 1$  Gyr (Saffe et al., 2005; Di Folco et al., 2004; Song et al., 2000; Soderblom & Dappen, 1989). As in the HR 8799 system a ring of cold dust at  $\sim 65$  AU is seen in resolved sub-millimeter images (Greaves et al., 1998, 2005), which encompasses an inner disk of warm dust revealed by Spitzer/MIPS (Backman et al., 2009). The excess emission at  $\lambda \gtrsim 15 \mu\text{m}$  in a Spitzer/IRS-spectrum (Backman et al., 2009) indicates that there is warm dust close to the star, at a few AU (inset in Fig. 4.1). Its origin is unknown, as an inner “asteroid belt” that could produce this dust would be dynamically unstable (Brogi et al., 2009) because a radial velocity planet (Hatzes et al., 2000) with a semimajor axis of 3.4 AU orbits the star. Another outer planet is expected to orbit near  $\sim 40$  AU, producing the inner cavity and clumpy structure in the outer ring (Liou & Zook, 1999; Ozerney et al., 2000; Quillen & Thorndike, 2002; Deller & Maddison, 2005).

Here, we check the possibility that the source of the warm dust is the outer ring from which dust grains could be transported inward by Poynting-Robertson drag and stellar wind. The importance of the latter for debris disks around late-type, low-mass stars was first pointed out by Plavchan et al. (2005), and it is known that  $\varepsilon$  Eridani does have strong winds (Wood et al., 2002).

It is convenient to divide the entire system into three regions: the outer “Kuiper belt” (55–90 AU), the intermediate zone (10–55 AU), and the inner region (inside 10 AU), see Fig. 4.1. In Sect. 4.1 we describe our modeling setup, and in Sect. 4.2, how we model the dust production in the outer ring and its transport through the intermediate region. Section 4.3 describes simulations of the inner system. Section 4.4 presents the SED modeling and provides an additional check for connection between the inner

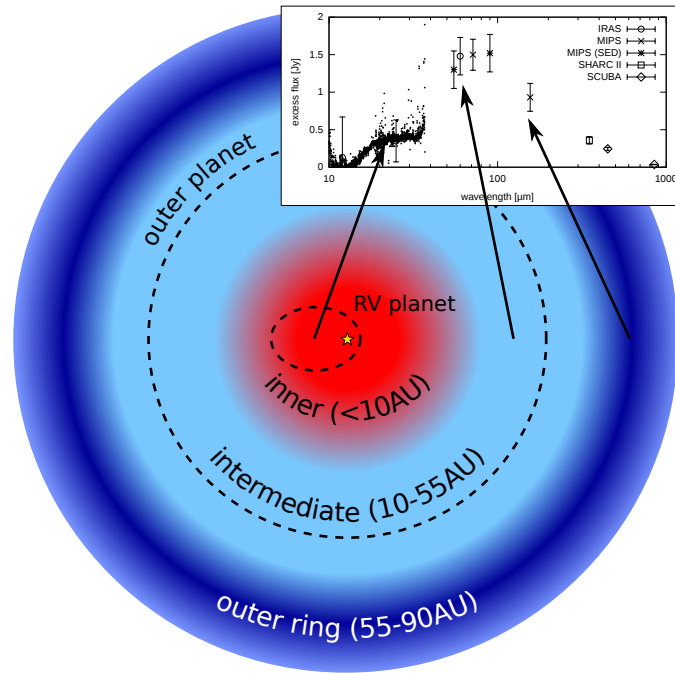


**Figure 4.1:** A schematic view of the  $\varepsilon$  Eridani system’s architecture. The outer ring is the region where the dust is produced by parent planetesimals; the intermediate zone is the one where it is transported inward by drag forces, possibly interacting with a presumed outer planet; transport continues through the inner region where dust interacts with the known inner planet. The outer part of the sketch ( $> 10$  AU) is not to scale. *Inset:* The observed SED. The IRS spectrum (dots) stems from dust in the inner region and exhibits a characteristic “plateau” (“shoulder”) at  $\lambda \approx 20$ – $30 \mu\text{m}$ . The main part of the SED with a maximum at  $\lambda \approx 70$ – $80 \mu\text{m}$ , well probed by several photometry points (symbols with error bars), derives from the outer and intermediate regions.

system and the outer parent ring (Sect. 4.4.4). Section 4.5 focuses on the surface brightness profiles. Section 4.6 contains our conclusions.

## 4.1 Model setup

### 4.1.1 Method

Our model includes gravitational forces from the star and an inner planet, radiation and stellar wind pressure, drag forces induced by both stellar photons and stellar wind particles (Burns et al., 1979), as well as collisions. Dust production in the outer region and dust transport through the intermediate region are modeled with a

statistical collisional code. To study the dust in the inner region, we need to handle dust interactions with the inner planet. These cannot be treated by the collisional code, so we model the inner region by collisionless numerical integration.

### 4.1.2 Stellar properties

We assumed a stellar mass of  $M_\star = 0.83M_\odot$  (Benedict et al., 2006) and a luminosity of  $L_\star = 0.32L_\odot$  (Di Folco et al., 2004). For the stellar spectrum we used a NextGen model (Hauschildt et al., 1999) with an effective temperature of 5200 K,  $\log g = 4.5$ , solar metallicity, and stellar radius  $R_\star = 0.735R_\odot$  (Di Folco et al., 2007).

### 4.1.3 Dust grain properties

The knee in the IRS spectrum at  $\sim 20 \mu\text{m}$  (inset in Fig. 4.1) is reminiscent of a classical silicate feature. Since the exact composition of those silicates is not known, we have chosen astronomical silicate (Laor & Draine, 1993) ( $\rho_d = 3.5 \text{ g cm}^{-3}$ ). On the other hand, by analogy with the surface composition of Kuiper belt objects in the Solar System (e.g., Barucci et al., 2008), we may expect many additional species such as ices and organic solids. In particular, it is natural to expect water ice to be present, especially given that the source of dust is a “Kuiper belt” located very far from the star ( $\sim 55\text{--}90 \text{ AU}$ ), and the star itself has a late spectral class. Accordingly, we also tried homogeneous mixtures of astrosilicate with 50% and 70% volume fraction of water ice (Li & Greenberg, 1998) ( $\rho_d = 1.2 \text{ g cm}^{-3}$ ). The bulk density of these ice-silicate mixtures is  $\rho = 2.35 \text{ g cm}^{-3}$  and  $\rho = 1.89 \text{ g cm}^{-3}$ , respectively. The optical constants of the mixtures were calculated by effective medium theory with the Bruggeman mixing rule. In all three cases (pure astrosilicate, two ice-silicate mixtures) the dust grains were assumed to be compact spheres.

### 4.1.4 Radiation pressure and stellar wind

Using the optical constants and adopting Mie theory, the radiation pressure efficiency  $Q_{\text{rp}}$ , averaged over the stellar spectrum, was calculated as a function of size  $s$  (Burns et al., 1979; Gustafson, 1994). We then computed the radiation pressure to gravity ratio,  $\beta$  (Fig. 4.2). The resulting  $\beta(s)$  was utilized to compute the direct radiation pressure and Poynting-Robertson forces.

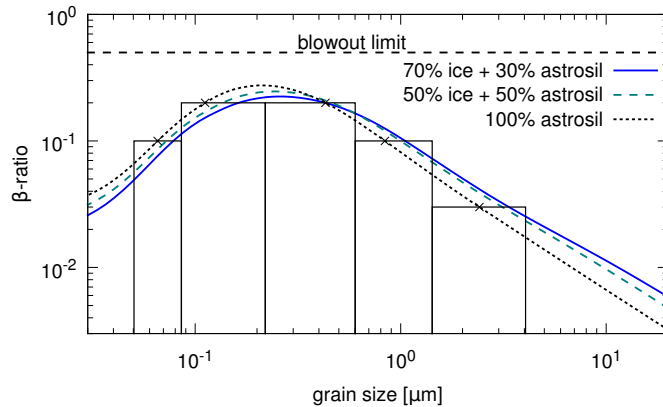


**Figure 4.2:** The  $\beta$  ratio of two mixtures of silicate and water ice, compared to a pure silicate composition, as a function of size for  $\varepsilon$  Eri. The bars show the size bins used in the inner disk simulations (Sect. 4.3). The dashed horizontal line shows the dynamical blowout limit of  $\beta = 0.5$ .

The stellar wind was included by a factor  $\beta_{\text{sw}}/\beta$ , which is the ratio of stellar wind pressure to radiation pressure (cf. Eq. (2.20)). We adopted for the absorption efficiency factor for stellar wind pressure  $Q_{\text{sw}} = 1$ . Assuming a stellar wind velocity equal to the average solar wind velocity,  $v_{\text{sw}} \approx 400 \text{ km s}^{-1}$ , and using a mass-loss rate of  $\dot{M}_{\star} \approx 30\dot{M}_{\odot}$  (Wood et al., 2002), we get  $\beta_{\text{sw}} = 3.69 \times 10^{-2}\beta$ . In this estimate (but not in the simulations), we set  $Q_{\text{rp}}$  to unity. Thus direct stellar wind pressure is approximately 27 times weaker than radiation pressure. However, the stellar wind drag is  $(\beta_{\text{sw}}/\beta)(c/v_{\text{sw}}) \approx 28$  times stronger than radiation (Poynting-Robertson) drag.

### 4.1.5 Sublimation

Using an ice-silicate mixture for dust raises a question whether and where the icy portion of the dust grains will suffer sublimation. The ice sublimation temperature of  $\sim 100 \text{ K}$  (e.g., Moro-Martín & Malhotra, 2002; Kobayashi et al., 2008) is reached at  $\approx 10 \text{ AU}$  (Fig. 4.3). Mukai & Fechtig (1983) proposed that fluffy and nearly homogeneous grains of ice and silicates can produce a core of silicate after sublimation of ice. Assuming a grain with a volatile icy mantle, instead of a homogeneous sphere of ice and silicates, would lead to the same result. In both cases, the silicate cores left after ice sublimation continue to drift further inward. Within the ice sublimation distance, the optical depth would decrease by the volume fraction of the refractories (see Kobayashi et al., 2008, their Eq. (35)). The shape of the size distribution is not affected by sublimation, as long as the volume fraction of ice is independent of the grain size.



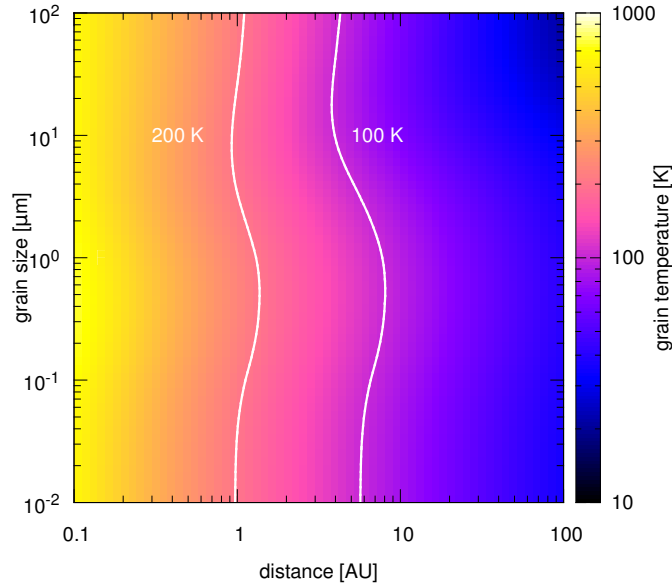


**Figure 4.3:** Equilibrium grain temperature of an 70% ice and 30% astronomical silicate composition depending on grain size  $s$  and distance to the star  $r$ . The results for the 50% ice – 50% silicate mixture are similar. The wavy shape of the isotherms is caused by the dependence of the absorption efficiency on the grain size (as explained in Krivov et al., 2008, see their Figs. 2 and 6).

Thus we expect the entire dust disk to consist of an inner silicate disk ( $r \lesssim 10$  AU) and an outer disk of an ice-silicate composition. Accordingly, in integrations described in Sect. 4.3 we assumed dust inside 10 AU to consist of pure astrosilicate. Outside 10 AU, we tried all three dust compositions described above.

We finally note that a ring due to sublimation as described in Kobayashi et al. (2008, 2009) is not expected, because such a ring can only be produced by particles with high  $\beta$  ratios ( $\beta \gtrsim 0.1$ – $0.3$ ). Such  $\beta$  ratios are barely reached in the  $\varepsilon$  Eri system even for pure silicate dust.

## 4.2 Dust in the outer and intermediate region

### 4.2.1 Model

We used our statistical collisional code *ACE* (*Analysis of Collisional Evolution*, Krivov et al., 2005, 2006; Löhne et al., 2008) to model the collisional disk beyond 10 AU. This includes the parent ring near 65 AU (Greaves et al., 2005) and the intermediate region

inside it. The *ACE* simulation provides us with a rotationally-symmetric steady-state dust size distribution at 10 AU, which we use later as input for our non-collisional models of the inner disk (see Sect. 4.3). The code is not able to treat planetary perturbations. Thus we neglect the presumed outer planet, but will qualitatively discuss its possible influence in Sects. 4.2.2 and 4.4.

We made three *ACE* runs, assuming the dust composition to be pure astrosilicate, a mixture of ice and astrosil in equal parts, and a mixture of 70% ice and 30% astrosil, as described above. In handling the collisions, we used the power-law description of the critical specific energy for fragmentation and dispersal  $Q_D^*$  from Eq. (2.35) and took the values  $A_s = 10^7 \text{ erg g}^{-1}$ ,  $A_g = 10^7 \text{ erg g}^{-1}$ ,  $3b_s = -0.37$ , and  $3b_g = 1.38$  (cf. Benz & Asphaug, 1999). In all *ACE* runs, we assumed that the outer ring has a uniform surface density between 55 and 90 AU and that the eccentricities of parent planetesimals range between 0.0 and 0.05, and arbitrarily set the semi-opening angle of the disk to  $3^\circ$ . Next, we assumed that the *initial* size distribution index of solids from km-sized planetesimals down to dust is  $q \sim 3.6$  (see, e.g., Löhne et al., 2008, for a justification of this choice). The current dust mass was set to  $m(s < 1 \text{ mm}) \approx 10^{-3} M_\oplus$ , based on previous estimates from sub-millimeter images (Greaves et al., 1998, 2005).

## 4.2.2 Results

Figure 4.4 (left) shows the resulting size distribution in an *evolved* disk at several distances from the star. It shows the case of a mixture of 70% ice and 30% astrosil, but the results for the two other compositions are qualitatively similar. We start a discussion of it with the parent ring (55–90 AU). For grains larger than  $s_c \approx 10 \mu\text{m}$ , the differential size distribution has a slope  $q \approx 3.7$ . Since Fig. 4.4 (left) plots the optical depth per size decade, this corresponds to a slope of  $q - 3 = -0.7$ . This is close to what is expected theoretically for collision-dominated disks (Dohnanyi, 1969). However, from  $s_c \approx 10 \mu\text{m}$  down to the smallest grains, the size distribution flattens, because the inward drift is faster for smaller grains – or, more exactly, for grains with higher  $\beta$ -ratios (see, e.g., Strubbe & Chiang, 2006; Vitense et al., 2010, for a more detailed discussion of this phenomenon). The slope calculated analytically for a transport-dominated disk with  $\beta \propto s^{-1}$  is  $q \approx 2.5$ . The actual size distribution is wavy, and is rather close to  $q = 3.0$ , which would correspond to a uniform distribution of the optical depth across the sizes. One reason for that is a nonlinear dependence of  $\beta$  on the reciprocal of particle size (Fig. 4.2).

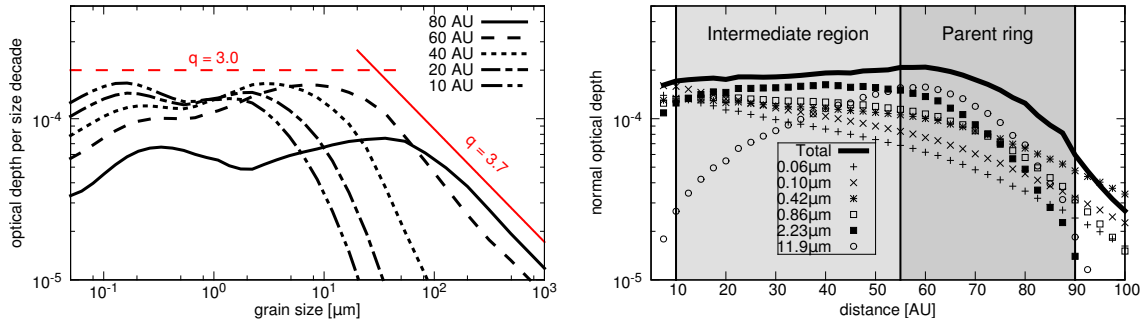


**Figure 4.4:** *Left:* Size distribution at different distances in a disk composed of 70% ice and 30% silicate, simulated with *ACE*. Curves depict the normal geometrical optical depth per size decade, as a function of size. The straight lines show power laws with  $q = 3.0$  and  $3.7$  for comparison. (Their height is arbitrary.) *Right:* Radial profiles of the optical depth. Symbols: partial contributions to the optical depth by several selected sizes. Each contribution is normalized to the unit size decade around that size. Solid line: the total optical depth of the disk.

Closer to the star, the slope for big grains progressively steepens because of their preferential collisional elimination. At the same time, the break  $s_c$  in the size distribution moves to smaller sizes. Already at 20 AU, particles larger than  $\sim 10 \mu\text{m}$  are almost absent. At 10 AU, the cutoff shifts to  $s \sim 4 \mu\text{m}$ . We argue that a progressive depletion of larger grains with decreasing distance will be strengthened further by the alleged outer planet at 40 AU. That planet, which presumably sculpts the outer ring, would stop bigger grains more effectively than smaller ones, by trapping some of them in mean-motion resonances (MMRs) and scattering the others (Liou et al., 1996; Moro-Martín & Malhotra, 2003; Moro-Martín & Malhotra, 2005). As a result, we do not expect any grains larger than about 1–10  $\mu\text{m}$  ( $\beta \lesssim 0.1$ –0.01) throughout most of the intermediate zone and in the entire inner region. At the same time, the outer planet is not expected to be an obstacle for smaller particles that, as discussed below, will be the most important for the mid-IR part of the SED.

From the same *ACE* run for the outer and intermediate regions, we found that  $\tau$  is nearly constant from 55 AU down to 10 AU (Fig. 4.4 right). This optical depth is dominated by submicron-sized and micron-sized grains. A constant optical depth inward from the sources is known to be a characteristic feature of transport-dominated disks (e.g Briggs, 1962; Wyatt, 2005). However, disks with the optical depth of  $\tau \gtrsim 10^{-5}$  are usually thought to be collision-dominated (Wyatt, 2005), and one might not expect that even the amplification of the Poynting-Robertson drag by stellar wind drag would increase the critical optical depth (that separates the transport- and collision-dominated regimes) by more than an order of magnitude. This raises a natural ques-

tion: how can it be that a disk with the optical depth of  $\sim 2 \times 10^{-4}$  is transport-dominated? To find an answer, we note that  $s_c$  discussed above is a critical grain size, for which the collisional lifetime is equal to the characteristic inward drift time scale. Therefore, the disk is collision-dominated at  $s > s_c$  and transport-dominated at  $s < s_c$ . In the “usual” disks, increasing  $\tau$  would sooner or later force  $s_c$  to reach the radiation pressure blowout limit  $s_{\text{blow}}$ . At that value of  $\tau$ , the entire disk becomes collision-dominated, since there is very little material in the disk of size  $s < s_{\text{blow}}$ . But not in the  $\varepsilon$  Eri disk! Here, the blowout limit does not exist (Fig. 4.2). Therefore, for any reasonable size distribution ( $q \geq 3$ ), the optical depth is dominated by small particles with  $s < s_c$ , and these are in the transport-dominated regime. That is why our simulation shows that the outer and intermediate regions of the  $\varepsilon$  Eri disk is dominated by grains roughly in the 0.05–1  $\mu\text{m}$  size range and, at those sizes, is nearly collisionless, despite  $\tau$  of  $\sim 10^{-4}$ . The same conclusion holds, of course, for the inner disk inside 10 AU. For this reason, we believe our model of the inner disk in the following section, which is obtained via collisionless numerical integration, is appropriate.

## 4.3 Dust in the inner region

### 4.3.1 Model

To investigate the behavior of dust in the inner region ( $r < 10$  AU) of the  $\varepsilon$  Eri debris disk and its interaction with the inner planet, we performed numerical integrations of grain trajectories. We used a Burlisch-Stoer algorithm (Press et al., 1992). Collisions are not considered in our inner disk model, because, as shown above, they play a minor role in the inner disk.

The dust grains were treated as massless particles, described only by their  $\beta$  ratio (or sizes) and their orbital elements: semimajor axis  $a$ , eccentricity  $e$ , inclination  $I$ , longitude of ascending node  $\Omega$ , argument of pericenter  $\omega$ , and mean anomaly  $\mathcal{M}$ .

In our simulations we examined the following grain sizes  $s_i$  ( $i = 1, \dots, 5$ ): 0.07, 0.11, 0.43, 0.84, and 2.42  $\mu\text{m}$ . These correspond to the  $\beta$  ratios of  $\beta_i = 0.1, 0.2, 0.2, 0.1,$  and 0.03, respectively (Fig. 4.2). Each  $s_i$  represents a size interval  $[\check{s}_i, \hat{s}_i]$ . The limits of these intervals are set to the middle of  $s_i$  and the adjacent sizes  $s_{i-1}$  and  $s_{i+1}$  (in logarithmic scale). Since, due to the low luminosity of the central star, the blowout grain size does not exist, the lower cut-off for the particle sizes was arbitrarily set to  $\check{s}_1 = 0.05$   $\mu\text{m}$ . Smaller particles are not expected to contribute significantly to the SED

at mid-IR and longer wavelengths. In addition, we expect that various erosive effects (e.g., plasma sputtering) and dynamical effects (e.g., the Lorentz force), which are not included in our model, would swiftly eliminate the tiniest grains from the system. Particles larger than  $\hat{s}_5 = 4 \mu\text{m}$  are not considered in these simulations, because they are absent in this region (cf. Fig. 4.4, right).

Since grains with the same  $\beta$  ratios experience the same force, it was enough to run three simulations ( $\beta_i = 0.2, 0.1,$  and  $0.03$ ) to cover all five grain sizes. We used 10 000 particles for each value of  $\beta$ . The grains were placed in orbits with initial eccentricities from 0 to 0.3 and an initial semimajor axis of  $20 \text{ AU}^9$ , assuming that they have passed the expected outer planet and are out of the range of its perturbation. The rather high initial eccentricities of up to 0.3 were taken, because these are expected to be increased by perturbations of the outer planet when passing through its orbit. The initial inclinations were uniformly distributed between  $0^\circ$  and  $10^\circ$ , respectively. The angular elements ( $\Omega, \omega, M$ ) were all uniformly distributed between  $0^\circ$  and  $360^\circ$ .

For the inner planet we used two different orbital configurations. These configurations fit the observations from Benedict et al. (2006) and Butler et al. (2006), in the following called cases *Be06* and *Bu06*, respectively. In both cases we set the planet’s semimajor axis to 3.4 AU and assumed its orbit to be coplanar with the disk’s mid-plane. Benedict et al. (2006) estimate the planet’s mass and eccentricity to  $m_{P_{\text{Be06}}} \sin i = 0.78 M_{\text{Jup}}$  and  $e_{P_{\text{Be06}}} = 0.7$ , while Butler et al. (2006) give  $m_{P_{\text{Bu06}}} \sin i = 1.06 M_{\text{Jup}}$  and  $e_{P_{\text{Bu06}}} = 0.25$ . The inclination of the system is estimated to  $30.1^\circ$  (Benedict et al., 2006). We also produced a simulation without an inner planet. A summary of the initial parameters for the simulations is given in Table 4.1.

### 4.3.2 Results

From our simulations we created a radial profile of the normal geometrical optical depth, assuming a steady-state distribution (Fig. 4.5). It illustrates that the inner planet intercepts a fraction of dust on its way inward by capturing the grains in MMRs and/or scattering those grains that pass the planetary orbit. This results in an inner gap around and inside the planet orbit. The gap is deeper for grains with smaller  $\beta$  ratios, because they drift inward more slowly, which increases the probability of a resonance trapping or a close encounter with the planet. Another conclusion from

<sup>9</sup>We use 20 AU instead of 10 AU because, if we placed the particles at 10 AU with eccentricities from 0 to 0.3, the initial distances would be distributed between 7 and 13 AU, causing an unwanted “boundary effect” of decreased optical depth in that distance range.

**Table 4.1:** Initial parameters of the inner disk simulations

star		
$M_\star$	$0.83M_\odot$	
$L_\star$	$0.32L_\odot$	
$\dot{M}_\star$	$30\dot{M}_\odot = 6 \times 10^{-13}M_\odot \text{ yr}^{-1}$	
$v_{sw}$	$400 \text{ km s}^{-1}$	
planet		
	Be06	Bu06
$m_P$	$1.78 \times 10^{-3}M_\star$	$2.44 \times 10^{-3}M_\star$
$a_P$	3.4 AU	3.4 AU
$e_P$	0.7	0.25
$I_P$	$0.0^\circ$	$0.0^\circ$
$\mathcal{M}_P, \Omega_P, \omega_P$	$0.0^\circ$	$0.0^\circ$
dust		
$\beta$	0.2, 0.1, 0.03, 0.01	
$a_0$	20 AU	
$e_0$	[0.0, 0.3]	
$I_0$	[ $0^\circ$ , $10^\circ$ ]	
$\mathcal{M}_0, \Omega_0, \omega_0$	[ $0^\circ$ , $360^\circ$ ]	

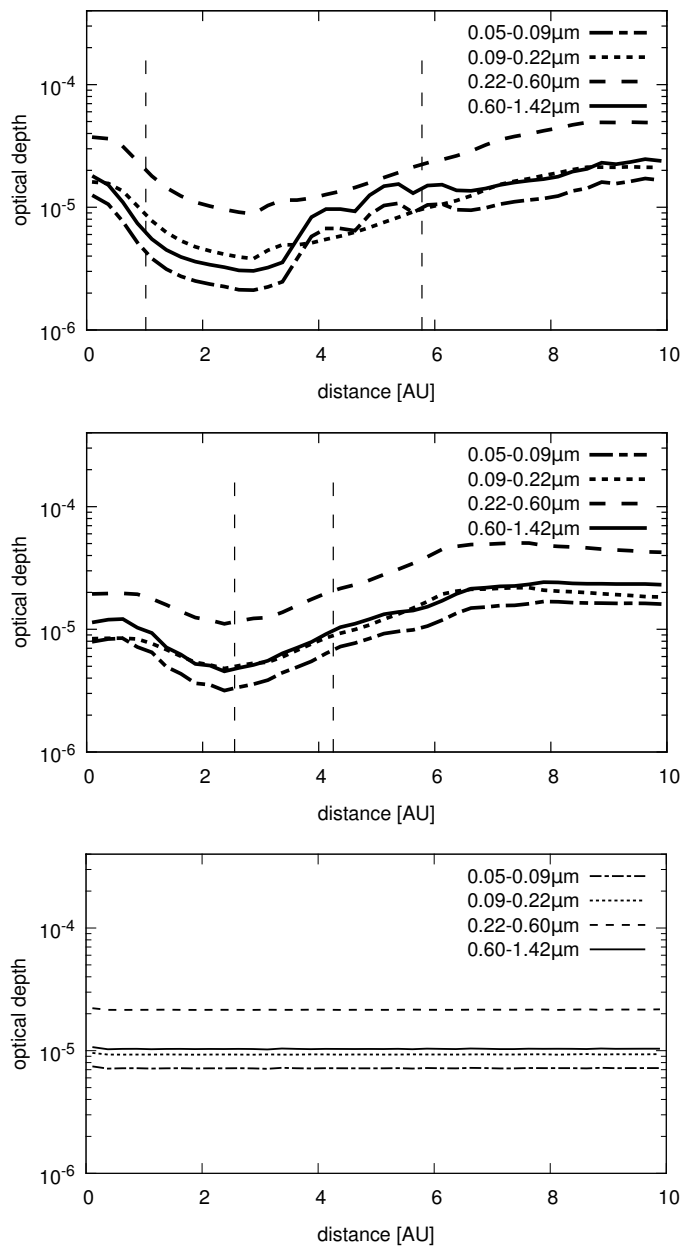
A range of  $[a, b]$  indicates that the parameters are equally distributed between  $a$  and  $b$ , and randomly chosen.

Fig. 4.5 is that the radial profiles in the cases Be06 and Bu06 do not differ much, although the eccentricities of planetary orbits are quite different.

## 4.4 Spectral energy distribution

### 4.4.1 SED from the outer and intermediate regions

Having calculated the distribution of dust particles with different  $\beta$  ratios in the  $\varepsilon$  Eridani system, we need to calculate the thermal emission of the dust for comparison with the observed SED. We start with the SED of the outer and intermediate region together. We have calculated it, using the output of the *ACE* runs described in Sect. 4.2. Specifically, coupled radial and size distributions of dust between 10 and 90 AU shown in Fig. 4.4 were used.



**Figure 4.5:** Radial profile of the normal geometrical optical depth produced by different grain size bins for the cases Be06 (*top*), Bu06 (*middle*), and without a planet (*bottom*). A radial bin width is  $\Delta r = 0.25$  AU. Vertical dashed lines show periastron and apastron of the planet orbit. A size distribution with a slope of  $q = 3.0$  and the dust mass of  $m_{\text{dust}} \approx 8.5 \times 10^{-8} M_{\oplus}$  (case Be06),  $9.9 \times 10^{-8} M_{\oplus}$  (case Bu06), and  $5.6 \times 10^{-8} M_{\oplus}$  (without a planet) were used for the vertical scaling of the curves.

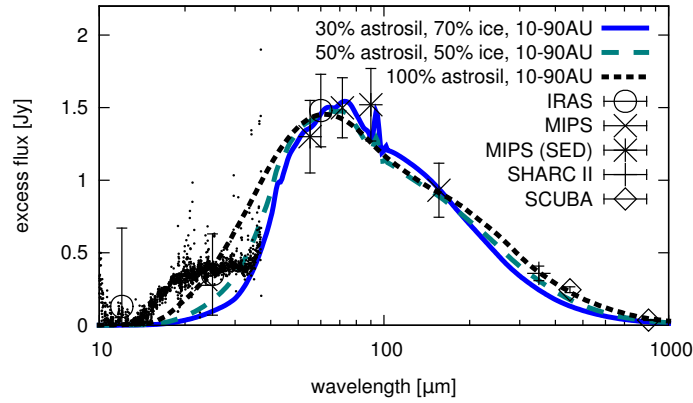


**Figure 4.6:** The SED from dust outside of 10 AU in the  $\varepsilon$  Eri dust disk. Symbols with error bars are data points and scattered dots are the IRS spectrum. Lines are model SEDs for different dust compositions: 100% astrosil (dotted), 50% ice and 50% astrosil (dashed), and 70% ice and 30% astrosil (solid).

The results are shown in Fig. 4.6. Overplotted are the data points, all taken from Fig. 7 of Backman et al. (2009); see also their Table 1. Clearly, the model with 100% astrosilicate contents is too “warm”. Notably, the SED starts to rise towards the main maximum too early (at  $\approx 25 \mu\text{m}$  instead of  $\approx 35 \mu\text{m}$ ), which is inconsistent with the “plateau” of the IRS spectrum. Including 50% ice improves the model, but the SED still rises too early. The best match of the data points is achieved with a 30% astrosil and 70% ice mixture, which will therefore be used in the rest of the paper. Still, even for that mixture, the main part of the SED (i.e., the combined contribution of the outer ring and the intermediate region) predicted by the collisional model is somewhat “warmer” than it should be. We discuss this slight discrepancy in Sect. 4.4.3.

#### 4.4.2 SED from the inner region

We now consider an SED coming from dust in the inner disk. The optical constants, density of the dust, and the stellar spectrum described in Sect. 4.1.3 have been used to calculate the “partial” SEDs from each grain size bin. To sum up the contributions from different bins, we assumed a power law  $m(s)ds \propto s^{3-q}ds$ . There are two parameters that allow us to adjust the resulting SED of the inner region to the IRS spectrum. One is the slope  $q$  that provides a “weighting” of relative contributions of different-sized grains into the resulting SED. In accord with our results in Sect. 4.2.2, we take  $q = 3$  and only consider grains with  $s \lesssim 2 \mu\text{m}$  (four lowest size bins). Another parameter should characterize the absolute amount of dust in the inner region. (This could be,



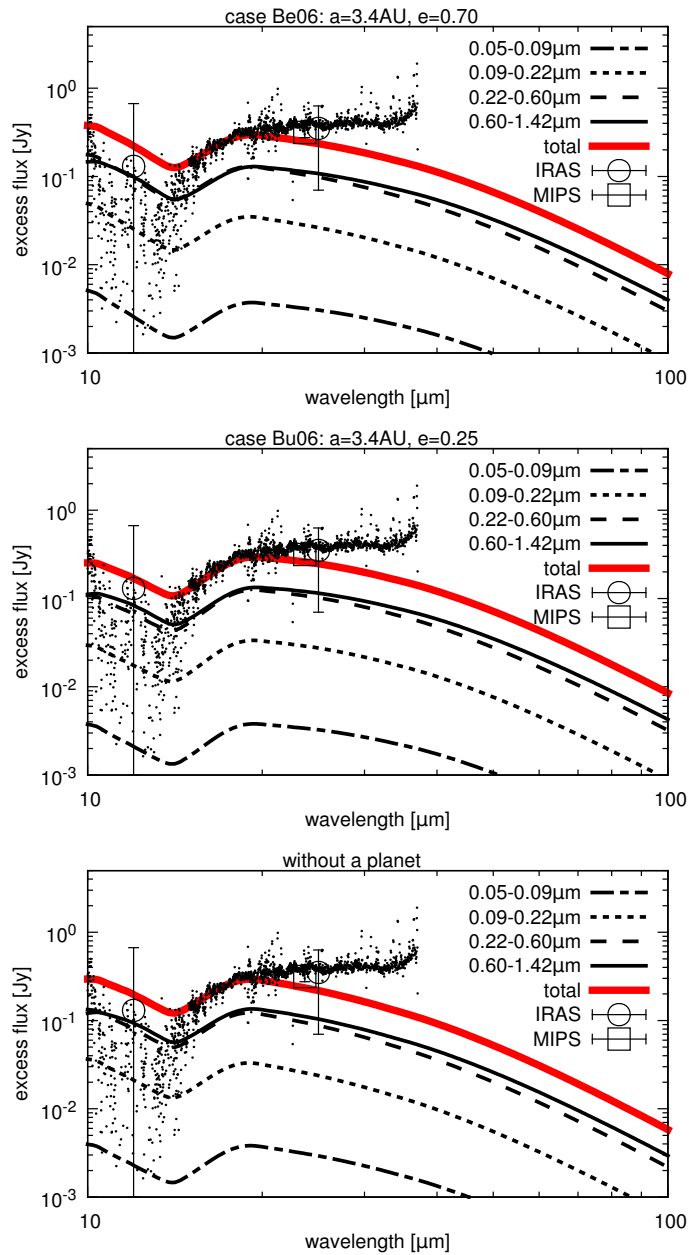


**Figure 4.7:** The observed Spitzer/IRS spectrum (Backman et al., 2009) (small dots) and the modeled SED of the inner region. *Top:* case Be06, *middle:* case Bu06, *bottom:* without a planet. Thin lines: contributions of the different size bins to the SED, thick line: the total emission from all sizes. The size distribution slope  $q$  and the dust mass  $m_{\text{dust}}$  are the same as in Fig. 4.5.

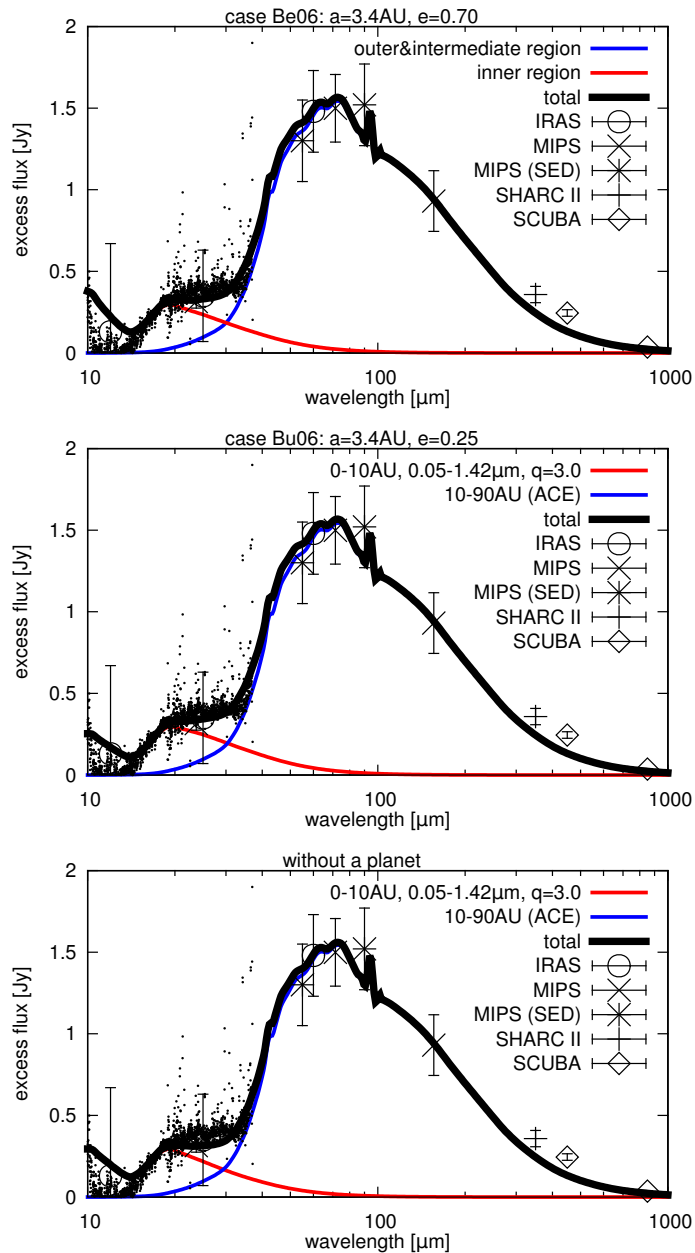
for instance, the total dust mass in the inner region.) This parameter would determine the overall height of the SED. We varied the dust mass until the resulting model SED fits the IRS spectrum best. The best results were achieved with the total dust mass in the inner region of  $m_{\text{dust}} \approx 8.5 \times 10^{-8} M_{\oplus}$  in the case Be06,  $9.9 \times 10^{-8} M_{\oplus}$  in the case Bu06, and  $5.6 \times 10^{-8} M_{\oplus}$  without a planet. The absolute height of optical depth profiles from various size bins shown in Fig. 4.5 corresponds to the same dust masses and the same slope  $q = 3.0$ .

Figure 4.7 shows the contribution of the different grain sizes to the SED and their total. we now use a logarithmic scale. Although the two planet orbits are quite different, the influence of the planet on the SED is rather minor, because the radial distributions of dust are similar in both cases.

A consistency check that we made was to compare the model predictions with the results of interferometric measurements with CHARA array in the  $K$ -band ( $2.2 \mu\text{m}$ ) (Di Folco et al., 2007). They set the upper limit of the fractional excess emission of the inner debris disk to  $6 \times 10^{-3}$  ( $3\sigma$  upper limit). With the photospheric flux of 120 Jy at  $\lambda = 2.2 \mu\text{m}$ , value includes both thermal emission and scattered light. The integrated surface brightness of the  $2.2 \mu\text{m}$  radial thermal emission profile, convolved with the CHARA transmission profile, generates a total excess of just 25.7 mJy, 14.5 mJy, and 15.4 mJy for the cases Be06, Bu06, and without an inner planet, respectively. Even if we took scattered light into account, which we estimate contributes  $\approx 3.4$  times more than the thermal emission at that wavelength, our model would be consistent with non-detection of dust with CHARA.

### 4.4.3 SED from the entire disk

We now assemble the SED produced by the entire disk. To this end, we summed up the SEDs of the inner region and of the region outside 10 AU presented in Figs. 4.6 and 4.7, respectively. Figure 4.8 shows the complete SED. It is in a reasonable, although not a perfect, agreement with the observations. In particular, the maximum of the modeled SED, while reproducing the data points within their error bars, appears to lie at a slightly shorter wavelength than the one suggested by the data points. A likely reason for this discrepancy is that our collisional simulation does not take into account elimination of particles in the size range from  $\sim 1$  to  $\sim 100 \mu\text{m}$  by the alleged outer planet, as explained above. Excluding these particles from the intermediate region 10–55 AU would reduce emission in the 35–70  $\mu\text{m}$  wavelength range, shifting the maximum of the SED to a longer wavelength. In addition, the main part of the



**Figure 4.8:** The entire SED of the  $\epsilon$  Eri dust disk. Symbols with error bars are data points, small dots is the IRS spectrum. Thick line in each panel is the excess emission predicted by the models, and thin lines show contributions from the inner region ( $< 10$  AU) and the intermediate+outer disk. Three panels are for the planet configurations Be06 (*top*), Bu06 (*middle*), and without a planet (*bottom*).

SED can be made “colder” by varying diverse parameters of the collisional simulation, many of which are not at all or are poorly constrained. These include the eccentricity distribution of planetesimals, the opening angle of the planetesimal disk, as well as the mechanical strength of solids. Such a search for the best fit would, however, be very demanding computationally. We deem the fit presented in Fig. 4.8 sufficiently good to demonstrate that our scenario, in which inner warm dust is produced in the outer ring, is feasible.

#### 4.4.4 Connecting outer and inner regions

To make sure that the amount of dust required to reproduce the IRS spectrum is consistent with the amount of dust that could be supplied to the inner disk from the outer parent belt, we now make an important consistency check. From calculations of the dust production in the outer ring and its transport through the intermediate region, we know the optical depth at 10 AU. Figure 4.4 (right) suggests that the optical depth per size decade, created by grains with sizes of 0.07, 0.11, 0.43, and 0.84  $\mu\text{m}$ , is about  $(1-2)\times 10^{-4}$ . These values have to be compared with optical depths, sufficient to reproduce the IRS spectrum. From Fig. 4.5 outside the planetary region we read out the values  $(2-5)\times 10^{-5}$  for the four lowest size bins (which are centered on the same four grain sizes). Taking into account the actual width of the four lowest size bins used in the modeling of the inner system, which is  $\approx 0.4$  dex, we would need an optical depth per size decade of  $(5-10)\times 10^{-5}$ . Thus the optical depth that is supplied by grains transported from outside matches the optical depth required to account for the IRS spectrum within a factor of two. Considering sublimation of 70% of the icy material at around 10 AU, the optical depths are in nearly perfect agreement.

### 4.5 Surface brightness profiles

The model developed in this paper was designed to explain the Spitzer/IRS spectrum of the system. Besides this, we have made sure that it reproduces the entire SED probed with many instruments at the far-IR and sub-mm wavelengths. We now provide a comparison with other measurements that we have not considered before.

The most important information comes from spatially resolved images. Spitzer/MIPS observations yielded brightness profiles in all three wavelength bands centered on 24,

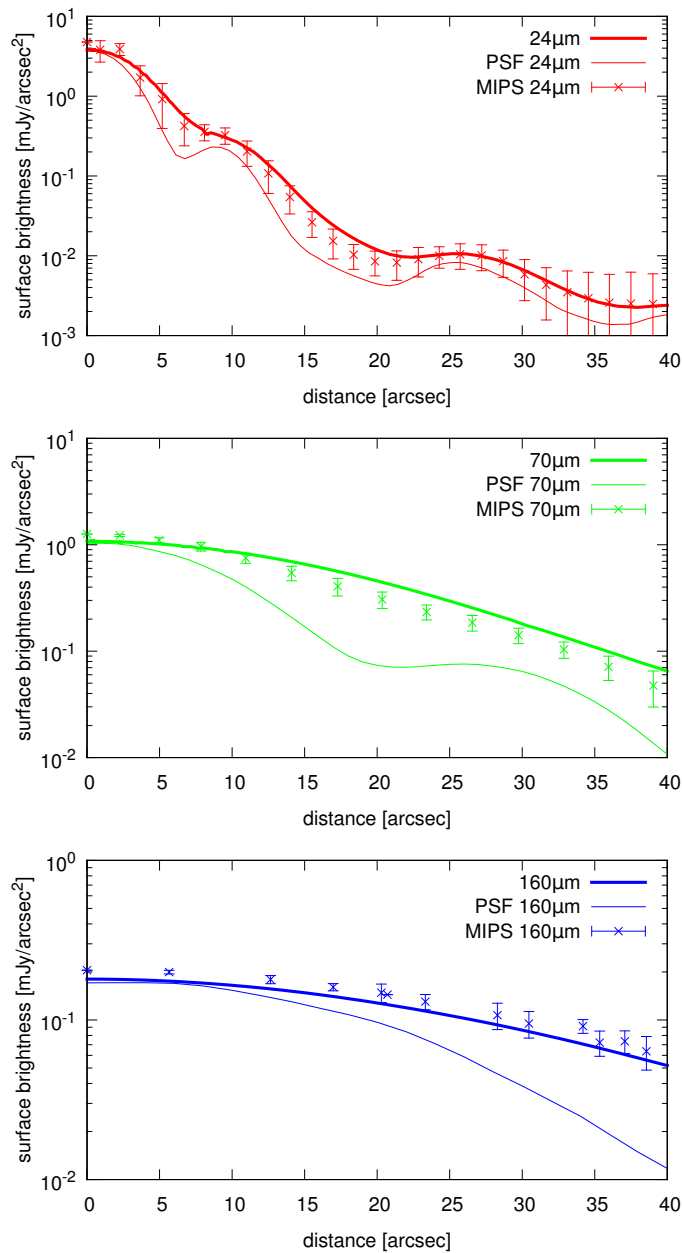


**Figure 4.9:** Azimuthally averaged surface brightness profiles of the  $\varepsilon$  Eri dust disk (case Be06) at three Spitzer/MIPS wavelengths: 24  $\mu\text{m}$  (*top*), 70  $\mu\text{m}$  (*middle*), and 160  $\mu\text{m}$  (*bottom*). Points with error bars: star-subtracted MIPS data (Fig. 6 of Backman et al., 2009). Solid lines: modeled profiles after convolution with the PSFs. Thin solid lines: the instrumental PSF.

70, and 160  $\mu\text{m}$  (Backman et al., 2009). We calculated the brightness profiles of thermal emission with our model. In doing so, we included both the outer+intermediate disk and the inner one. The resulting brightness profiles were convolved with the instrumental PSF (see Sect. 2 in Müller et al., 2010, for the algorithm used) and compared them with observed profiles.

The results are presented in Fig. 4.9. We only show case Be06, since the profiles in case Bu06 and without a planet are very similar. At all three wavelengths, the modeled brightness monotonically increases toward the star, as does the observed brightness. Both the slopes and the absolute brightness level are in good agreement with observations. The only exception is the modeled 70  $\mu\text{m}$  profile (Fig. 4.9 middle). It is flatter than the observed one, predicting the brightness inside 30 AU correctly but overestimating the emission in most of the intermediate and the parent ring regions by a factor of two. The reasons for this deviation are probably the same as those discussed in Sect. 4.4.3. First, if a presumed outer planet at  $\approx 40$  AU efficiently eliminates particles in a size range from several to several tens of micrometers (which is not taken into account in our ACE simulations), this will decrease the 70  $\mu\text{m}$  brightness in the intermediate region. Second, it should be possible to slightly decrease the 70  $\mu\text{m}$  emission in the parent ring region by varying poorly known parameters in the collisional simulation.

We also checked the radial brightness profile at 850  $\mu\text{m}$  and compared it with JCMT/SCUBA observations (Greaves et al., 1998, 2005). After convolution with a Gaussian PSF of  $\sigma = 5''$ , the resulting profile is consistent with Greaves et al. (2005, their Fig. 2), showing a broad ring around  $\approx 60$  AU and a resolved central cavity.

## 4.6 Conclusions

In this paper we show that in the nearby system  $\varepsilon$  Eridani the Spitzer/IRS excess emission at  $\lambda \sim 15\text{--}30$   $\mu\text{m}$  can be caused by dust that is produced in the known outer dust ring and that streams inward due to interaction with strong stellar winds.

By running a collisional code, we simulated the dust production in the outer ring between 55 AU and 90 AU with a dust mass of  $10^{-3}M_{\oplus}$  and the subsequent transport of the dust inward to 10 AU. We then employed single-particle numerical integrations to simulate the dust transport further inward through the orbit of the known inner planet. The dust in the inner region was found to consist of grains smaller than  $\approx 2$   $\mu\text{m}$ , and the dust mass inside 10 AU was estimated to be  $(6\text{--}10)\times 10^{-8}M_{\oplus}$ . Combining the

results of the collisional simulations outside 10 AU and numerical integrations inside that distance, we calculated the overall SED and radial brightness profiles. This SED is in a reasonable agreement with the available observational data, and it correctly reproduces the shape and the height of the Spitzer/IRS spectrum. Likewise, the brightness profiles are consistent with the Spitzer/MIPS data.

The best results are obtained with an ice-silicate composition (Laor & Draine, 1993; Li & Greenberg, 1998) of dust outside the ice sublimation distance of  $\approx 10$  AU, and an inner disk of non-volatile silicate grains inside that distance.

With the aid of the modeled spectra and brightness profiles, it is not possible to distinguish between the different orbital solutions for the inner, radial velocity planet proposed by Benedict et al. (2006) or Butler et al. (2006). Although the planetary orbits they inferred are quite different, both setups yield quite similar radial profiles of dust, the SEDs, and the brightness profiles.

Various kinds of new data on the  $\varepsilon$  Eridani system are expected soon. Data from ALMA, JCMT/SCUBA2 (J. Greaves, pers. comm.), Herschel/PACS, and /SPIRE should shed light on the cold dust. This includes the structure of the outer “Kuiper belt” and the intermediate region of the disk between 10 and 55 AU. Further more, there is hope to better probe the inner warm dust directly, with instruments such as the Mid InfraRed Instrument (MIRI) aboard the upcoming James Web Space Telescope (JWST). Likewise, there is an ongoing effort to find outer planets in the system by direct imaging (Itoh et al., 2006; Marengo et al., 2006; Janson et al., 2007, 2008; Marengo et al., 2009).

# Chapter 5

## Debris dust in systems with transiting planets

*This chapter is based on the paper “Debris disc candidates in systems with transiting planets” (Krivov et al., 2011). I made major contributions to the catalog search and data processing. Other parts of this study were done in collaboration with Alexander Krivov, Simone Fiedler, Torsten Löhne, and Ralph Neuhäuser.*

Many debris disks have been found in systems with known radial velocity (RV) planets (e.g., Beichman et al., 2005b; Moro-Martín et al., 2007; Trilling et al., 2008; Bryden et al., 2009; Kóspál et al., 2009), and a few systems with debris disks and directly imaged planetary candidates are known (Kalas et al., 2008; Marois et al., 2008; Lagrange et al., 2010). Until the beginning of 2012, no debris dust had been found in systems with planets detected by transits (Ribas et al., 2012).

With the release of the *WISE Preliminary Release Source Catalog* in April 2011 we saw a promising opportunity to find debris dust in systems with transiting planets. The motivation is obvious. A successful search would extend the list of known “full” planetary systems that harbor both planets and asteroid or Kuiper belt analogs. Furthermore, it is the transit technique that allows determination of many planetary parameters, such as masses, radii and densities, and can provide insights into properties of planetary atmospheres and interiors. Finally, transiting planets are on the average even closer to their parent stars than those discovered by the RV method, which might be related to somewhat different formation circumstances. Therefore, systems with transiting planets are of special interest. Detection of planetesimal belts, which are leftovers of planet formation, could help constraining various formation and evolution scenarios of those planets. And conversely, precise knowledge of planetary parameters could put constraints on the properties of the planetesimal belts. For instance, accurate masses and orbits of planets would result in tighter constraints on dynamical stability zones and thus location of planetesimal belts.

While the two previous chapters are detailed studies of the architecture of known full planetary systems, we want to present here our attempt to find additional systems of this kind. The chapter describes how we found and identified candidates for excess



emission in systems with transiting planets. Section 5.1 describes the inquiry for observational data of systems with transiting planets and the preselection of excess candidates. In Sect. 5.2 the more detailed analysis of the candidates is described. In Sect. 5.3 we try to constrain the mass and location of the presumed dust belts on the basis of the observational data. Sect. 5.4 closes with our conclusions and a discussion of our findings.

## 5.1 Search for dust

In May 2011, we took a list of 93 systems, known at that time, from [exoplanets.org](http://exoplanets.org) (Wright et al., 2011b). This list was compared with target lists of several IR missions: *IRAS* (Neugebauer et al., 1984), *ISO* (Kessler et al., 1996), *Spitzer* (Werner et al., 2004), *AKARI* (Murakami et al., 2007), and *WISE* (Wright et al., 2010), which we accessed through IRSA, the NASA/IPAC Infrared Science Archive at <http://irsa.ipac.caltech.edu>.

### 5.1.1 IRAS, ISO, Spitzer, and AKARI

Nearly all of the transit planet host stars are located at hundreds of parsecs from the Sun and are thus faint. Accordingly, we had not expected to find them in older, and shallower, *IRAS* and *ISO* catalogs and indeed, have not found any. For example, of 93 systems with transiting planets listed in [exoplanets.org](http://exoplanets.org), only five are within 50 pc. These are GJ 436, GJ 1214, HAT-P-11, HD 189733, and HD 209458. None of them appears in *IRAS*, *ISO*, and *WISE* catalogs. Three of them, GJ 436, HD 189733, and HD 209458, have been probed by *Spitzer*/MIPS at 24 and 70  $\mu\text{m}$ , yielding no excess detection (Bryden et al., 2009). We found an entry for the latter star in the *AKARI* catalog, reporting a detection at 9  $\mu\text{m}$ , which is consistent with the photospheric level. Note that HD 209458 b was the first exoplanet found to transit the disk of its parent star (Charbonneau et al., 2000).

We also identified two more distant transit planet host stars that were observed by *Spitzer*/MIPS: HD 80606 and HD 149026. No excess at 24 and 70  $\mu\text{m}$  was found for HD 189733 (Bryden et al., 2009). For HD 80606, the result is ambiguous due to pointing problems (Carpenter et al., 2008). *AKARI* has observed one more transit host star, too: HD 149026. It has been detected at 9  $\mu\text{m}$ , showing no excess.

### 5.1.2 WISE

The search in the *WISE* Preliminary Source Catalog was more successful. This is perhaps not a surprise, given the broad sky coverage (57%) of the catalog, an excellent sensitivity of the instrument and thus a huge number of sources observed (257 million). The *WISE* catalog provides measured magnitudes in four bands  $W_i$  ( $i = 1, \dots, 4$ ), which are centered at 3.4, 4.6, 12, and 22  $\mu\text{m}$ . Of 93 systems with transiting planet candidates listed in exoplanets.org, we found 53 with entries in the *WISE* catalog. One source – CoRoT-14 – is irretrievably contaminated by ghost images in bands  $W_3$  and  $W_4$  and was excluded from further analysis.

To select possible IR excess candidates amongst the remaining 52 sources, we first converted the observed magnitudes in the four bands into spectral flux densities. Since no excesses are expected in bands  $W_1$  and  $W_2$ , we made simple photospheric predictions for  $W_3$  and  $W_4$  from the  $W_1$  and  $W_2$  fluxes. At first, we roughly corrected the  $W_1$  and  $W_2$  fluxes for an expected average level of interstellar extinction. Considering that systems in our sample are typically at a few hundred parsecs, we set  $A_V$  to 0.5<sup>m</sup>, which translates to  $A(W_1) = 0.029^m$  and  $A(W_2) = 0.012^m$  (Rieke & Lebofsky, 1985). We then fitted the corrected  $W_1$  and  $W_2$  fluxes with a power law  $F_{\text{phot}} = F_{\text{phot}}^0 \lambda^{-b}$ , with  $F_{\text{phot}}^0$  and  $b$  being the fitting parameters. Subtracting the expected photospheric flux from the observed one, we derived the “excess flux”  $F \equiv F_{\text{obs}} - F_{\text{phot}}$  in bands  $W_3$  and  $W_4$ . The net uncertainty of a photometric point for a given star in the band  $W_3$  or  $W_4$  was computed as  $\sigma = \sqrt{\sigma_{\text{phot}}^2 + \sigma_{\text{obs}}^2 + \sigma_{\text{cal}}^2}$ . Here,  $\sigma_{\text{phot}}$  is the photospheric uncertainty, which we estimated from the combined uncertainties of the measurements in bands  $W_1$  and  $W_2$ , given in the *WISE* catalog. Next,  $\sigma_{\text{obs}}$  is the measurement uncertainty in the bands of interest,  $W_3$  and  $W_4$ , also taken from the *WISE* catalog. Finally,  $\sigma_{\text{cal}}$  is the absolute calibration uncertainty of the *WISE* instrument (2.4, 2.8, 4.5, and 5.7% for bands from  $W_1$  to  $W_4$ ). The significance of an excess can now be defined as  $\chi = F/\sigma$ .

The distributions of  $\chi$ -values in the sample are shown in Fig. 5.1 for bands  $W_3$  (top) and  $W_4$  (bottom). The  $W_3$  histogram appears close to a Gaussian, without any obvious outliers. However, the  $W_4$  histogram uncovers a bin containing four systems with  $\chi > 1.75\sigma$ , clearly separated from the Gaussian bulk. These are XO-5, HAT-P-5, TrES-2, and CoRoT-8. These four excess candidates will be checked in Sect. 5.2 more thoroughly, including an in-depth photospheric analysis and more accurate uncertainty estimates.

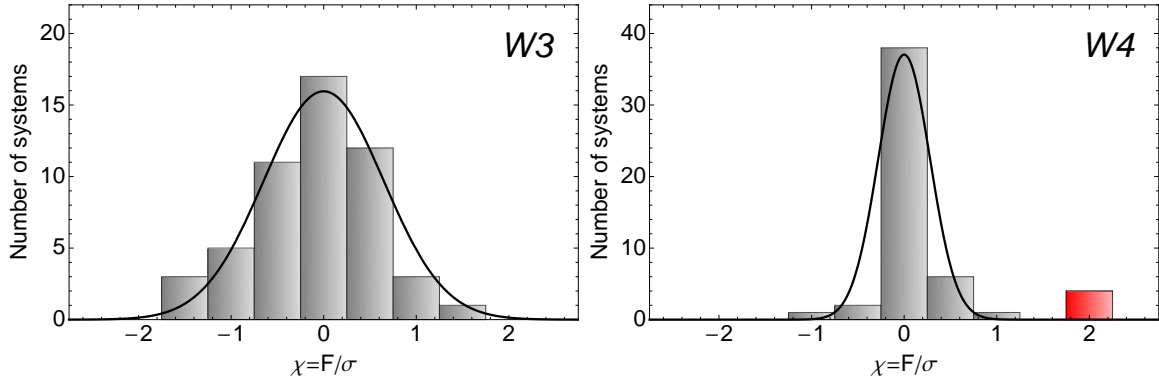


**Figure 5.1:** Histogram of  $\chi = F/\sigma$  values at 12  $\mu\text{m}$  (left) and 22  $\mu\text{m}$  (right) for systems with transiting planets. For comparison, overplotted are closest Gaussian distributions, which have variances of 0.65 (left) and 0.28 (right). That these variances are smaller than unity may suggest that the procedure of calculating  $\sigma$ , described in the text, is too cautious and overestimates the actual noise. The rightmost bin in the  $W_4$  histogram shown in red contains four excess candidates. We checked that slight modifications to the photospheric extrapolation procedure or extinction correction (i.e., using  $A_V$  values between 0.0<sup>m</sup> and 1.0<sup>m</sup>) slightly skew and shift the  $W_3$  histogram, but preserve the  $W_4$  one, including the bin with the four outliers.

## 5.2 Analysis of excess candidates

For the excess candidates, we have collected stellar data (Tab. 5.1) as well as optical and near-IR photometry. In the visual, we used the USNO-B1.0 Catalog (Monet et al., 2003), the Guide Star Catalog, Vers. 2.3.2 (Lasker et al., 2008), and the All-Sky Compiled Catalogue of 2.5 Million Stars (Kharchenko & Roeser, 2009). The near-IR data stem from the 2MASS All-Sky Catalog of Point Sources (Skrutskie et al., 2006). For transforming the  $B$ ,  $V$ ,  $R$ ,  $I$  magnitudes into units of flux density [Jy], we used the Johnson calibration system and for the 2MASS  $J$ ,  $H$ ,  $K_s$  bands the Cohen et al. (2003) calibrations.

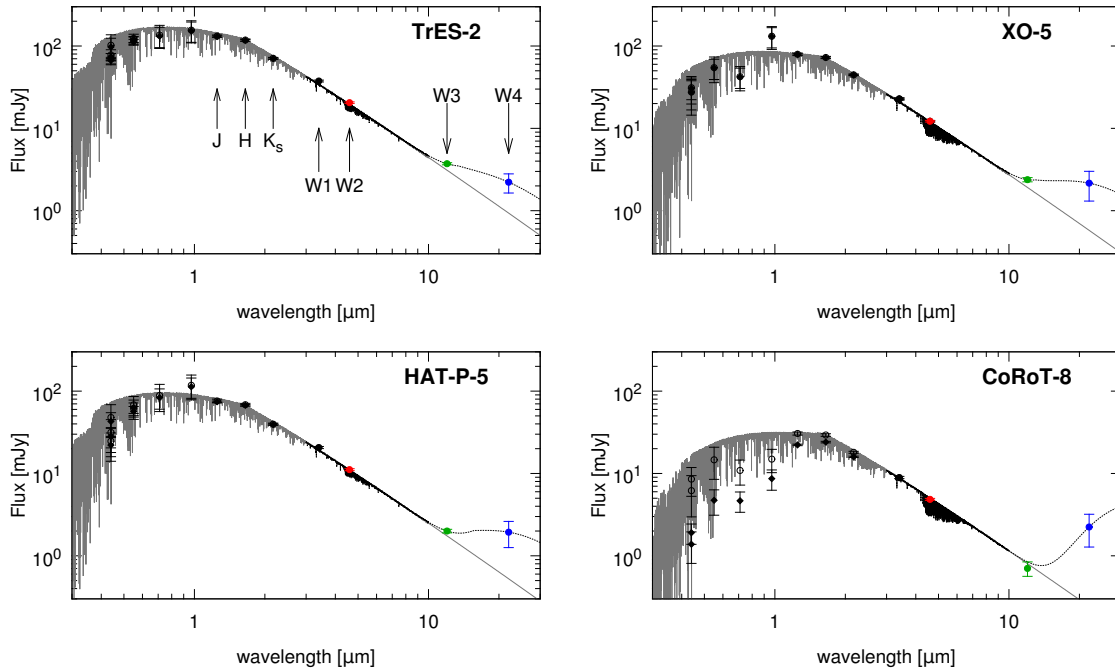
At the first step, this photometry was corrected for interstellar extinction. Since for distances considered here the latter is known to correlate with distance only weakly, we used color indices from Kenyon & Hartmann (1995) and the spectral type as given in Tab. 5.1 to derive the best-fit  $A_V$  from multiple colors and then  $A_\lambda/A_V$  ratios of Rieke & Lebofsky (1985) to compute extinction for the wavelengths of all photometry points. The derived  $A_V$  values are within 0.1<sup>m</sup> for non-CoRoT stars, but as large as  $1.3^m \pm 0.2^m$  for CoRoT-8. The extinction in  $W_3$  and  $W_4$  bands does not exceed 0.04<sup>m</sup> (CoRoT-8).

**Table 5.1:** Stellar parameters given in literature, as well as our best-fit values and the deviation from starting values.

Star		XO-5	HAT-P-5	TrES-2	CoRoT-8
References		[1]	[2]	[3]	[4]
$V_{\text{mag}}$	[mag]	12.1	12.0	11.4	14.8
$d$	[pc]	$260 \pm 12$	$340 \pm 30$	230	$380 \pm 30$
Spectral type		late G	early G	G0 V	K1 V
$M_{\star}$	$[M_{\odot}]$	$0.88 \pm 0.03$	$1.16 \pm 0.06$	$1.08 \pm 0.11$	$0.88 \pm 0.04$
$T_{\text{eff}}$	[K]	$5370 \pm 70$	$5960 \pm 100$	$5960 \pm 100$	$5080 \pm 80$
$R_{\star}$	$[R_{\odot}]$	$1.08 \pm 0.04$	$1.17 \pm 0.05$	$1.00^{+0.06}_{-0.04}$	$0.77 \pm 0.02$
best-fit					
$d$	[pc]	$286 (+10\%)$	$340 (\pm 0\%)$	$219 (-5\%)$	$304 (-20\%)$
$T_{\text{eff}}$	[K]	$5800 (+8\%)$	$6400 (+7\%)$	$6400(+7\%)$	$5400 (+6\%)$

**References:**

[1] Pál et al. (2009), [2] Bakos et al. (2007), [3] O’Donovan et al. (2006), [4] Bordé et al. (2010).

**Figure 5.2:** Spectral energy distributions (SEDs) of four selected stars. Grey solid line: predicted extinction-corrected photosphere. Diamonds and open circles: visual and near-IR photometry data before and after correction for interstellar extinction, respectively. Filled circles: extinction-corrected *WISE* data (errors bars are  $\sigma_{\text{obs}}$ ). Black dashed line: modified BB model.

**Table 5.2:** Fluxes, uncertainties, and significance of excesses for all four candidates.

System	Band	$F_{\text{obs}}^*$ [mJy]	$F_{\text{obs}}$ [mJy]	$F_{\text{phot}}$ [mJy]	$F$ [mJy]	$\sigma_{\text{phot}}$	$\sigma_{\text{obs}}$	$\sigma_{\text{cal}}$	$\sigma$	$\chi$	$\chi_{\text{joint}}$
TrES-2	W3	3.71	3.72	3.10	0.62	0.20	0.11	0.17	0.29	2.17	3.28
	W4	2.22	2.22	0.93	1.29	0.12	0.58	0.13	0.61	2.12	
XO-5	W3	2.38	2.38	1.92	0.47	0.09	0.14	0.11	0.20	2.35	3.23
	W4	2.16	2.16	0.58	1.58	0.08	0.85	0.12	0.86	1.84	
HAT-P-5	W3	1.99	2.00	1.74	0.26	0.09	0.10	0.09	0.16	1.58	2.82
	W4	1.93	1.94	0.53	1.41	0.09	0.68	0.11	0.70	2.03	
CoRoT-8	W4	2.17	2.24	0.24	2.00	0.09	0.96	0.13	0.97	2.05	

*Columns:* Observed flux  $F_{\text{obs}}^*$ , observed flux after correction for extinction  $F_{\text{obs}}$ , expected photospheric flux  $F_{\text{phot}}$ , excess flux  $F$ ; uncertainty of photospheric flux  $\sigma_{\text{phot}}$ , observation uncertainty  $\sigma_{\text{obs}}$ , absolute calibration uncertainty  $\sigma_{\text{cal}}$ , net uncertainty of the excess flux  $\sigma$ , excess significance level in a single band  $\chi$ ; joint ( $W_3$  and  $W_4$ ) significance level  $\chi_{\text{joint}}$ .

At the second step, we performed a minimum  $\chi^2$  fitting of the extinction-corrected stellar photospheric fluxes by NextGen models (Hauschildt et al., 1999), only to data points between  $1\ \mu\text{m}$  and  $5\ \mu\text{m}$ . This is because those wavelengths are short enough not to expect any excess emission, but are long enough for interstellar extinction to be small. The interval from  $1\ \mu\text{m}$  to  $5\ \mu\text{m}$  includes three 2MASS points ( $J$ ,  $H$ ,  $K_s$ ) and two *WISE* points ( $3.4$  and  $4.6\ \mu\text{m}$ ), all of which were given equal weights. Since the surface gravity of our stars ( $\log g$  between 4.33 and 4.61) and their metallicity ( $[\text{Fe}/\text{H}]$  from  $-0.2$  to  $+0.31$ ) deviate from the solar values only slightly (see Tab. 5.1 for references), we assumed a  $\log g$  of 4.5 and the solar metallicity. Using  $T_{\text{eff}}$  and  $d$  listed in Tab. 5.1 as starting values, we varied the temperature by  $\pm 400\ \text{K}$  in 200 K steps and the distance to the star within  $\pm 30\%$  in 5% steps to derive best-fit values of these two parameters. This yielded deviations from the starting values of up to 8% in  $T_{\text{eff}}$  and up to 20% in  $d$  (Tab. 5.1). The results with the photometric points overplotted are shown in Fig. 5.2. Importantly, TrES-2 and XO-5 and possibly also HAT-P-5 reveal small excesses in band  $W_3$  as well, which were not seen in Fig. 5.1 (top).

We now come to a detailed analysis of the fluxes and their uncertainties. Denote the observed flux by  $F_{\text{obs}}^*$ , the extinction-corrected one by  $F_{\text{obs}}$ , the predicted extinction-corrected photospheric flux by  $F_{\text{phot}}$ , and the excess flux by  $F \equiv F_{\text{obs}} - F_{\text{phot}}$ . As in Sect. 5.1, the net uncertainty of  $F$  for a given star in band  $W_3$  or  $W_4$  is computed as  $\sigma = \sqrt{\sigma_{\text{phot}}^2 + \sigma_{\text{obs}}^2 + \sigma_{\text{cal}}^2}$ . The measurement uncertainty  $\sigma_{\text{obs}}$  and the calibration un-

certainty  $\sigma_{\text{cal}}$  are included as described before. However, the photospheric uncertainty  $\sigma_{\text{phot}}$  is now a by-product of the fitting procedure. It is dominated by a scatter in  $J$ ,  $H$ ,  $K_s$ ,  $W_1$ , and  $W_2$  points (the error bars of the points themselves as well as the uncertainty of the extinction correction are much smaller). All the quantities above, and the resulting excess significance  $\chi = F/\sigma$ , are listed in Tab. 5.2. Nearly all excesses are at  $\approx 2\sigma$  level, whereas usually a  $3\sigma$  excess is treated as a significant detection. However, in the cases of TrES-2, XO-5, and HAT-P-5, the excess is detected in two bands. The combined multi-band ( $W_3$  and  $W_4$ ) Gaussian statistics suggests the significance level for these sources of 3.28, 3.23, and 2.82, respectively. This finally selects two systems, TrES-2 and XO-5, as  $> 3\sigma$ -significant and thus the best excess candidates. The binomial probability that one of these two detections is false is only 6.4%, and the probability that both are false is as low as 0.2%. The expected number of false detections at  $> 3\sigma$  level is just 0.14; we detected two excesses at that level.

### 5.3 Presumed dust belts

In what follows, we estimate the parameters of dust that would produce the excesses in the best candidate systems, TrES-2 and XO-5, provided these are real. Since the excesses are of low significance and the data are limited to two photometry points, a detailed SED modeling based on various assumptions about the size distribution and composition of dust is not warranted. Instead, we used a pure blackbody (BB) and a modified BB emission model. In the latter case, we assumed a single grain size  $s_0$  and the opacity index of  $-2$  beyond  $\lambda = 2\pi s_0$ . The effective grain size  $s_0$  was chosen in the following way. Assuming a power-law size distribution with the index  $q = 3.5$  and the lower cutoff radius  $s_{\text{min}}$  of twice the radiation pressure blowout limit  $s_{\text{blow}}$  (see. e.g., Krivov et al., 2006; Thébault & Augereau, 2007), we have equated the emission of a disk of grains having such a size distribution and the emission of a disk composed of equal-sized grains of radius  $s_0$ :

$$\begin{aligned} & \int_{s_{\text{min}}}^{\infty} Q_{\text{abs}}(\lambda, s) B_{\nu}(\lambda, T_{\text{d}}(r_{\text{d}}, s)) s^{2-q} ds \\ &= Q_{\text{abs}}(\lambda, s_0) B_{\nu}(\lambda, T_{\text{d}}(r_{\text{d}}, s_0)) s_0^2 \int_{s_{\text{min}}}^{\infty} s^{-q} ds, \end{aligned} \quad (5.1)$$

where  $r_{\text{d}}$  is the distance from the star,  $\lambda$  is the wavelength where excess emission is observed,  $B_{\nu}$  is the Planck intensity,  $Q_{\text{abs}}(\lambda, s)$  is the grain absorption efficiency, and  $T_{\text{d}}$  is the grain temperature. In calculating  $s_{\text{blow}}$ , we assumed the unit radiation

pressure efficiency and the bulk density of  $3 \text{ g cm}^{-3}$  and took the stellar parameters from Tab. 5.1. Equation (5.1) was solved for  $s_0$ .

We then sought pure BB and modified BB curves that reproduce  $F(12 \mu\text{m})$  and  $F(22 \mu\text{m})$ . This has yielded estimates of the temperature, location, mass, and the fractional luminosity of the emitting dust (Tab. 5.3). When deriving the dust mass, we converted the mass of grains with  $s = s_0$  into the mass of grains with  $s < 1 \text{ mm}$ , assuming a power-law size distribution with a slope of 3.5. Both stars, TrES-2 and XO-5, appear to have rings with radii of 6–8 AU and fractional luminosities in the range  $(3\text{--}6) \times 10^{-4}$ . We stress that all these inferred values are quite uncertain, because they rest on scarce photometric data and their derivation involves a number of simplifying assumptions and poorly known parameters.

**Table 5.3:** Dust parameters inferred from the observed excesses and parameters of transiting planets.

System	Blackbody		Modified blackbody						Planet		
	$T_d$ [K]	$r_d$ [AU]	$s_{\text{blow}}$ [ $\mu\text{m}$ ]	$s_0$ [ $\mu\text{m}$ ]	$T_d$ [K]	$r_d$ [AU]	$m_d$ [ $M_\oplus$ ]	$f_d$ $10^{-4}$	$a_{\text{pl}}$ [AU]	$e_{\text{pl}}$	$m_{\text{pl}}$ [ $M_{\text{Jup}}$ ]
TrES-2	218	1.7	0.4	2.1	155	5.8	$5 \times 10^{-5}$	3	0.037	0	1.28
XO-5	181	2.2	0.4	2.0	133	8.0	$1 \times 10^{-4}$	6	0.051	0.049	1.06

*Note:* Planetary parameters are taken from the papers listed in Tab. 5.1.

## 5.4 Conclusions and discussion

We found that 52 systems with transiting planets have been observed by *WISE*. Our analysis of the data given in the *preliminary* WISE catalog from April 2011, two of them showed a warm two-band (12 and 22  $\mu\text{m}$ ) IR excesses at  $\chi_{\text{joint}} > 3$ . These results have not been confirmed by an analysis from Ribas et al. (2012). On the one hand, they do not find a significant excess in W3 for all of our four candidates, and no excess in W4 for XO-5 since they fit a lower effective temperature for the stellar model atmosphere and a more stringent cutoff  $\chi_\lambda > 2$ . On the other hand, they find an excess in W4 for CoRoT-8, HAT-P-5, and TrES-2 but a closer look onto the WISE images reveals, that the photocenter is offset with respect to shorter wavelengths. Thus, the flux given in the catalog comes from another source contaminating the target. In the *final* release of the *WISE All-Sky Source Catalog* now all four systems are flagged in

W4 as 95% confidence upper limit, and also CoRoT-8 is flagged in W3 as an upper limit detection.

In their analysis of known transiting systems from the literature, and 997 transiting candidates from the *Kepler* mission Ribas et al. (2012) found 13 other candidates with excesses at 12 and/or 22  $\mu\text{m}$ . This would nearly double the number of systems with known warm excess around main sequence stars, if their candidates were confirmed. Kennedy & Wyatt (2012) note, that the findings of Ribas et al. (2012) also have to be taken with caution, since for an excess significance threshold of  $2\sigma$ , statistically 2.3% of all systems could show an excess due to uncertainties. Therefore, of the 468 systems, Ribas et al. (2012) considered, statistically 11 may be false-positives.

Kennedy & Wyatt (2012) found in their own analysis of all Kepler targets – consisting not only transit systems – an occurrence rate of warm dust emission of about four per cent. But they argue that these excesses are caused by a contamination of high background. Finally, they present one significant candidate from the Kepler field with a one per cent chance of being contaminated by a background galaxy. Altogether they found “no evidence that the disc occurrence rate is any different for planet and non-planet host stars.”

Morales et al. (2012) searched instead for dust around all planet host stars observed with WISE. From about 350 robustly detected systems, nine show an IR-excess ( $\gtrsim 3\sigma$ ) at 12 and/or 22  $\mu\text{m}$ , but none of these candidates are transiting planet host stars. Their occurrence rate (2.6%) of warm dust around planet-bearing stars is lower than that of  $\sim 4\%$  from unbiased samples studied with Spitzer (Bryden et al., 2006; Trilling et al., 2008; Lawler et al., 2009; Carpenter et al., 2009). This difference is explained by Morales et al. (2012) with a lower sensitivity of the WISE satellite and some fainter systems than in the Spitzer sample.

In the case of the faint transit systems and Kepler targets, the source of the excess is under debate. A cool companion would have to be anomalously bright to be seen at distances of several hundreds of parsecs. While Ribas et al. (2012) found an alignment with a cool foreground object or a background galaxy improbable to explain the IR excesses, Kennedy & Wyatt (2012) estimated that the incidence of background galaxies is similar to their findings of systems with IR excess. Another explanation could be the interaction of the host star with an interstellar-medium (ISM) cloud. There could be an alignment between a candidate and a clump of interstellar medium with a population of very small particles. Mid-IR spectroscopy and observations in



longer wavelengths will help to identify the particle sizes and the role of the ISM altogether.

Our preferred explanation for the IR excess was warm dust, but the origin and the production mechanisms of the presumed dust are unclear. For our cases, we had computed the dust mass expected to be produced through a steady-state collisional cascade in a belt of “asteroids” with moderate eccentricities, using the model of Löhne et al. (2008) with a velocity-dependent critical fragmentation energy from Stewart & Leinhardt (2009). At ages of  $\sim 1$  Gyr, the maximum expected dust mass is  $\sim 10^{-4}M_{\oplus}$  at  $r_d = 10$  AU and  $\sim 10^{-5}M_{\oplus}$  at  $r_d = 6$  AU. Comparing with Tab. 5.3, we concluded that the amount of dust in our systems is close to, or even somewhat greater than, the theoretical maximum allowed by a steady-state collisional cascade. This means that we might have a similar difficulty that exists in explaining other systems with hot excesses that have been known before, such as HD 69830 (Beichman et al., 2005a),  $\eta$  Corvi (Wyatt et al., 2005; Lisse et al., 2012), BD+20307 (Song et al., 2005), HD 72905 (Beichman et al., 2006), or HD 23514 (Rhee et al., 2008). Proposed scenarios for such systems include: supply of comets from an outer massive cometary reservoir, possibly following a recent dynamical instability such as the Late Heavy Bombardment; the inward-scattering and disintegration of a large object from such an outer reservoir; a recent major collision between two large planetesimals (see Payne et al., 2009, and references therein). Finally, a possibility of a steady-state collisional dust production can be resuscitated if one allows the asteroids in the belt to have very eccentric orbits (Wyatt et al., 2010). Such a belt could result from shepherding and scattering of an initial planetesimal belt during the inward migration of “hot Jupiters” (Payne et al., 2009).

Each of our two candidates presented here hosts one known close-in planet and, if the excesses are real, an asteroid belt-size dust ring well outside the planetary orbit. In both cases, more planets could orbit both inside and outside the belts. Additional planets at  $\lesssim 10$  AU could be revealed by in-depth RV analyses, by transits, or by transit time variations of already known planets (Maciejewski et al., 2011a). The latter method was used for TrES-2 (Rätz et al., 2009) and XO-5 (Maciejewski et al., 2011b). Non-detection is consistent with the presence of debris belts at several AU, which are incompatible with planets in that region. In the case of TrES-2, Rätz et al. (2009) noticed a second dip in the light curve, both in their own light curves and those published in the literature. This second dip has been observed several times and then disappeared. In addition to other possible reasons for this effect, discussed by Rätz et al., it could be due to an occultation by material in the debris disk. Estimates show

that a clump of dust produced in a recent collision of two  $\sim 100$  km-sized planetesimals would bear enough cross section to account for such a dip before it is azimuthally spread into a ring in a few years, although the probability of witnessing such an event is low.

Planets at largest orbital radii ( $\gtrsim 10$  AU) will be hard to find by the transit technique. Direct imaging and astrometry are not feasible either, since these systems are too old and too distant. It will also be difficult to search for possible Kuiper belt analogues on the periphery of the systems, because they are too faint for far-IR facilities such as *Herschel*. However, future mid-IR instruments such as *JWST/MIRI* should have enough sensitivity to study warm dust in great detail, including dust grain spectroscopy.

# Chapter 6

## Conclusions

In this thesis the architecture of selected *full planetary systems* is studied. This expression refers to systems which contain one or more planets, as well as at least one debris disk. The architecture of the 36 known full planetary systems, as they are known nowadays, can be categorized into two groups: “*tight systems*”, in which the components (planets, debris disks) are tightly spaced with little or no space for additional components; and “*loose systems*”, which show a large gap and plenty of space for additional components. In the majority of loose systems debris disks are discovered farther out and planets are found closer to the star. Whether this is an observational bias or a real feature of planet formation and evolution is still uncertain. Future observations may either discover further components, filling the void and reclassify the system as a tight one, or help to understand processes during planet formation and evolution which may cause the gap.

Although an analysis of each component – be it the star, the planets, or the dust and planetesimals – can shed light onto the system and its history, with information on all of them one can draw a much more detailed picture. Additionally, mutual interactions between the components can help to find more parameters or give constraints which might not have been found in a uniform system. Therefore, we studied two full planetary systems in detail. HR 8799 and  $\varepsilon$  Eridani. Additionally, we tried to extend the list of full planetary systems by searching for IR excesses in systems with transiting planets.

### 6.1 HR 8799

HR 8799 is beside the Solar System a prime example for a tight system. Four massive planets have been imaged directly, and a significant amount of warm and cold dust has been detected. For this system we performed a detailed analysis of all components, from the star, over the planets to the planetesimals and the dust. In the literature we found a wide range of age estimates for the star, reaching from 20 Myr to over 1 Gyr. An analysis of the stellar rotation estimated the inclination of the equator to  $13^{\circ}$ – $30^{\circ}$ , which can possibly be the inclination of the whole system. With the help

of evolutionary models, using the stellar age and measured planetary luminosities, we estimated the planetary masses to range between  $3M_{\text{Jup}}$  and  $50M_{\text{Jup}}$ , for the youngest and oldest estimated age, respectively. We used dynamical simulations to constrain the unknown orbital configuration – i.e., the inclination ( $i$ ) and the rotation angle ( $\Omega$ ), which defines the true radial distance of the planets. The simulations revealed that the system is most stable with an inclination of  $20^\circ$ – $30^\circ$  and an rotation angle of  $20^\circ$ – $50^\circ$ . This area in the  $(i, \Omega)$ -phase space is encircled by 1:2 mean-motion resonances between b-c, c-d and d-e, respectively. Thus, a configuration of multiple mean-motion resonances are probable. In our simulation not only the orientation of the system was varied, but also the mass of the planets between  $5M_{\text{Jup}}$  and  $13M_{\text{Jup}}$ , implying an age of 30 Myr and 160 Myr, respectively. Simulations with lower mass planets appear to be stable over larger time scales. While a setup with the three first-discovered planets are stable up to 100 Myr, adding a fourth planet reduces the period of stability down to a few tens of megayears. In our model of the SED the inner ( $\sim 10$  AU) and outer ( $\gtrsim 100$  AU) dust disk have dust masses of  $1.1 \times 10^{-5}M_{\oplus}$  and  $5 \times 10^{-2}M_{\oplus}$ , respectively. The high luminosity of the cold dust also favors a young age, since old system are not expected to have comparable amounts of dust (Su et al., 2006). The simulations of the planetesimals also show that the belts are stable against gravitational perturbation of the planets.

While in our simulations the phase space was constrained to coplanarity and initially circular orbits to reduce the time of simulations to a manageable amount, further simulations may consider more parameters, such as mutual inclinations and individual eccentricities. To keep the amount of simulations in a practical frame, one could constrain the initial conditions to a configuration with mean-motion resonances between the planets, since many planets are observed to orbit in or at least near a mean-motion resonance (Zhou et al., 2012). Observations will also help to constrain the orbits of the planets. The successful discovery of the four planets via direct imaging attracted wide interest, and within a few years, follow-up observations (Hinz et al., 2010; Marois et al., 2010; Currie et al., 2011a; Bergfors et al., 2011; Galicher et al., 2011; Madhusudhan et al., 2011) and findings in archived images from Subaru, Keck or HST (Fukagawa et al., 2009; Metchev et al., 2009; Lafrenière et al., 2009; Soummer et al., 2011; Currie et al., 2012) accumulate 24 astrometric positions of the companions. Since the inner planet has a period of  $\sim 50$  years, it will be possible to measure orbital curvature after only 2 years (Marois et al., 2010). Of further interest may be the inner region within the inner planetesimal belt, e.g., what kind of planet(s) can orbit there without destabilizing the inner belt.

Spectroscopic observations show an unusual atmospheric SEDs compared to field brown dwarfs (Marois et al., 2008, 2010; Lafrenière et al., 2009; Metchev et al., 2009; Janson et al., 2010; Hinz et al., 2010; Currie et al., 2011a; Barman et al., 2011; Galicher et al., 2011; Skemer et al., 2012). The modeling of the SED indicates that non-equilibrium chemistry and complex cloud structures may play an important role in the physics of young exoplanets (Janson et al., 2010). A better understanding of planetary atmospheres can give constraints to evolutionary models and may help to distinguish between formation scenarios, either core accretion or gravitational instability.

Beside the planets, the new facilities ALMA and JCMT/SCUBA2 are expected to resolve the outer disk around HR 8799, providing insights in the disk structure and geometry. This can give further constraints on orientation of the disk, and the whole system, if one assumes coplanarity.

## 6.2 $\varepsilon$ Eridani

$\varepsilon$  Eridani is a typical loose system with a large outer disk (Greaves et al., 1998, 2005) and a planet at a few AU (Hatzes et al., 2000). Further, the SED shows an excess of warm dust in the vicinity of the planet (Backman et al., 2009). The origin of the warm dust is puzzling, since a belt of planetesimals as the source of dust in the direct proximity would already be cleared by the planet (Brogi et al., 2009). We therefore modeled the dust production of the outer ring, including collisions and transport effects due to Poynting-Robertson effect and stellar-wind drag. Our simulations show, that due to the strong stellar wind (Wood et al., 2002) small dust grains of submicron size are transported inward close to the star without appreciable loss due to mutual collisions. The quantity of small particles reaching the inner region is in good agreement with the quantity of warm dust needed to reproduce the SED. Additionally, we tested the influence of the two orbital solutions of the RV planet given by Benedict et al. (2006) and Butler et al. (2006). While the first solution predicts an eccentric orbit with  $e = 0.7$ , and the other one gives a moderate eccentricity of  $e = 0.25$ , both solutions have little effect on the SED. The SED of both solutions fit well with the IRS spectrum. Even a scenario without an inner planet would fit with IRS spectrum. Thus, we cannot draw any conclusions on the different orbital solutions. Another important result of our analysis is that the outer disk could not be modeled with a composition of pure “astronomical silicate” (Laor & Draine, 1993), the resulting SED would be too warm. While modeling the SED, we achieved the best fit with a mixture

of 30% silicate and 70% water ice. Since sublimation of ice is expected at  $\approx 10$  AU the inner part of the disk was modeled with pure astronomical silicate again.

Due to stellar magnetic activity it proved to be difficult to identify the radial-velocity signature of the inner planet (Anglada-Escudé & Butler, 2012). Further observations, e.g., with HARPS, will be necessary to specify the orbit of the inner planet. While direct observation of the inner planet are unlikely due to the old age of the system and the close proximity to the star, there are ongoing efforts to image an assumed outer planet at  $\approx 40$  AU (Itoh et al., 2006; Marengo et al., 2006; Janson et al., 2007, 2008; Marengo et al., 2009), which is thought to be responsible for the gap and a clumpy structure of the outer dust disk seen in sub-mm (Greaves et al., 1998, 2005). Observations with ALMA, JCMT/SCUBA2 (J. Greaves, pers. comm.), Herschel/PACS, and /SPIRE are expected to substantiate the structure of the outer disk which may allow more precise predictions for the existence of the outer planet. The inner part of the disk may be probed with the future instrument JWST/MIRI.

### 6.3 Dust in systems with transiting planets

The last part of this work contains our search for debris disks in systems with transiting planets. This search was motivated by the fact that no debris disk had been discovered before in systems with transiting planets and that transits provide important information on the planets, which are not accessible with other existing methods so far. Research in the available databases of IRAS, ISO, Spitzer, and AKARI quarried only five observed transit systems, but none of them showed an excess. In contrast, in the *preliminary* catalog of the *Wide-field Infrared Survey Explorer* (WISE) 53 of 93 known transit systems have been listed. A rough photospheric fit to the first two bands of the WISE measurements (W1 & W2) reduced the list to four possible candidates for IR excess: CoRoT-8, HAT-P-5, TrES-2, and XO-5. In our further analysis we concentrated on the latter two systems, since CoRoT-8 only showed an excess in the last band (W4), and HAT-P-5 was excluded due to low joint significance level ( $\chi_{\text{joint}} < 3$ ). We tried to derive the properties of the dust disk in the systems. The dust rings were found to be at 6–8 AU, far outside of the planetary orbits, and with high fractional luminosities of  $f_d \approx (3-6) \times 10^{-4}$ . In the meantime, our results could not be confirmed and in the *final* release catalog of the WISE mission, all four candidates are now flagged in the W4 band as 95% upper limit. Other authors also tried to identify warm dust excess around systems with (transiting) planets (Ribas et al.,

2012; Kennedy & Wyatt, 2012; Morales et al., 2012), but their results are still under discussion. Altogether, all authors agree to each other that warm dust must be rare.

One reason for the rare findings of dust in system with transiting planets is the large distance most systems are found. Only 21 out of 233 known transit systems (2012-10-25) are within 100 pc. The majority are found at several hundreds of parsecs. At such distances debris dust is hard to detect with present-day telescopes. Especially systems with warm debris disk must be very young or the disks need to be very massive to be detected with current instruments. Future instruments such as JWST/MIRI may provide sufficient sensitivity to discover more dust in transit systems.





# References

- Absil, O., Di Folco, E., Mérand, A., et al. (2006), “Circumstellar material in the Vega inner system revealed by CHARA/FLUOR”, *Astron. Astrophys.*, 452:237–244
- Absil, O., Di Folco, E., Mérand, A., et al. (2008), “A near-infrared interferometric survey of debris disc stars. II. CHARA/FLUOR observations of six early-type dwarfs”, *Astron. Astrophys.*, 487:1041–1054
- Alexander, R. D., Clarke, C. J., & Pringle, J. E. (2006), “Photoevaporation of protoplanetary discs - II. Evolutionary models and observable properties”, *MNRAS*, 369:229–239
- Allende Prieto, C. & Lambert, D. L. (1999), “Fundamental parameters of nearby stars from the comparison with evolutionary calculations: masses, radii and effective temperatures”, *Astron. Astrophys.*, 352:555–562
- Andrews, S. M. & Williams, J. P. (2005), “Circumstellar Dust Disks in Taurus-Auriga: The Submillimeter Perspective”, *Astrophys. J.*, 631:1134–1160
- Anglada-Escudé, G. & Butler, R. P. (2012), “The HARPS-TERRA Project. I. Description of the Algorithms, Performance, and New Measurements on a Few Remarkable Stars Observed by HARPS”, *Astrophys. J. Suppl.*, 200:15
- Armitage, P. J. (2010), *Astrophysics of Planet Formation*, Cambridge: University Press, 2010
- Augereau, J. C., Nelson, R. P., Lagrange, A. M., et al. (2001), “Dynamical modeling of large scale asymmetries in the beta Pictoris dust disk”, *Astron. Astrophys.*, 370:447–455
- Aumann, H. H., Beichman, C. A., Gillett, F. C., et al. (1984), “Discovery of a shell around Alpha Lyrae”, *Astrophys. J. Letters*, 278:L23–L27
- Backman, D., Marengo, M., Stapelfeldt, K., et al. (2009), “Epsilon Eridani’s Planetary Debris Disk: Structure and Dynamics Based on Spitzer and Caltech Submillimeter Observatory Observations”, *Astrophys. J.*, 690:1522–1538
- Baines, E. K., White, R. J., Huber, D., et al. (2012), “The CHARA Array Angular Diameter of HR 8799 Favors Planetary Masses for its Imaged Companions”, *Astrophys. J.*, 761:57
- Bakos, G. Á., Shporer, A., Pál, A., et al. (2007), “HAT-P-5b: A Jupiter-like Hot Jupiter Transiting a Bright Star”, *Astrophys. J. Letters*, 671:L173–L176
- Balbus, S. A. & Hawley, J. F. (1991), “A powerful local shear instability in weakly magnetized disks. I - Linear analysis. II - Nonlinear evolution”, *Astrophys. J.*, 376:214–233

- Baraffe, I., Chabrier, G., Allard, F., et al. (1998), “Evolutionary models for solar metallicity low-mass stars: mass-magnitude relationships and color-magnitude diagrams”, *Astron. Astrophys.*, 337:403–412
- Baraffe, I., Chabrier, G., Allard, F., et al. (2002), “Evolutionary models for low-mass stars and brown dwarfs: Uncertainties and limits at very young ages”, *Astron. Astrophys.*, 382:563–572
- Baraffe, I., Chabrier, G., & Barman, T. (2008), “Structure and evolution of super-Earth to super-Jupiter exoplanets. I. Heavy element enrichment in the interior”, *Astron. Astrophys.*, 482:315–332
- Baraffe, I., Chabrier, G., Barman, T. S., et al. (2003), “Evolutionary models for cool brown dwarfs and extrasolar giant planets. The case of HD 209458”, *Astron. Astrophys.*, 402:701–712
- Barman, T. S., Macintosh, B., Konopacky, Q. M., et al. (2011), “Clouds and Chemistry in the Atmosphere of Extrasolar Planet HR8799b”, *Astrophys. J.*, 733:65
- Barucci, M. A., Brown, M. E., Emery, J. P., et al. (2008), “Composition and Surface Properties of Transneptunian Objects and Centaurs”, in Barucci, M. A., Boehnhardt, H., Cruikshank, D. P., & Morbidelli, A. (Editor), “The Solar System Beyond Neptune”, pp. 143–160
- Beichman, C. A., Bryden, G., Gautier, T. N., et al. (2005a), “An Excess Due to Small Grains around the Nearby K0 V Star HD 69830: Asteroid or Cometary Debris?”, *Astrophys. J.*, 626:1061–1069
- Beichman, C. A., Bryden, G., Rieke, G. H., et al. (2005b), “Planets and Infrared Excesses: Preliminary Results from a Spitzer MIPS Survey of Solar-Type Stars”, *Astrophys. J.*, 622:1160–1170
- Beichman, C. A., Neugebauer, G., Habing, H. J., et al. (Editors) (1988), *Infrared astronomical satellite (IRAS) catalogs and atlases. Volume 1: Explanatory supplement*, vol. 1
- Beichman, C. A., Tanner, A., Bryden, G., et al. (2006), “IRS Spectra of Solar-Type Stars: A Search for Asteroid Belt Analogs”, *Astrophys. J.*, 639:1166–1176
- Benedict, G. F., McArthur, B. E., Gatewood, G., et al. (2006), “The Extrasolar Planet  $\epsilon$  Eridani b: Orbit and Mass”, *Astron. J.*, 132:2206–2218
- Benz, W. & Asphaug, E. (1999), “Catastrophic Disruptions Revisited”, *Icarus*, 142:5–20
- Bergfors, C., Brandner, W., Janson, M., et al. (2011), “VLT/NACO astrometry of the HR 8799 planetary system. L'-band observations of the three outer planets”, *Astron. Astrophys.*, 528:A134
- Blum, J. & Wurm, G. (2008), “The Growth Mechanisms of Macroscopic Bodies in Protoplanetary Disks”, *Ann. Rev. Astron. Astrophys.*, 46:21–56

- Bodenheimer, P. & Pollack, J. B. (1986), “Calculations of the accretion and evolution of giant planets The effects of solid cores”, *Icarus*, 67:391–408
- Bohren, C. F. & Huffman, D. R. (1983), *Absorption and scattering of light by small particles*, New York: Wiley, 1983
- Boley, A. C., Payne, M. J., Corder, S., et al. (2012), “Constraining the Planetary System of Fomalhaut Using High-resolution ALMA Observations”, *Astrophys. J. Letters*, 750:L21
- Bordé, P., Bouchy, F., Deleuil, M., et al. (2010), “Transiting exoplanets from the CoRoT space mission. XI. CoRoT-8b: a hot and dense sub-Saturn around a K1 dwarf”, *Astron. Astrophys.*, 520:A66
- Boss, A. P. (1997), “Giant planet formation by gravitational instability.”, *Science*, 276:1836–1839
- Boss, A. P. (1998), “Evolution of the Solar Nebula. IV. Giant Gaseous Protoplanet Formation”, *Astrophys. J.*, 503:923
- Boss, A. P. (2011), “Formation of Giant Planets by Disk Instability on Wide Orbits Around Protostars with Varied Masses”, *Astrophys. J.*, 731:74
- Brauer, F., Dullemond, C. P., & Henning, T. (2008), “Coagulation, fragmentation and radial motion of solid particles in protoplanetary disks”, *Astron. Astrophys.*, 480:859–877
- Briggs, R. E. (1962), “Steady-state space distribution of meteoric particles under the operation of the Poynting-Robertson effect”, *Astron. J.*, 67:710–723
- Brogi, M., Marzari, F., & Paolicchi, P. (2009), “Dynamical stability of the inner belt around Epsilon Eridani”, *Astron. Astrophys.*, 499:L13–L16
- Bryden, G., Beichman, C. A., Carpenter, J. M., et al. (2009), “Planets and Debris Disks: Results from a Spitzer/MIPS Search for Infrared Excess”, *Astrophys. J.*, 705:1226–1236
- Bryden, G., Beichman, C. A., Trilling, D. E., et al. (2006), “Frequency of Debris Disks around Solar-Type Stars: First Results from a Spitzer MIPS Survey”, *Astrophys. J.*, 636:1098–1113
- Burns, J. A., Lamy, P. L., & Soter, S. (1979), “Radiation forces on small particles in the solar system”, *Icarus*, 40:1–48
- Burrows, A., Marley, M., Hubbard, W. B., et al. (1997), “A Nongray Theory of Extrasolar Giant Planets and Brown Dwarfs”, *Astrophys. J.*, 491:856–+
- Burrows, A., Rauscher, E., Spiegel, D. S., et al. (2010), “Photometric and Spectral Signatures of Three-dimensional Models of Transiting Giant Exoplanets”, *Astrophys. J.*, 719:341–350

- Burrows, C. J., Krist, J. E., Stapelfeldt, K. R., et al. (1995), “HST Observations of the Beta Pictoris Circumstellar Disk”, in “American Astronomical Society Meeting Abstracts”, vol. 27 of *Bulletin of the American Astronomical Society*, p. 1329
- Butler, R. P., Wright, J. T., Marcy, G. W., et al. (2006), “Catalog of Nearby Exoplanets”, *Astrophys. J.*, 646:505–522
- Cameron, A. G. W. (1978), “Physics of the primitive solar accretion disk”, *Moon and Planets*, 18:5–40
- Carpenter, J. M., Bouwman, J., Mamajek, E. E., et al. (2009), “Formation and Evolution of Planetary Systems: Properties of Debris Dust Around Solar-Type Stars”, *Astrophys. J. Suppl.*, 181:197–226
- Carpenter, J. M., Bouwman, J., Silverstone, M. D., et al. (2008), “The Formation and Evolution of Planetary Systems: Description of the Spitzer Legacy Science Database”, *Astrophys. J. Suppl.*, 179:423–450
- Chabrier, G. & Baraffe, I. (1997), “Structure and evolution of low-mass stars”, *Astron. Astrophys.*, 327:1039–1053
- Chabrier, G., Baraffe, I., Allard, F., et al. (2000), “Evolutionary Models for Very Low-Mass Stars and Brown Dwarfs with Dusty Atmospheres”, *Astrophys. J.*, 542:464–472
- Chabrier, G., Baraffe, I., Allard, F., et al. (2005), “Review on low-mass stars and brown dwarfs”, *ArXiv Astrophysics e-prints*
- Chambers, J. E. (1999), “A hybrid symplectic integrator that permits close encounters between massive bodies”, *MNRAS*, 304:793–799
- Chambers, J. E. (2001), “Making More Terrestrial Planets”, *Icarus*, 152:205–224
- Charbonneau, D., Brown, T. M., Latham, D. W., et al. (2000), “Detection of Planetary Transits Across a Sun-like Star”, *Astrophys. J. Letters*, 529:L45–L48
- Chauvin, G., Lagrange, A.-M., Beust, H., et al. (2012), “Orbital characterization of the  $\beta$  Pictoris b giant planet”, *Astron. Astrophys.*, 542:A41
- Chen, C. H., Sargent, B. A., Bohac, C., et al. (2006), “Spitzer IRS Spectroscopy of IRAS-discovered Debris Disks”, *Astrophys. J. Suppl.*, 166:351–377
- Chiang, E., Kite, E., Kalas, P., et al. (2009), “Fomalhaut’s Debris Disk and Planet: Constraining the Mass of Fomalhaut b from disk Morphology”, *Astrophys. J.*, 693:734–749
- Chiang, E. & Youdin, A. N. (2010), “Forming Planetesimals in Solar and Extrasolar Nebulae”, *Annual Review of Earth and Planetary Sciences*, 38:493–522
- Clarke, C. J., Gendrin, A., & Sotomayor, M. (2001), “The dispersal of circumstellar discs: the role of the ultraviolet switch”, *MNRAS*, 328:485–491
- Close, L. M. & Males, J. R. (2010), “A Search for Wide Companions to the Extrasolar Planetary System HR 8799”, *Astrophys. J.*, 709:342–348

- Cohen, M., Wheaton, W. A., & Megeath, S. T. (2003), “Spectral Irradiance Calibration in the Infrared. XIV. The Absolute Calibration of 2MASS”, *Astron. J.*, 126:1090–1096
- Cowen, R. (2012), “Hubble to revisit exoplanet puzzle”, *Nature*, 485:428
- Currie, T., Burrows, A., Itoh, Y., et al. (2011a), “A Combined Subaru/VLT/MMT 1–5  $\mu\text{m}$  Study of Planets Orbiting HR 8799: Implications for Atmospheric Properties, Masses, and Formation”, *Astrophys. J.*, 729:128
- Currie, T., Fukagawa, M., Thalmann, C., et al. (2012), “Direct Detection and Orbital Analysis of the Exoplanets HR 8799 bcd from Archival 2005 Keck/NIRC2 Data”, *Astrophys. J. Letters*, 755:L34
- Currie, T., Thalmann, C., Matsumura, S., et al. (2011b), “A 5  $\mu\text{m}$  Image of  $\beta$  Pictoris b at a Sub-Jupiter Projected Separation: Evidence for a Misalignment Between the Planet and the Inner, Warped Disk”, *Astrophys. J. Letters*, 736:L33
- Cuzzi, J. N. & Weidenschilling, S. J. (2006), *Particle-Gas Dynamics and Primary Accretion*, pp. 353–381
- Deller, A. T. & Maddison, S. T. (2005), “Numerical Modeling of Dusty Debris Disks”, *Astrophys. J.*, 625:398–413
- Di Folco, E., Absil, O., Augereau, J.-C., et al. (2007), “A near-infrared interferometric survey of debris disk stars. I. Probing the hot dust content around  $\epsilon$  Eridani and  $\tau$  Ceti with CHARA/FLUOR”, *Astron. Astrophys.*, 475:243–250
- Di Folco, E., Thévenin, F., Kervella, P., et al. (2004), “VLTI near-IR interferometric observations of Vega-like stars. Radius and age of  $\alpha$  PsA,  $\beta$  Leo,  $\beta$  Pic,  $\epsilon$  Eri and  $\tau$  Cet”, *Astron. Astrophys.*, 426:601–617
- Dodson-Robinson, S. E., Beichman, C. A., Carpenter, J. M., et al. (2011), “A Spitzer Infrared Spectrograph Study of Debris Disks Around Planet-host Stars”, *Astron. J.*, 141:11
- Dohnanyi, J. S. (1969), “Collisional model of asteroids and their debris”, *J. Geophys. Res.*, 74:2531–2554
- Dominik, C., Blum, J., Cuzzi, J. N., et al. (2007), “Growth of Dust as the Initial Step Toward Planet Formation”, *Protostars and Planets V*, pp. 783–800
- Draine, B. T. (2003), “Scattering by Interstellar Dust Grains. I. Optical and Ultraviolet”, *Astrophys. J.*, 598:1017–1025
- Dullemond, C. P. & Dominik, C. (2005), “Dust coagulation in protoplanetary disks: A rapid depletion of small grains”, *Astron. Astrophys.*, 434:971–986
- Duncan, M., Quinn, T., & Tremaine, S. (1989), “The long-term evolution of orbits in the solar system - A mapping approach”, *Icarus*, 82:402–418

- Durda, D. D., Greenberg, R., & Jedicke, R. (1998), “Collisional Models and Scaling Laws: A New Interpretation of the Shape of the Main-Belt Asteroid Size Distribution”, *Icarus*, 135:431–440
- Eiroa, C., Marshall, J. P., Mora, A., et al. (2011), “Herschel discovery of a new class of cold, faint debris discs”, *Astron. Astrophys.*, 536:L4
- Faber, P. & Quillen, A. C. (2007), “The total number of giant planets in debris discs with central clearings”, *MNRAS*, 382:1823–1828
- Fabrycky, D. C. & Murray-Clay, R. A. (2010), “Stability of the Directly Imaged Multiplanet System HR 8799: Resonance and Masses”, *Astrophys. J.*, 710:1408–1421
- Fabrycky, D. C. & Winn, J. N. (2009), “Exoplanetary Spin-Orbit Alignment: Results from the Ensemble of Rossiter-McLaughlin Observations”, *Astrophys. J.*, 696:1230–1240
- Freistetter, F., Krivov, A. V., & Löhne, T. (2007), “Planets of  $\beta$  Pictoris revisited”, *Astron. Astrophys.*, 466:389–393
- Fujiwara, A., Kamimoto, G., & Tsukamoto, A. (1977), “Destruction of basaltic bodies by high-velocity impact”, *Icarus*, 31:277–288
- Fukagawa, M., Itoh, Y., Tamura, M., et al. (2009), “H-Band Image of a Planetary Companion Around HR 8799 in 2002”, *Astrophys. J.*, 696:L1–L5
- Galicher, R., Marois, C., Macintosh, B., et al. (2011), “M-band Imaging of the HR 8799 Planetary System Using an Innovative LOCI-based Background Subtraction Technique”, *Astrophys. J. Letters*, 739:L41
- Gammie, C. F. (2001), “Nonlinear Outcome of Gravitational Instability in Cooling, Gaseous Disks”, *Astrophys. J.*, 553:174–183
- Golimowski, D. A., Ardila, D. R., Krist, J. E., et al. (2006), “Hubble Space Telescope ACS Multiband Coronagraphic Imaging of the Debris Disk around  $\beta$  Pictoris”, *Astron. J.*, 131:3109–3130
- Goździewski, K. & Migaszewski, C. (2009), “Is the HR 8799 extrasolar system destined for planetary scattering?”, *MNRAS*, 397:L16–L20
- Gray, R. O. & Kaye, A. B. (1999), “HR 8799: A Link between  $\gamma$  Doradus Variables and  $\lambda$  Bootis Stars”, *Astron. J.*, 118:2993–2996
- Greaves, J. S., Fischer, D. A., & Wyatt, M. C. (2006), “Metallicity, debris discs and planets”, *MNRAS*, 366:283–286
- Greaves, J. S., Holland, W. S., Jayawardhana, R., et al. (2004), “A search for debris discs around stars with giant planets”, *MNRAS*, 348:1097–1104
- Greaves, J. S., Holland, W. S., Moriarty-Schieven, G., et al. (1998), “A Dust Ring around epsilon Eridani: Analog to the Young Solar System”, *Astrophys. J. Letters*, 506:L133–L137

- Greaves, J. S., Holland, W. S., Wyatt, M. C., et al. (2005), “Structure in the  $\varepsilon$  Eridani Debris Disk”, *Astrophys. J. Letters*, 619:L187–L190
- Greenberg, R., Hartmann, W. K., Chapman, C. R., et al. (1978), “Planetesimals to planets - Numerical simulation of collisional evolution”, *Icarus*, 35:1–26
- Gustafson, B. A. S. (1994), “Physics of Zodiacal Dust”, *Annual Review of Earth and Planetary Sciences*, 22:553–595
- Güttler, C., Blum, J., Zsom, A., et al. (2010), “The outcome of protoplanetary dust growth: pebbles, boulders, or planetesimals?. I. Mapping the zoo of laboratory collision experiments”, *Astron. Astrophys.*, 513:A56+
- Haisch, Jr., K. E., Lada, E. A., & Lada, C. J. (2001), “Disk Frequencies and Lifetimes in Young Clusters”, *Astrophys. J. Letters*, 553:L153–L156
- Hatzes, A. P., Cochran, W. D., McArthur, B., et al. (2000), “Evidence for a Long-Period Planet Orbiting  $\varepsilon$  Eridani”, *Astrophys. J. Letters*, 544:L145–L148
- Hauschildt, P. H., Allard, F., & Baron, E. (1999), “The NextGen Model Atmosphere Grid for  $3000 \leq T_{\text{eff}} \leq 10000$  K”, *Astrophys. J.*, 512:377–385
- Hayashi, C. (1981), “Formation of the planets”, in D. Sugimoto, D. Q. Lamb, & D. N. Schramm (Editor), “Fundamental Problems in the Theory of Stellar Evolution”, vol. 93 of *IAU Symposium*, pp. 113–126
- Heap, S. R., Lindler, D. J., Lanz, T. M., et al. (2000), “Space Telescope Imaging Spectrograph Coronagraphic Observations of  $\beta$  Pictoris”, *Astrophys. J.*, 539:435–444
- Helling, C., Ackerman, A., Allard, F., et al. (2008), “A comparison of chemistry and dust cloud formation in ultracool dwarf model atmospheres”, *MNRAS*, 391:1854–1873
- Helou, G. & Walker, D. W. (Editors) (1988), *Infrared astronomical satellite (IRAS) catalogs and atlases. Volume 7: The small scale structure catalog*, vol. 7
- Henry, L. G., Forbes, J. E., & Gould, N. L. (1964), “A New Method of Automatic Computation of Stellar Evolution.”, *Astrophys. J.*, 139:306
- Hildebrand, R. H. (1983), “The Determination of Cloud Masses and Dust Characteristics from Submillimetre Thermal Emission”, *Quarterly Journal of the Royal Astronomical Society*, 24:267
- Hillenbrand, L. A., Carpenter, J. M., Kim, J. S., et al. (2008), “The Complete Census of 70  $\mu\text{m}$ -bright Debris Disks within “the Formation and Evolution of Planetary Systems” Spitzer Legacy Survey of Sun-like Stars”, *Astrophys. J.*, 677:630–656
- Hillenbrand, L. A., Strom, S. E., Calvet, N., et al. (1998), “Circumstellar Disks in the Orion Nebula Cluster”, *Astron. J.*, 116:1816–1841

- Hinz, P. M., Rodigas, T. J., Kenworthy, M. A., et al. (2010), “Thermal Infrared MMTAO Observations of the HR 8799 Planetary System”, *Astrophys. J.*, 716:417–426
- Høg, E., Fabricius, C., Makarov, V. V., et al. (2000), “The Tycho-2 catalogue of the 2.5 million brightest stars”, *Astron. Astrophys.*, 355:L27–L30
- Hollenbach, D., Johnstone, D., Lizano, S., et al. (1994), “Photoevaporation of disks around massive stars and application to ultracompact H II regions”, *Astrophys. J.*, 428:654–669
- Hughes, A. M., Wilner, D. J., Andrews, S. M., et al. (2011), “Resolved Submillimeter Observations of the HR 8799 and HD 107146 Debris Disks”, *Astrophys. J.*, 740:38
- Ida, S. (1990), “Stirring and dynamical friction rates of planetesimals in the solar gravitational field”, *Icarus*, 88:129–145
- Ida, S., Bryden, G., Lin, D. N. C., et al. (2000), “Orbital Migration of Neptune and Orbital Distribution of Trans-Neptunian Objects”, *Astrophys. J.*, 534:428–445
- Ida, S. & Makino, J. (1993), “Scattering of planetesimals by a protoplanet - Slowing down of runaway growth”, *Icarus*, 106:210
- Ikoma, M., Emori, H., & Nakazawa, K. (2001), “Formation of Giant Planets in Dense Nebulae: Critical Core Mass Revisited”, *Astrophys. J.*, 553:999–1005
- Ishihara, D., Onaka, T., Kataza, H., et al. (2010), “The AKARI/IRC mid-infrared all-sky survey”, *Astron. Astrophys.*, 514:A1
- Itoh, Y., Oasa, Y., & Fukagawa, M. (2006), “Coronagraphic Search for Extrasolar Planets around  $\epsilon$  Eri and Vega”, *Astrophys. J.*, 652:1729–1733
- Janson, M., Bergfors, C., Goto, M., et al. (2010), “Spatially Resolved Spectroscopy of the Exoplanet HR 8799 c”, *Astrophys. J. Letters*, 710:L35–L38
- Janson, M., Brandner, W., Henning, T., et al. (2007), “NACO-SDI Direct Imaging Search for the Exoplanet  $\epsilon$  Eri b”, *Astron. J.*, 133:2442–2456
- Janson, M., Carson, J. C., Lafrenière, D., et al. (2012), “Infrared Non-detection of Fomalhaut b: Implications for the Planet Interpretation”, *Astrophys. J.*, 747:116
- Janson, M., Reffert, S., Brandner, W., et al. (2008), “A comprehensive examination of the  $\epsilon$  Eridani system. Verification of a 4 micron narrow-band high-contrast imaging approach for planet searches”, *Astron. Astrophys.*, 488:771–780
- Johansen, A., Oishi, J. S., Low, M.-M. M., et al. (2007), “Rapid planetesimal formation in turbulent circumstellar disks”, *Nature*, 448:1022–1025
- Jura, M., Chen, C. H., Furlan, E., et al. (2004), “Mid-Infrared Spectra of Dust Debris around Main-Sequence Stars”, *Astrophys. J. Suppl.*, 154:453–457
- Kalas, P., Graham, J. R., Chiang, E., et al. (2008), “Optical Images of an Exosolar Planet 25 Light-Years from Earth”, *Science*, 322:1345–



- Kalas, P., Graham, J. R., & Clampin, M. (2005), “A planetary system as the origin of structure in Fomalhaut’s dust belt”, *Nature*, 435:1067–1070
- Kaye, A. B. & Strassmeier, K. G. (1998), “CA II H&K survey of Gamma Doradus candidates”, *MNRAS*, 294:L35–L39
- Kennedy, G. M. & Wyatt, M. C. (2010), “Are debris discs self-stirred?”, *MNRAS*, 405:1253–1270
- Kennedy, G. M. & Wyatt, M. C. (2012), “Confusion limited surveys: using WISE to quantify the rarity of warm dust around Kepler stars”, *MNRAS*, 426:91–107
- Kenyon, S. J. & Bromley, B. C. (2006), “Terrestrial Planet Formation. I. The Transition from Oligarchic Growth to Chaotic Growth”, *Astron. J.*, 131:1837–1850
- Kenyon, S. J. & Bromley, B. C. (2008), “Variations on Debris Disks: Icy Planet Formation at 30-150 AU for 1-3  $M_{\text{Solar}}$  Main-Sequence Stars”, *Astrophys. J. Suppl.*, 179:451–483
- Kenyon, S. J. & Hartmann, L. (1995), “Pre-Main-Sequence Evolution in the Taurus-Auriga Molecular Cloud”, *Astrophys. J. Suppl.*, 101:117
- Kessler, M. F., Steinz, J. A., Anderegg, M. E., et al. (1996), “The Infrared Space Observatory (ISO) mission.”, *Astron. Astrophys.*, 315:L27–L31
- Kharchenko, N. V. & Roeser, S. (2009), “All-sky Compiled Catalogue of 2.5 million stars”, *VizieR Online Data Catalog*, 1280:0
- Kippenhahn, R. & Weigert, A. (1990), *Stellar Structure and Evolution*
- Kirsh, D. R., Duncan, M., Brasser, R., et al. (2009), “Simulations of planet migration driven by planetesimal scattering”, *Icarus*, 199:197–209
- Klahr, H. (2004), “The Global Baroclinic Instability in Accretion Disks. II. Local Linear Analysis”, *Astrophys. J.*, 606:1070–1082
- Klahr, H. H. & Bodenheimer, P. (2003), “Turbulence in Accretion Disks: Vorticity Generation and Angular Momentum Transport via the Global Baroclinic Instability”, *Astrophys. J.*, 582:869–892
- Kobayashi, H., Watanabe, S., Kimura, H., et al. (2008), “Dust ring formation due to ice sublimation of radially drifting dust particles under the Poynting Robertson effect in debris disks”, *Icarus*, 195:871–881
- Kobayashi, H., Watanabe, S., Kimura, H., et al. (2009), “Dust ring formation due to sublimation of dust grains drifting radially inward by the Poynting-Robertson drag: An analytical model”, *Icarus*, 201:395–405
- Koerner, D. W., Kim, S., Trilling, D. E., et al. (2010), “New Debris Disk Candidates Around 49 Nearby Stars”, *Astrophys. J. Letters*, 710:L26–L29
- Kóspál, Á., Ardila, D. R., Moór, A., et al. (2009), “On the Relationship Between Debris Disks and Planets”, *Astrophys. J. Letters*, 700:L73–L77

- Kratter, K. M., Murray-Clay, R. A., & Youdin, A. N. (2010), “The Runts of the Litter: Why Planets Formed Through Gravitational Instability Can Only Be Failed Binary Stars”, *Astrophys. J.*, 710:1375–1386
- Krivov, A. V., Löhne, T., & Sremčević, M. (2006), “Dust distributions in debris disks: effects of gravity, radiation pressure and collisions”, *Astron. Astrophys.*, 455:509–519
- Krivov, A. V., Müller, S., Löhne, T., et al. (2008), “Collisional and Thermal Emission Models of Debris Disks: Toward Planetesimal Population Properties”, *Astrophys. J.*, 687:608–622
- Krivov, A. V., Reidemeister, M., Fiedler, S., et al. (2011), “Debris disc candidates in systems with transiting planets”, *MNRAS*, 418:L15–L19
- Krivov, A. V., Sremčević, M., & Spahn, F. (2005), “Evolution of a Keplerian disk of colliding and fragmenting particles: a kinetic model with application to the Edgeworth Kuiper belt”, *Icarus*, 174:105–134
- Lafrenière, D., Marois, C., Doyon, R., et al. (2009), “HST/NICMOS Detection of HR 8799 b in 1998”, *Astrophys. J. Letters*, 694:L148–L152
- Lagrange, A.-M., Boccaletti, A., Milli, J., et al. (2012a), “The position of  $\beta$  Pictoris b position relative to the debris disk”, *Astron. Astrophys.*, 542:A40
- Lagrange, A.-M., Bonnefoy, M., Chauvin, G., et al. (2010), “A Giant Planet Imaged in the Disk of the Young Star  $\beta$  Pictoris”, *Science*, 329:57–
- Lagrange, A.-M., De Bondt, K., Meunier, N., et al. (2012b), “Constraints on planets around  $\beta$  Pic with Harps radial velocity data”, *Astron. Astrophys.*, 542:A18
- Lagrange, A.-M., Gratadour, D., Chauvin, G., et al. (2009), “A probable giant planet imaged in the  $\beta$  Pictoris disk. VLT/NaCo deep L'-band imaging”, *Astron. Astrophys.*, 493:L21–L25
- Laor, A. & Draine, B. T. (1993), “Spectroscopic constraints on the properties of dust in active galactic nuclei”, *Astrophys. J.*, 402:441–468
- Lasker, B. M., Lattanzi, M. G., McLean, B. J., et al. (2008), “The Second-Generation Guide Star Catalog: Description and Properties”, *Astron. J.*, 136:735–766
- Lawler, S. M., Beichman, C. A., Bryden, G., et al. (2009), “Explorations Beyond the Snow Line: Spitzer/IRS Spectra of Debris Disks Around Solar-type Stars”, *Astrophys. J.*, 705:89–111
- Le Bouquin, J.-B., Absil, O., Benisty, M., et al. (2009), “The spin-orbit alignment of the Fomalhaut planetary system probed by optical long baseline interferometry”, *Astron. Astrophys.*, 498:L41–L44
- Li, A. & Greenberg, J. M. (1998), “A comet dust model for the beta Pictoris disk”, *Astron. Astrophys.*, 331:291–313
- Liou, J.-C. & Zook, H. A. (1999), “Signatures of the Giant Planets Imprinted on the Edgeworth-Kuiper Belt Dust Disk”, *Astron. J.*, 118:580–590

- Liou, J.-C., Zook, H. A., & Dermott, S. F. (1996), “Kuiper Belt Dust Grains as a Source of Interplanetary Dust Particles”, *Icarus*, 124:429–440
- Liseau, R., Eiroa, C., Fedele, D., et al. (2010), “Resolving the cold debris disc around a planet-hosting star . PACS photometric imaging observations of  $\eta^1$  Eridani (HD 10647, HR 506)”, *Astron. Astrophys.*, 518:L132
- Lissauer, J. J. (1987), “Timescales for planetary accretion and the structure of the protoplanetary disk”, *Icarus*, 69:249–265
- Lisse, C. M., Wyatt, M. C., Chen, C. H., et al. (2012), “Spitzer Evidence for a Late-heavy Bombardment and the Formation of Ureilites in  $\eta$  Corvi at  $\sim 1$  Gyr”, *Astrophys. J.*, 747:93
- Lithwick, Y. (2009), “Formation, Survival, and Destruction of Vortices in Accretion Disks”, *Astrophys. J.*, 693:85–96
- Lodders, K. (2003), “Solar System Abundances and Condensation Temperatures of the Elements”, *Astrophys. J.*, 591:1220–1247
- Löhne, T., Krivov, A. V., & Rodmann, J. (2008), “Long-Term Collisional Evolution of Debris Disks”, *Astrophys. J.*, 673:1123–1137
- Lorente, R., Onaka, T., Ita, Y., et al. (2007), *AKARI IRC Data User Manual Version 1.4*
- Lovis, C., Mayor, M., Pepe, F., et al. (2006), “An extrasolar planetary system with three Neptune-mass planets”, *Nature*, 441:305–309
- Maciejewski, G., Dimitrov, D., Neuhäuser, R., et al. (2011a), “Transit timing variation and activity in the WASP-10 planetary system”, *MNRAS*, 411:1204–1212
- Maciejewski, G., Seeliger, M., Adam, C., et al. (2011b), “Refining Parameters of the XO-5 Planetary System with High-Precision Transit Photometry”, *Acta Astronomica*, 61:25–35
- Madhusudhan, N., Burrows, A., & Currie, T. (2011), “Model Atmospheres for Massive Gas Giants with Thick Clouds: Application to the HR 8799 Planets and Predictions for Future Detections”, *Astrophys. J.*, 737:34
- Maldonado, J., Eiroa, C., Villaver, E., et al. (2012), “Metallicity of solar-type stars with debris discs and planets”, *Astron. Astrophys.*, 541:A40
- Mamajek, E. E., Meyer, M. R., Hinz, P. M., et al. (2004), “Constraining the Lifetime of Circumstellar Disks in the Terrestrial Planet Zone: A Mid-Infrared Survey of the 30 Myr old Tucana-Horologium Association”, *Astrophys. J.*, 612:496–510
- Marengo, M., Megeath, S. T., Fazio, G. G., et al. (2006), “A Spitzer IRAC Search for Substellar Companions of the Debris Disk Star  $\varepsilon$  Eridani”, *Astrophys. J.*, 647:1437–1451

- Marengo, M., Stapelfeldt, K., Werner, M. W., et al. (2009), “Spitzer/Infrared Array Camera Limits to Planetary Companions of Fomalhaut and epsilon Eridani”, *Astrophys. J.*, 700:1647–1657
- Marley, M. S., Fortney, J. J., Hubickyj, O., et al. (2007), “On the Luminosity of Young Jupiters”, *Astrophys. J.*, 655:541–549
- Marley, M. S., Saumon, D., & Goldblatt, C. (2010), “A Patchy Cloud Model for the L to T Dwarf Transition”, *Astrophys. J. Letters*, 723:L117–L121
- Marois, C., Macintosh, B., Barman, T., et al. (2008), “Direct Imaging of Multiple Planets Orbiting the Star HR 8799”, *Science*, 322:1348–
- Marois, C., Zuckerman, B., Konopacky, Q. M., et al. (2010), “Images of a fourth planet orbiting HR 8799”, *Nature*, 468:1080–1083
- Mayor, M., Marmier, M., Lovis, C., et al. (2011), “The HARPS search for southern extra-solar planets XXXIV. Occurrence, mass distribution and orbital properties of super-Earths and Neptune-mass planets”, *ArXiv e-prints*
- Mayor, M. & Queloz, D. (1995), “A Jupiter-mass companion to a solar-type star”, *Nature*, 378:355–359
- Metchev, S., Marois, C., & Zuckerman, B. (2009), “Pre-Discovery 2007 Image of the HR 8799 Planetary System”, *Astrophys. J. Letters*, 705:L204–L207
- Mizuno, H., Nakazawa, K., & Hayashi, C. (1980), “Dissolution of the primordial rare gases into the molten earth’s material”, *Earth and Planetary Science Letters*, 50:202–210
- Monet, D. G., Levine, S. E., Canzian, B., et al. (2003), “The USNO-B Catalog”, *Astron. J.*, 125:984–993
- Moór, A., Ábrahám, P., Derekas, A., et al. (2006), “Nearby Debris Disk Systems with High Fractional Luminosity Reconsidered”, *Astrophys. J.*, 644:525–542
- Morales, F. Y., Padgett, D. L., Bryden, G., et al. (2012), “WISE Detections of Dust in the Habitable Zones of Planet-bearing Stars”, *Astrophys. J.*, 757:7
- Morbidelli, A., Bottke, W. F., Nesvorný, D., et al. (2009), “Asteroids were born big”, *Icarus*, 204:558–573
- Moro-Martín, A., Carpenter, J. M., Meyer, M. R., et al. (2007), “Are Debris Disks and Massive Planets Correlated?”, *Astrophys. J.*, 658:1312–1321
- Moro-Martín, A. & Malhotra, R. (2002), “A Study of the Dynamics of Dust from the Kuiper Belt: Spatial Distribution and Spectral Energy Distribution”, *Astron. J.*, 124:2305–2321
- Moro-Martín, A. & Malhotra, R. (2003), “Dynamical Models of Kuiper Belt Dust in the Inner and Outer Solar System”, *Astron. J.*, 125:2255–2265
- Moro-Martín, A. & Malhotra, R. (2005), “Dust outflows and inner gaps generated by massive planets in debris disks”, *Astrophys. J.*, 633:1150–1167

- Moro-Martín, A., Rieke, G. H., & Su, K. Y. L. (2010), “Could the Planets Around HR 8799 be Brown Dwarfs?”, *Astrophys. J. Letters*, 721:L199–L202
- Moshir, M., Kopan, G., Conrow, T., et al. (1990), *IRAS Faint Source Catalogue, version 2.0*.
- Mouillet, D., Larwood, J. D., Papaloizou, J. C. B., et al. (1997), “A planet on an inclined orbit as an explanation of the warp in the Beta Pictoris disc”, *MNRAS*, 292:896
- Mukai, T. & Fechtig, H. (1983), “Packing effect of fluffy particles”, *Planet. Space Sci.*, 31:655–658
- Müller, S., Löhne, T., & Krivov, A. V. (2010), “The Debris Disk of Vega: A Steady-state Collisional Cascade, Naturally”, *Astrophys. J.*, 708:1728–1747
- Murakami, H., Baba, H., Barthel, P., et al. (2007), “The Infrared Astronomical Mission AKARI”, *PASJ*, 59:369
- Murray, C. D. & Dermott, S. F. (2000), *Solar System Dynamics*, Cambridge: University Press, 2000, ISBN 9780521575973
- Mustill, A. J. & Wyatt, M. C. (2009), “Debris disc stirring by secular perturbations from giant planets”, *MNRAS*, 399:1403–1414
- Nero, D. & Bjorkman, J. E. (2009), “Did Fomalhaut, HR 8799, and HL Tauri Form Planets Via the Gravitational Instability? Placing Limits on the Required Disk Masses”, *Astrophys. J. Letters*, 702:L163–L167
- Neugebauer, G., Habing, H. J., van Duinen, R., et al. (1984), “The Infrared Astronomical Satellite (IRAS) mission”, *Astrophys. J. Letters*, 278:L1–L6
- O’Brien, D. P. & Greenberg, R. (2003), “Steady-state size distributions for collisional populations: analytical solution with size-dependent strength”, *Icarus*, 164:334–345
- O’Brien, D. P., Morbidelli, A., & Levison, H. F. (2006), “Terrestrial planet formation with strong dynamical friction”, *Icarus*, 184:39–58
- O’Donovan, F. T., Charbonneau, D., Mandushev, G., et al. (2006), “TrES-2: The First Transiting Planet in the Kepler Field”, *Astrophys. J. Letters*, 651:L61–L64
- Okuzumi, S., Tanaka, H., Kobayashi, H., et al. (2012), “Rapid Coagulation of Porous Dust Aggregates outside the Snow Line: A Pathway to Successful Icy Planetesimal Formation”, *Astrophys. J.*, 752:106
- Ozernoy, L. M., Gorkavyi, N. N., Mather, J. C., et al. (2000), “Signatures of Exosolar Planets in Dust Debris Disks”, *Astrophys. J. Letters*, 537:L147–L151
- Pál, A., Bakos, G. Á., Fernandez, J., et al. (2009), “Independent Confirmation and Refined Parameters of the Hot Jupiter XO-5b”, *Astrophys. J.*, 700:783–790
- Paolicchi, P., Verlicchi, A., & Cellino, A. (1996), “An Improved Semi-Empirical Model of Catastrophic Impact Processes. I: Theory and Laboratory Experiments”, *Icarus*, 121:126–157

- Pasinetti Fracassini, L. E., Pastori, L., Covino, S., et al. (2001), “Catalogue of Apparent Diameters and Absolute Radii of Stars (CADARS) - Third edition - Comments and statistics”, *Astron. Astrophys.*, 367:521–524
- Patience, J., Bulger, J., King, R. R., et al. (2011), “Spatially resolved submillimeter imaging of the HR 8799 debris disk”, *Astron. Astrophys.*, 531:L17
- Paunzen, E., Duffee, B., Heiter, U., et al. (2001), “A spectroscopic survey for lambda Bootis stars. II. The observational data”, *Astron. Astrophys.*, 373:625–632
- Payne, M. J., Ford, E. B., Wyatt, M. C., et al. (2009), “Dynamical simulations of the planetary system HD69830”, *MNRAS*, 393:1219–1234
- Perryman, M. A. C. & ESA (Editors) (1997), *The HIPPARCOS and TYCHO catalogues. Astrometric and photometric star catalogues derived from the ESA HIPPARCOS Space Astrometry Mission*, vol. 1200 of *ESA Special Publication*
- Plavchan, P., Jura, M., & Lipsky, S. J. (2005), “Where Are the M Dwarf Disks Older Than 10 Million Years?”, *Astrophys. J.*, 631:1161–1169
- Pollack, J. B., Hubickyj, O., Bodenheimer, P., et al. (1996), “Formation of the Giant Planets by Concurrent Accretion of Solids and Gas”, *Icarus*, 124:62–85
- Poynting, J. H. (1903), “Radiation in the solar system : its effect on temperature and its pressure on small bodies”, *MNRAS*, 64:A1
- Press, W. H., Teukolsky, S. A., Vetterling, W. T., et al. (1992), *Numerical recipes in C. The art of scientific computing*, Cambridge: University Press, 1992, 2nd ed.
- Queck, M., Krivov, A. V., Sremčević, M., et al. (2007), “Collisional velocities and rates in resonant planetesimal belts”, *Celestial Mechanics and Dynamical Astronomy*, 99:169–196
- Quillen, A. C. (2006), “Predictions for a planet just inside Fomalhaut’s eccentric ring”, *MNRAS*, 372:L14–L18
- Quillen, A. C. & Thorndike, S. (2002), “Structure in the  $\epsilon$  Eridani Dusty Disk Caused by Mean Motion Resonances with a 0.3 Eccentricity Planet at Periastron”, *Astrophys. J. Letters*, 578:L149–L152
- Rafikov, R. R. (2005), “Can Giant Planets Form by Direct Gravitational Instability?”, *Astrophys. J. Letters*, 621:L69–L72
- Rafikov, R. R. (2007), “Convective Cooling and Fragmentation of Gravitationally Unstable Disks”, *Astrophys. J.*, 662:642–650
- Rätz, S., Mugrauer, M., Schmidt, T. O. B., et al. (2009), “Planetary transit observations at the University Observatory Jena: TrES-2”, *Astronomische Nachrichten*, 330:459
- Raymond, S. N., Armitage, P. J., Moro-Martín, A., et al. (2011), “Debris disks as signposts of terrestrial planet formation”, *Astron. Astrophys.*, 530:A62

- Raymond, S. N., Barnes, R., Armitage, P. J., et al. (2008), “Mean Motion Resonances from Planet-Planet Scattering”, *Astrophys. J. Letters*, 687:L107–L110
- Raymond, S. N., Barnes, R., & Kaib, N. A. (2006), “Predicting Planets in Known Extrasolar Planetary Systems. III. Forming Terrestrial Planets”, *Astrophys. J.*, 644:1223–1231
- Raymond, S. N., O’Brien, D. P., Morbidelli, A., et al. (2009), “Building the terrestrial planets: Constrained accretion in the inner Solar System”, *Icarus*, 203:644–662
- Reidemeister, M., Krivov, A. V., Schmidt, T. O. B., et al. (2009), “A possible architecture of the planetary system HR 8799”, *Astron. Astrophys.*, 503:247–258
- Reidemeister, M., Krivov, A. V., Stark, C. C., et al. (2011), “The cold origin of the warm dust around  $\varepsilon$  Eridani”, *Astron. Astrophys.*, 527:A57
- Rhee, J. H., Song, I., & Zuckerman, B. (2007), “EF Chamaeleontis: Warm Dust Orbiting a Nearby 10 Myr Old Star”, *Astrophys. J.*, 671:616–621
- Rhee, J. H., Song, I., & Zuckerman, B. (2008), “Warm Dust in the Terrestrial Planet Zone of a Sun-like Pleiades Star: Collisions between Planetary Embryos?”, *Astrophys. J.*, 675:777–783
- Ribas, Á., Merín, B., Ardila, D. R., et al. (2012), “Warm debris disks candidates in transiting planets systems”, *Astron. Astrophys.*, 541:A38
- Rieke, G. H. & Lebofsky, M. J. (1985), “The interstellar extinction law from 1 to 13 microns”, *Astrophys. J.*, 288:618–621
- Robertson, H. P. (1937), “Dynamical effects of radiation in the solar system”, *MNRAS*, 97:423
- Rodriguez, E. & Zerbi, F. M. (1995), “A long period early F-type variable: HR8799”, *Information Bulletin on Variable Stars*, 4170:1–+
- Royer, F., Zorec, J., & Gómez, A. E. (2007), “Rotational velocities of A-type stars. III. Velocity distributions”, *Astron. Astrophys.*, 463:671–682
- Sadakane, K. (2006), “ $\lambda$  Bootis-Like Abundances in the Vega-Like,  $\gamma$  Doradus Type-Pulsator HD 218396”, *PASJ*, 58:1023–1032
- Sadakane, K. & Nishida, M. (1986), “Twelve additional ‘Vega-like’ stars”, *PASP*, 98:685–689
- Saffe, C., Gómez, M., & Chavero, C. (2005), “On the ages of exoplanet host stars”, *Astron. Astrophys.*, 443:609–626
- Safronov, V. S. (1969), *Evolution of the protoplanetary cloud and formation of the earth and the planets*, Nauka, Moscow (in Russian). [English translation: NASA TTF-677, 1972.]
- Saumon, D., Chabrier, G., & van Horn, H. M. (1995), “An Equation of State for Low-Mass Stars and Giant Planets”, *Astrophys. J. Suppl.*, 99:713

- Schmidt, T. O. B., Neuhäuser, R., & Seifahrt, A. (2009), “Homogeneous Comparison of Planet Candidates Imaged Directly Until 2008”, in T. Usuda, M. Tamura, & M. Ishii (Editor), “American Institute of Physics Conference Series”, vol. 1158 of *American Institute of Physics Conference Series*, pp. 231–234
- Schneider, J., Dedieu, C., Le Sidaner, P., et al. (2011), “Defining and cataloging exoplanets: the exoplanet.eu database”, *Astron. Astrophys.*, 532:A79
- Skemer, A. J., Hinz, P. M., Esposito, S., et al. (2012), “First Light LBT AO Images of HR 8799 bcde at 1.6 and 3.3  $\mu\text{m}$ : New Discrepancies between Young Planets and Old Brown Dwarfs”, *Astrophys. J.*, 753:14
- Skrutskie, M. F., Cutri, R. M., Stiening, R., et al. (2006), “The Two Micron All Sky Survey (2MASS)”, *Astron. J.*, 131:1163–1183
- Skrutskie, M. F., Dutkevitch, D., Strom, S. E., et al. (1990), “A sensitive 10-micron search for emission arising from circumstellar dust associated with solar-type pre-main-sequence stars”, *Astron. J.*, 99:1187–1195
- Soderblom, D. R. & Dappen, W. (1989), “Modeling Epsilon Eridani and its oscillations”, *Astrophys. J.*, 342:945–950
- Song, I., Caillault, J.-P., Barrado y Navascués, D., et al. (2000), “Ages of Late Spectral Type Vega-like Stars”, *Astrophys. J. Letters*, 533:L41–L44
- Song, I., Caillault, J.-P., Barrado y Navascués, D., et al. (2001), “Ages of A-Type Vega-like Stars from uvby $\beta$  Photometry”, *Astrophys. J.*, 546:352–357
- Song, I., Zuckerman, B., Weinberger, A. J., et al. (2005), “Extreme collisions between planetesimals as the origin of warm dust around a Sun-like star”, *Nature*, 436:363–365
- Soummer, R., Brendan Hagan, J., Pueyo, L., et al. (2011), “Orbital Motion of HR 8799 b, c, d Using Hubble Space Telescope Data from 1998: Constraints on Inclination, Eccentricity, and Stability”, *Astrophys. J.*, 741:55
- Spiegel, D. S. & Burrows, A. (2012), “Spectral and Photometric Diagnostics of Giant Planet Formation Scenarios”, *Astrophys. J.*, 745:174
- Stevenson, D. J. (1982), “Formation of the giant planets”, *Planet. Space Sci.*, 30:755–764
- Stewart, G. R. & Wetherill, G. W. (1988), “Evolution of planetesimal velocities”, *Icarus*, 74:542–553
- Stewart, S. T. & Leinhardt, Z. M. (2009), “Velocity-Dependent Catastrophic Disruption Criteria for Planetesimals”, *Astrophys. J. Letters*, 691:L133–L137
- Strubbe, L. E. & Chiang, E. I. (2006), “Dust dynamics, surface brightness profiles, and thermal spectra of debris disks: The case of AU Mic”, *Astrophys. J.*, 648:652–665
- Su, K. Y. L., Rieke, G. H., Stansberry, J. A., et al. (2006), “Debris disk evolution around A stars”, *Astrophys. J.*, 653:675–689



- Su, K. Y. L., Rieke, G. H., Stapelfeldt, K. R., et al. (2009), “The Debris Disk Around HR 8799”, *Astrophys. J.*, 705:314–327
- Sudol, J. J. & Haghhighipour, N. (2012), “High-mass, Four-planet Configurations for HR 8799: Constraining the Orbital Inclination and Age of the System”, *Astrophys. J.*, 755:38
- Sylvester, R. J., Skinner, C. J., Barlow, M. J., et al. (1996), “Optical, infrared and millimetre-wave properties of Vega-like systems.”, *MNRAS*, 279:915–939
- Tanner, A., Beichman, C., Bryden, G., et al. (2009), “Survey of Nearby FGK Stars at 160  $\mu\text{m}$  with Spitzer”, *Astrophys. J.*, 704:109–116
- Th ebault, P. & Augereau, J.-C. (2007), “Collisional processes and size distribution in spatially extended debris discs”, *Astron. Astrophys.*, 472:169–185
- Thommes, E. W. (2005), “A Safety Net for Fast Migrators: Interactions between Gap-opening and Sub-Gap-opening Bodies in a Protoplanetary Disk”, *Astrophys. J.*, 626:1033–1044
- Toomre, A. (1964), “On the gravitational stability of a disk of stars”, *Astrophys. J.*, 139:1217–1238
- Trilling, D. E., Bryden, G., Beichman, C. A., et al. (2008), “Debris Disks around Sun-like Stars”, *Astrophys. J.*, 674:1086–1105
- Turcotte, S. (2002), “Mixing and Accretion in  $\lambda$  Bootis Stars”, *Astrophys. J. Letters*, 573:L129–L132
- Uesugi, A. & Fukuda, I. (1982), *Catalogue of stellar rotational velocities (revised)*, Kyoto: University of Kyoto, Departement of Astronomy, 1982, Rev.ed.
- van Belle, G. T. & von Braun, K. (2009), “Directly Determined Linear Radii and Effective Temperatures of Exoplanet Host Stars”, *Astrophys. J.*, 694:1085–1098
- van Boekel, R., Waters, L. B. F. M., Dominik, C., et al. (2004), “Spatially and spectrally resolved 10  $\mu\text{m}$  emission in Herbig Ae/Be stars”, *Astron. Astrophys.*, 418:177–184
- Veras, D. & Armitage, P. J. (2004), “Outward migration of extrasolar planets to large orbital radii”, *MNRAS*, 347:613–624
- Verdugo, E., Yamamura, I., & Pearson, C. P. (2007), *AKARI FIS Data User Manual Version 1.3*, URL <http://www.ir.isas.jaxa.jp/AKARI/Publications/guideline.html>
- Vitense, C., Krivov, A. V., Kobayashi, H., et al. (2012), “An improved model of the Edgeworth-Kuiper debris disk”, *Astron. Astrophys.*, 540:A30
- Vitense, C., Krivov, A. V., & L ohne, T. (2010), “The Edgeworth-Kuiper debris disk”, *Astron. Astrophys.*, 520:A32
- Vorobyov, E. I. & Basu, S. (2008), “Mass Accretion Rates in Self-Regulated Disks of T Tauri Stars”, *Astrophys. J. Letters*, 676:L139–L142

- Wada, K., Tanaka, H., Suyama, T., et al. (2011), “The Rebound Condition of Dust Aggregates Revealed by Numerical Simulation of Their Collisions”, *Astrophys. J.*, 737:36
- Wang, Q.-D. (1991), “The global solution of the n-body problem”, *Celestial Mechanics and Dynamical Astronomy*, 50:73–88
- Weidenschilling, S. J. (1977), “Aerodynamics of solid bodies in the solar nebula”, *MNRAS*, 180:57–70
- Weidenschilling, S. J. (2011), “Initial sizes of planetesimals and accretion of the asteroids”, *Icarus*, 214:671–684
- Werner, M. W., Roellig, T. L., Low, F. J., et al. (2004), “The Spitzer Space Telescope Mission”, *Astrophys. J. Suppl.*, 154:1–9
- Wetherill, G. W. (1980), “Formation of the terrestrial planets”, *Ann. Rev. Astron. Astrophys.*, 18:77–113
- Wetherill, G. W. & Stewart, G. R. (1989), “Accumulation of a swarm of small planetesimals”, *Icarus*, 77:330–357
- Williams, J. P. & Andrews, S. M. (2006), “The Dust Properties of Eight Debris Disk Candidates as Determined by Submillimeter Photometry”, *Astrophys. J.*, 653:1480–1485
- Williams, J. P. & Cieza, L. A. (2011), “Protoplanetary Disks and Their Evolution”, *Ann. Rev. Astron. Astrophys.*, 49:67–117
- Wisdom, J. & Holman, M. (1991), “Symplectic maps for the n-body problem”, *Astron. J.*, 102:1528–1538
- Wolk, S. J. & Walter, F. M. (1996), “A Search for Protoplanetary Disks Around Naked T Tauri Stars”, *Astron. J.*, 111:2066
- Wood, B. E., Müller, H.-R., Zank, G. P., et al. (2002), “Measured Mass-Loss Rates of Solar-like Stars as a Function of Age and Activity”, *Astrophys. J.*, 574:412–425
- Wright, D. J., Chené, A.-N., De Cat, P., et al. (2011a), “Determination of the Inclination of the Multi-planet Hosting Star HR 8799 Using Asteroseismology”, *Astrophys. J. Letters*, 728:L20
- Wright, E. L., Eisenhardt, P. R. M., Mainzer, A. K., et al. (2010), “The Wide-field Infrared Survey Explorer (WISE): Mission Description and Initial On-orbit Performance”, *Astron. J.*, 140:1868
- Wright, J. T., Fakhouri, O., Marcy, G. W., et al. (2011b), “The Exoplanet Orbit Database”, *PASP*, 123:412–422
- Wuchterl, G. (2001), “A Dialogue on Dynamical Pre-Main Sequence Tracks”, in H. Zinnecker & R. Mathieu (Editors), “The Formation of Binary Stars”, vol. 200 of *IAU Symposium*, pp. 492–+

- Wyatt, M. C. (2005), “The insignificance of P-R drag in detectable extrasolar planetesimal belts”, *Astron. Astrophys.*, 433:1007–1012
- Wyatt, M. C., Booth, M., Payne, M. J., et al. (2010), “Collisional evolution of eccentric planetesimal swarms”, *MNRAS*, 402:657–672
- Wyatt, M. C., Clarke, C. J., & Booth, M. (2011), “Debris disk size distributions: steady state collisional evolution with Poynting-Robertson drag and other loss processes”, *Celestial Mechanics and Dynamical Astronomy*, 111:1–28
- Wyatt, M. C., Greaves, J. S., Dent, W. R. F., et al. (2005), “Submillimeter Images of a Dusty Kuiper Belt around  $\eta$  Corvi”, *Astrophys. J.*, 620:492–500
- Wyatt, M. C., Kennedy, G., Sibthorpe, B., et al. (2012), “Herschel imaging of 61 Vir: implications for the prevalence of debris in low-mass planetary systems”, *MNRAS*, 424:1206–1223
- Wyatt, S. P. & Whipple, F. L. (1950), “The Poynting-Robertson effect on meteor orbits”, *Astrophys. J.*, 111:134–141
- Yamamura, I., Makiuti, S., Ikeda, N., et al. (2010), “AKARI/FIS All-Sky Survey Point Source Catalogues (ISAS/JAXA, 2010)”, *VizieR Online Data Catalog*, 2298:0
- Yi, S., Demarque, P., Kim, Y.-C., et al. (2001), “Toward Better Age Estimates for Stellar Populations: The  $Y^2$  Isochrones for Solar Mixture”, *Astrophys. J. Suppl.*, 136:417–437
- Yoshida, H. (1993), “Recent Progress in the Theory and Application of Symplectic Integrators”, *Celestial Mechanics and Dynamical Astronomy*, 56:27–43
- Zacharias, N., Monet, D. G., Levine, S. E., et al. (2004), “The Naval Observatory Merged Astrometric Dataset (NOMAD)”, *BAAS*, 36:1418–+
- Zerbi, F. M., Rodríguez, E., Garrido, R., et al. (1999), “The gamma DOR variable HR 8799: results from a multisite campaign”, *MNRAS*, 303:275–283
- Zhou, J.-L., Xie, J.-W., Liu, H.-G., et al. (2012), “Forming different planetary systems”, *Research in Astronomy and Astrophysics*, 12:1081–1106
- Zsom, A., Ormel, C. W., Güttler, C., et al. (2010), “The outcome of protoplanetary dust growth: pebbles, boulders, or planetesimals? II. Introducing the bouncing barrier”, *Astron. Astrophys.*, 513:A57+
- Zuckerman, B. & Song, I. (2004), “Dusty Debris Disks as Signposts of Planets: Implications for Spitzer Space Telescope”, *Astrophys. J.*, 603:738–743



# Ehrenwörtliche Erklärung

Ich erkläre hiermit ehrenwörtlich, dass ich die vorliegende Arbeit selbstständig, ohne unzulässige Hilfe Dritter und ohne Benutzung anderer als der angegebenen Hilfsmittel und Literatur angefertigt habe. Die aus anderen Quellen direkt oder indirekt übernommenen Daten und Konzepte sind unter Angabe der Quelle gekennzeichnet.

Weitere Personen waren an der inhaltlich-materiellen Erstellung der vorliegenden Arbeit nicht beteiligt. Insbesondere habe ich hierfür nicht die entgeltliche Hilfe von Vermittlungs- bzw. Beratungsdiensten (Promotionsberater oder andere Personen) in Anspruch genommen. Niemand hat von mir unmittelbar oder mittelbar geldwertige Leistungen für Arbeiten erhalten, die im Zusammenhang mit dem Inhalt der vorgelegten Dissertation stehen.

Die Arbeit wurde bisher weder im In- noch Ausland in gleicher oder ähnlicher Form einer anderen Prüfungsbehörde vorgelegt.

Die geltende Promotionsordnung der Physikalisch-Astronomischen Fakultät ist mir bekannt.

Ich versichere ehrenwörtlich, dass ich nach bestem Wissen die reine Wahrheit gesagt und nichts verschwiegen habe.

Jena, 23. Mai 2013

Martin Reidemeister



# Lebenslauf

## Persönliche Daten

Name Martin Reidemeister  
Geburtsdatum 25.03.1982  
Geburtsort Magdeburg  
Wohnort Karl-Liebknecht-Straße 4  
07749 Jena  
Dienstanschrift Astrophysikalisches Institut und Universitäts-Sternwarte  
Friedrich-Schiller-Universität  
Schillergäßchen 2-3  
07745 Jena  
eMail martin.reidemeister@astro.uni-jena.de  
Telefon +49-3641-947-548

## Werdegang

Schulbildung 1988 – 1992  
Lessing Grundschule, Magdeburg  
1992 – 2000  
Wilhelm-Raabe-Gymnasium, Magdeburg  
04.07.2000 Abschluss: Abitur  
Gesamtnote „Gut (2,2)“  
(Leistungskurse: Mathematik, Physik)  
Zivildienst 09/2000 – 07/2001  
Kreiskrankenhaus Burg  
Pflegehelfer auf einer chirurgischen Station  
Studium 10/2001 – 09/2004  
Otto-von-Guericke-Universität, Magdeburg  
Studiengang Physik (Diplom)  
10/2004 – 12/2007  
Friedrich-Schiller-Universität, Jena  
Studiengang Physik (Diplom)  
10/2006 – 11/2007  
Diplomarbeit zum Thema „Resonante Dynamik von Staubteilchen in Trümmerscheiben mit Planeten“ bei Prof. Dr. Alexander Krivov  
20.12.2007 Abschluss: Diplom  
Gesamtnote „Sehr gut (1,5)“

Promotion	05/2008 – 12/2012 Dissertation zum Thema „Architecture of selected full planetary systems“ bei Prof. Dr. Alexander Krivov am AIU Jena
Verteidigung	16. 04. 2013 Abschluss: Dr. rer. nat. Gesamturteil: „magna cum laude“
Lehre	10/2008 – 07/2012 Betreuung physikalisches Grundpraktikum (Physiker und Nebenfächler)  10/2011 – 03/2012 Seminarleiter „Celestial Mechanics“
Vorträge	07. 04. 2009 <i>ISSI: Exozodiacal Dust Disks and Darwin</i> in Bern – „HR8799: A planetary system with cold and warm dust“ und „ $\epsilon$ Eri (lack of) exozodi: review of recent observations and modeling“  15. 11. 2010 <i>YETI Collaboration Meeting</i> in Jena – „Architectures of planetary systems: HR 8799 and $\epsilon$ Eridani“  15. 02. 2011 <i>Planet Formation Workshop</i> in Göttingen – „The cold origin of warm dust around $\epsilon$ Eridani“
Publikationen	<u>Reidemeister, M.</u> , Krivov, A. V., Schmidt, T. O. B., et al. (2009), „A possible architecture of the planetary system HR 8799“, <i>Astronomy &amp; Astrophysics</i> , 503:247-258  <u>Reidemeister, M.</u> , Krivov, A. V., Stark, C. C., et al. (2011), „The cold origin of the warm dust around $\epsilon$ Eridani“, <i>Astronomy &amp; Astrophysics</i> , 527:A57  <u>Reidemeister, M.</u> , Krivov, A. V., Stark, C. C., et al. (2011), „Warm dust around $\epsilon$ Eridani“, in A. Sozzetti, M. G. Lattanzi, & A. P. Boss (Editors), <i>IAU Symposium</i> , vol. 276, pp. 455–456  Krivov, A. V., <u>Reidemeister, M.</u> , Fiedler, S., et al. (2011), „Warm dust in systems with transiting planets“, in „EPSC-DPS Joint Meeting 2011“, p. 475  Krivov, A. V., <u>Reidemeister, M.</u> , Fiedler, S., et al. (2011), „Debris disc candidates in systems with transiting planets“, <i>MNRAS</i> , 418:L15-L19

Jena, den 23. Mai 2013

Martin Reidemeister